FACULTY
OF MATHEMATICS
AND PHYSICS
Charles University

# DOCTORAL THESIS

Oleksandra Koloskova

## U-based thin films: electronic structure and physical properties

Department of Condensed Matter Physics

Supervisor of the doctoral thesis: Doc. RNDr. Ladislav Havela, CSc.

Study programme: Physics

Specialization: Physics of Condensed Matter and Materials

Prague 2024

I declare that I carried out this doctoral thesis independently, and only with the cited sources, literature and other professional sources.

I understand that my work relates to the rights and obligations under the Act No. 121/2000 Coll., the Copyright Act, as amended, in particular the fact that the Charles University has the right to conclude a license agreement on the use of this work as a school work pursuant to Section 60 paragraph 1 of the Copyright Act.

In…..... date..... signature

**Acknowledgments**

I would like to take this opportunity to express my gratitude to all the people who influenced the beginning of my scientific journey and helped me make what I hope is the right choice of a life path.

First and foremost, I would like to thank to my supervisor, Ladislav Havela, whose advice and scientific knowledge have driven this work to completion. Through gentle guidance, long scientific discussions, and an endless positive attitude, he walked me through the long and rough path of a PhD student.

I am grateful to Volodymyr Buturlim and Mykhaylo Paukov for "the course of a young researcher." Their instructions helped instill necessary habits for efficient work in the lab. I also wish to express my deepest appreciation to Thomas Gouder and Frank Huber from EC JRC Karlsruhe for their unwavering support of any "crazy" experimental idea and their technical assistance in sample preparation.

My thanks go to Peter Minárik and Mayerling Martinez Celis for their beautiful images of the "inner micro-world" of uranium hydrides. Special gratitude goes to Evgenia Tereshina-Chitrova and Lukáš Horák for their efforts in detangling the crystal structures of thin film samples. I also wish to acknowledge Martin Diviš, Jindřich Kolorenč and Dominik Legut for their readiness to support our experimental results with theoretical calculations.

I am also grateful to the staff of the Materials Growth & Measurement Laboratory, particularly Martin Žáček, Jan Prokleška, and Petr Proschek, for their invaluable help with resistivity and magnetization measurements.

A special mention goes to my friend, Daria Drozdenko, for sharing my passion for science and for motivating and supporting me on every occasion.

None of this would have been possible without my family. I am deeply thankful to my parents for the initial impulse that pushed me to move to Prague. Finally, I thank to Dan, for being there for me through my state exam, a pandemic, long experiments, work trips, and late-night thesis writing.

Název práce: Tenké vrstvy na bázi uranu: elektronová struktura a fyzikální vlastnosti

Autor: Oleksandra Koloskova

Katedra / Ústav: Katedra fyziky kondenzovaných látek

Vedoucí doktorské práce: Doc. RNDr. Ladislav Havela, CSc.

Abstrakt: Tato práce se zabývá studiem tenkých vrstev na bázi uranu deponovaných pomocí DC naprašování, které umožňuje změny v kompozici a mikrostruktuře a zkoumání pomocí fotoelektronové spektroskopie. Předmětem studia jsou slitiny U-Mo a U-Zr, uranové hydridy ($UH_3$ and $UH_2$) a uranové hydridy se substitucí Zr/Mo.

Nejprve byla provedena *in-situ* analýza a poté *ex-situ* analýzy struktury a magnetických a transportních vlastností. Navzdory supravodivému stavu U-T slitin, pouze jeden film ($U_{0.92}Mo_{0.08}$) supravodivost vykazuje, a to s přechodem při teplotě 0,55 K.

Všechny hydridy jsou ferromagnetické, přičemž jejich Curieovy teploty se pohybují kolem 120 K pro $UH_2$ a 170 K pro α- a β-$UH_3$. Tento ferromagnetismus je robustní a nezávislý na strukturních detailech. Variací parametrů naprašování můžeme získat $UH_2$ (který se v bulku nevyskytuje), β-$UH_3$, nebo koexistenci $UH_2$ and α-$UH_3$. Inkluze atomů vodíku drasticky ovlivňuje vlastnosti. Konkrétně mění paramagnetické slitiny na ferromagnetické hydridy, a pro feromagnetismus je zde velmi důležitá U-H polární vazba. Pásově ferromagnetická povaha $UH_3$ byla objasněna porovnáním DMFT výpočtů se spektry XPS a UPS. Tato spektra vykazují finální stav s rysy $5f^2$ multipletu a výrazné electron-elektronové korelace.

Substituce Zr v hydridových filmech stabilizovala $UH_2$ místo očekávané fáze α-$UH_3$. Série $(UH_3)_{1-x}Mo_x$, $(UH_3)_{1-x}Zr_x$ a $(UH_2)_{1-x}Zr_x$ mají nižší Curievy teploty než jejich bulkové verze a čisté $UH_2$ či $UH_3$ filmy. Tento pokles je připsán destabilizaci atomů vodíku v krystalové struktuře, která je způsobena zahrnutím přechodových kovů a kinetickou energií z depozičního procesu.

Klíčová slova: Tenké vrstvy, Uran, Supravodivost, Hydrid, Elektronická Struktura, Magnetismus

Title: U-based thin films: electronic structure and physical properties

Author: Oleksandra Koloskova

Department / Institute: Department of Condensed Matter Physics, Faculty of Mathematics and Physics, Charles University

Supervisor of the doctoral thesis: Doc. RNDr. Ladislav Havela, CSc., Department of Condensed Matter Physics, Faculty of Mathematics and Physics, Charles University, Prague, The Czech Republic

Abstract: This thesis presents studies of U-based thin films synthesized by means of the DC sputter deposition, which allows to vary the composition and microstructure and perform in photoelectron spectroscopy studies. The subjects are U-Mo and U-Zr alloys, Uranium hydrides ($UH_3$ and $UH_2$), and U hydrides with Zr/Mo substitution.

*In-situ* analysis was followed by *ex-situ* studies of structure, magnetic and transport properties. Despite the superconducting ground state of the U-T alloys, only one film ($U_{0.92}Mo_{0.08}$) exhibited superconductivity, with the transition at 0.55 K.

All hydrides are ferromagnetic, with Curie temperatures around 120 K for $UH_2$ and 170 K for both α- and β-$UH_3$. This ferromagnetism is robust and independent of structural details. By varying sputtering parameters, one can obtain $UH_2$ (nonexistent in bulk form), β-$UH_3$, or a mix of $UH_2$ and α-$UH_3$ (first observed in film form). Inclusion of hydrogen atoms drastically changes properties, shifting from paramagnetic alloys to ferromagnetic hydrides, with the U-H polar bond being crucial for magnetism. The nature of $UH_3$ as a band ferromagnet was clarified by comparing DMFT calculations with XPS and UPS spectra, revealing final-state $5f^2$ multiplet and emphasizing electron-electron correlations in $UH_3$.

Zr substitution in hydride films stabilized $UH_2$ instead of the expected α-$UH_3$ phase. Series $(UH_3)_{1-x}Mo_x$, $(UH_3)_{1-x}Zr_x$, and $(UH_2)_{1-x}Zr_x$ have lower Curie temperatures than their bulk counterparts and pure $UH_2$ or $UH_3$ films. This decrease is attributed to a destabilization of hydrogen caused by the incorporation of transition metals and the excessive energy from the deposition process.

Keywords: Thin Films, Uranium, Superconductivity, Hydride, Electronic Structure, Magnetism

**Contents**

## Introduction

Actinide elements represent an enigmatic segment of the periodic table, exhibiting diverse exotic properties. Despite their remarkable physical properties, actinide materials remain among the least understood elements due to their rarity, radioactivity, and synthesis difficulties. Their unusual behavior is related to the presence of 5*f* electrons, poised between localization and itinerancy. The *f*-electron orbitals, known for their high directionality (in case of involvement in bonds) and limited spatial extent, determine various bonding situations observed in actinide compounds. The localization tendency increases with the 5*f* occupancy and the threshold of full localization, occurring between Pu and Am in pure elements, can be shifted to U in compounds. This displacement presents numerous exciting opportunities for investigating phenomena associated with this threshold, including emergent phenomena, such as anomalous superconductivity, exotic types of magnetism, valence fluctuations, and charge ordering [1–4].

Electronic structure is a common denominator of basic properties of actinide systems. However, the complexity of the electronic structure brings uncertainty into a determination of the situation of 5*f* electrons, as it cannot be assessed from first principles calculations. Experimental studies targeting magnetic and other electronic properties are in such cases indispensable. Electron spectroscopies (XPS, UPS, BIS) bring more direct information (taken with precaution though) on electronic states than bulk properties and in the past they were successfully used to specify the localization, e-e interactions, as well as bonding characteristics. High-quality spectroscopic data demand high surface purity, which can be provided by thin film specimens prepared under ultra-high vacuum (UHV) conditions.

Thin films offer numerous advantages beyond the specimen purity. Sample synthesis is notably rapid compared to conventional bulk methods, facilitating the study of various compositions. The growth techniques allow precise control over deposition parameters, enabling structure, composition, phase, and stoichiometry engineering, resulting in the stabilization of thermodynamically unstable phases in some cases [5,6]. Thin film synthesis allows the production of amorphous, polycrystalline, or single-crystalline materials, with control over grain size and crystal quality, as well as the manipulation of strain fields. Additionally, thin film samples have tiny masses of radioactive material, making them accessible to a broader range

of facilities and institutions. Transport, handling, and storage of these samples are significantly simplified compared to their bulk counterparts.

Research of different forms of 5*f* magnetism and its relation to underlying electronic structure has been ongoing for several decades. The ability to manipulate properties of metallic systems through polar bonds (reduction of the 5*f*-6*d* hybridization in U by involving the 6*d* states in bonding with ligands) represents a novel aspect. This gives an additional avenue for modifying electronic structure and bringing 5*f* magnetism, accompanied by significant benefits from the strong spin-orbit interaction, such as giant anisotropy and magnetoresistance, to ambient temperatures.

Uranium hydride with a relatively high Curie temperature was chosen as a subject for the studies presented in this work to prove the importance of polar bonds. This thesis summarizes the results of my research activities on U hydrides thin films, conducted in the years 2019 - 2024 at the Charles University, Department of Condensed Matter Physics and EC JRC Karlsruhe, where the synthesis of samples and spectroscopic studies were carried out. My work under supervision of Dr. L. Havela was inspired by earlier PhD. theses of I. Tkach and V. Buturlim, who studied pure and alloyed U hydrides in a bulk form, and by research of M. Paukov, who was involved at first attempts to grow films of U hydrides. The success in preparing clean U hydride films was a key element that enabled thorough spectroscopic studies, serving as a cornerstone of the current understanding of actinide hydrides. This was developed by studies of electronic and lattice properties, which could be confronted with features known already from bulk studies, yielding a consistent framework, providing a general understanding of observed trends (some obvious, some surprising) related to variations of structure and composition.

The thesis starts with a brief introduction to the theory of solid state physics with an emphasis made on different types of magnetism (based on the localization of electronic states) and superconductivity (Sub-chapter 1.1). It is followed by the basic information on uranium metal and hydrides (Sub-chapter 1.2). Sub-chapter 1.3 describes the basic processes of experimental methods used in these studies (reactive DC sputtering, photoelectron spectroscopy and X-ray diffraction methods). Chapter 2 is fully dedicated to the experimental setup which was employed in these studies. Chapter 3 contains discussion of the electronic structure variations, structural, magnetic, and transport properties of the studied U-T (T – Mo, Zr), U-H and U-T-H thin films. The last part is dedicated to brief conclusions and future outlook.

# 1. Theory

In this study, our focus was on the fabrication and analysis of thin films of U hydrides and alloys. These films serve as valuable experimental proxies for bulk counterparts, offering a means to mitigate experimental risks and constraints associated with handling bulk radioactive materials. Adopting a thin film approach to the study of actinide compounds holds the promise of enhancing our understanding of 5*f* electron systems at a fundamental level.

Uranium compounds (pure and alloyed hydrides, in particular) are the main subject of the current studies. As will be shown later, U systems are on the verge between localization and itineracy. The primary criterion for distinguishing between localized and itinerant states lies in the dynamical properties of *f*-electrons. In localized states, *f*-electrons do not significantly contribute to the states at the Fermi energy ($E_F$), and the local *f*-electron configuration remains stable. Conversely, in itinerant states, *f*-electrons make finite contributions to the states at $E_F$, leading to dynamically fluctuating local *f*-electron configurations upon thermal excitation. These states significantly influence various transport properties, including electrical resistivity, magnetic susceptibility, and electronic specific heat. Therefore, the fundamental distinction between itinerant and localized *f*-electron states is evident in their dynamic rather than static properties. The electronic structure can be elucidated through optical measurements such as ultraviolet photoelectron spectroscopy (UPS), X-ray Photoelectron Spectroscopy (XPS), and Bremsstrahlung Isochromat Spectroscopy (BIS).

The chapter is divided into two sections. The first one describes the basic physics, which lies behind itinerant and localized systems and their properties. The second part includes principles of experimental methods used in these studies.

## *1.1. Selected topics of solid state physics*

### *1.1.1. Itinerant and localized electronic systems*

The difference between itinerant and localized electronic systems is a fundamental question in condensed matter physics, based on the diverse behaviors of electrons in different materials. Itinerant electron systems have delocalized electrons that are free to move throughout the crystal lattice, playing a crucial role in electrical

or thermal conductivity and phenomena such as band magnetism. On the other hand, localized electronic systems have electrons confined to specific atomic or molecular sites, leading to insulating behavior and distinct magnetic properties, as seen in Mott insulators and localized magnetic moments in rare-earth elements. The interplay between itinerant and localized electrons leads to complex phenomena like heavy fermion behavior, mixed valence systems, and the Kondo effect. These systems are often studied using advanced spectroscopic techniques and theoretical models, giving a comprehensive understanding of their electronic structure and magnetic interactions.

The thesis makes an emphasis on different types of magnetism coming from these two types of electronic systems. Itinerant electrons, often found in the conduction band, contribute to the magnetic properties by aligning their spins collectively. In such cases magnetism is often described by band theory, where the exchange interaction between conduction electrons causes a spontaneous alignment of spins. This kind of magnetism is strongly sensitive to temperature, pressure and chemical composition of the material.

Localized magnetism is based on the magnetic moments of individual atoms. Magnetic moments can be described by the Heisenberg model for instance, where the interaction between spins on different sites leads to magnetic ordering. Systems with localized magnetism often exhibit complex magnetic behaviors, including spin glass, ferrimagnetism, and more complex magnetic structures, influenced by factors like crystal field effects and spin-orbit coupling.

#### 1.1.1.1. Localized systems

In this section, the properties of metallic (lanthanides, in particular) systems with localized moments are discussed. In these elements, the unfilled 4*f* shell lies deep within the core of the atom and occupies a small spatial extent. It is shielded by the outer 6*s* and 5*d* shells. As a result, the 4*f* shell can be approximated as the atomic shell of a free ion, and calculations of atomic magnetic moment can be applied.

The Hamiltonian of 4*f* localized electrons can be written (considering negligible spin-orbit interaction):

$$H_{4f} = \sum_{i=1}^{N} -\frac{\hbar}{2m_e}\nabla_i^2 + \sum_{i=1}^{N} -\frac{\tilde{Z}e^2}{r_i} + \sum \frac{e^2}{r_{ij}} \tag{1.1}$$

This Hamiltonian includes the kinetic energy, interaction of 4*f* electrons with other filled shells, and interactions of electrons within the 4*f* shell. For the simplification of the calculations, the Hartree-Fock approximation (one-electron approximation) is often used. The Hamiltonian is rewritten then:

$$H_{4f} = \sum_{i=1}^{N} -\frac{\hbar}{2m_e}\nabla_i^2 + \sum_{i=1}^{N} -\frac{\tilde{Z}e^2}{r_i} + \sum_{i\neq j} V_i(r) \qquad (1.2)$$

Where the last term is substituted by self-consistent Hartree-Fock potential of 4*f* shell $V_i(r)$.

Such quantum numbers as total angular momentum *J*, total spin angular momentum *S*, and total orbital angular momentum *L* are used to characterize the ground state of a multi-electron atom. Hund's rules provide guidelines for determining how electrons occupy the electron shells in the ground state. Each electron possesses its own orbital angular momentum (*l*) and spin angular momentum (*s*). The total spin (*S*) and orbital (*L*) momenta are obtained by summing the momenta of individual electrons in the shell. To minimize the total energy, electrons fill the shell according to the following order of Hund's rules:

1. The total spin angular momentum (*S*) should be maximized.

2. For a given *S*, the total orbital angular momentum (*L*) is also maximized.

3. If the shell is half-filled or less, then the total angular momentum (*J*) is calculated as $J = L - S$. If the shell is more than half-filled, then $J = L + S$ (describes spin-orbit interaction of the same electron).

Atomic magnetic moments can be then calculated by: $\mu = g\mu_B J$, where $\mu_B$ is Bohr magneton and *g* stands for Landé factor, which is calculated as:

$$g = 1 + \frac{J(J+1)+S(S+1)-L(L+1)}{2J(J+1)} \qquad (1.3)$$

The negligible overlap of 4*f* orbitals limits direct exchange interactions in localized electron systems, making them weak. In these systems, magnetic moments of ions with electrons in localized states can become magnetically ordered via an indirect interaction mediated by conduction electrons. These conduction electrons, polarized by exchange interaction near an ion, facilitate the creation of a polarized cloud shared by two neighboring 4*f* ions (Fig. 1.1). This cloud fosters a long-range correlation between the orientations of magnetic moments of ions, leading to magnetic

ordering in localized electron systems. This form of indirect interaction is known as the RKKY interaction, named after the scientists Ruderman, Kittel, Kasuya, and Yoshida.

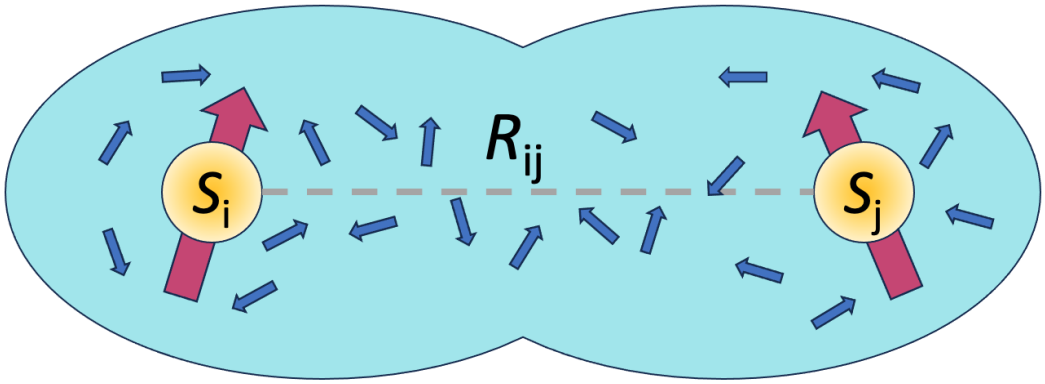


Fig. 1.1 Schematics of RKKY interaction.

The interaction can be expressed by the effective Hamiltonian: $H_{ij} = \sum_{i,j} J(R_{ij}) \cdot S_i \cdot S_j$, where $J(R_{ij})$ is the RKKY- coupling constant [7]:

$$J(R_{ij}) = \frac{J^2 k_F^6}{E_F} \frac{\hbar^2 V^2}{N^2 (2\pi)^3} F(2k_F R_{ij}) \tag{1.4}$$

The function $F(2k_F R_{ij})$ gives the interaction an oscillatory behavior (see Fig. 1.2).

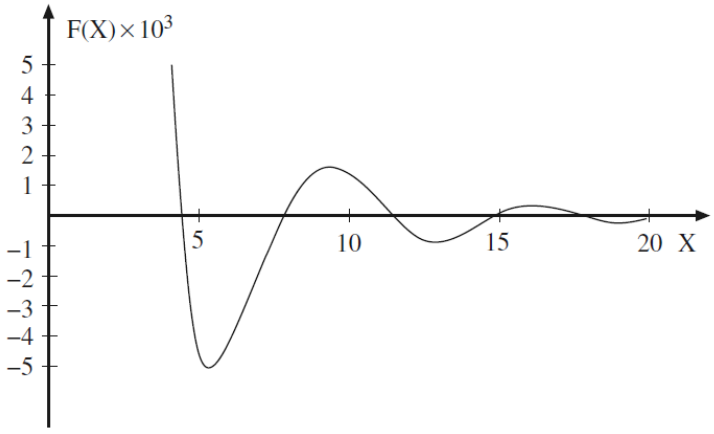


Fig. 1.2 Oscillatory behavior of the RKKY exchange is described by $F(X) = \frac{\sin X - X \cos X}{X^4}$, where $X = 2k_F R_{ij}$ [7].

The distance between magnetic ions $R_{ij}$ plays a crucial role in determining the ground state magnetism of the system. Depending on this interaction, the system can exhibit either ferromagnetism or antiferromagnetism. In contrast to direct exchange

interactions, which decrease exponentially with distance, RKKY interactions have a relatively larger range: $J(R_{ij}) \sim \frac{1}{R_{ij}^3}$, which also depends on the electron density ($n_e$) [7]: $J(R_{ij}) \sim n_e^{4/3} \sim (\frac{N_e}{V})_e^{4/3}$.

1.1.1.2. Itinerant systems

Band magnetism arises not from localized magnetic moments at individual atoms, but rather from the collective behavior of electrons occupying energy bands near the Fermi level. As a common example of itinerant systems, 3*d* metals are often mentioned with 3*d* electrons responsible for magnetism. The exchange interaction results in the energy splitting of electron states with different spins, leading to an unequal distribution of spin-up and spin-down electrons at the Fermi level. This disparity gives rise to a spontaneous magnetization characteristic of ferromagnetism.

The Hubbard model is employed to describe magnetism in itinerant electron systems. This model incorporates contributions from electron hopping between lattice sites and the on-site Coulomb interaction. Additionally, the Pauli exclusion principle is taken into account. The corresponding Hamiltonian is given by:

$$H = \sum_{ij\sigma} t_{ij} c_{i\sigma}^{+} c_{j\sigma} + U \sum_i n_{i\uparrow} n_{i\downarrow} \quad (1.5)$$

where $t_{ij}$ is the coefficient of electron hopping between sites, and $U$ is on-site Coulomb repulsion of electrons, $c_{i\sigma}^{\dagger} c_{j\sigma}$ are the creation and annihilation operators for electrons with spin $\sigma$. $n_{i\uparrow}$ *and* $n_{i\downarrow}$ are the ladder operators which give occupation number on site *i* with spins orientated up or down.

The conditions for spontaneous band splitting were originally introduced by Stoner, who considered nearly free electrons [8], which follow the Pauli exclusion principle (the same energy state can be occupied only by electrons with opposite spins). Stoner and Hubbard models become equivalent when a Mean Field Theory approximation is applied to the later one.

The description of the Stoner model is the following. The electron band states are filled up to the Fermi level $E_F$. The transfer of the electrons from the vicinity of the Fermi level (energy window between $E_F - \delta E$ and $E_F$) to the band with opposite spin direction is considered (Fig. 1.3). The new configuration will be more stable than spin-balanced one if the change of total energy $\Delta E < 0$.

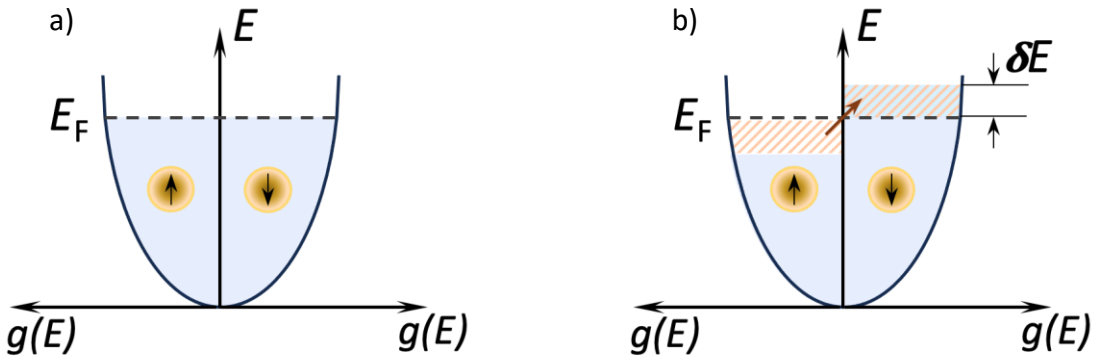


Fig. 1.3 Electronic bands with equal (a) and unequal occupation of the spin up and spin down states.

During this spin flip, kinetic energy increases. The change in kinetic energy depends on the density of states at the Fermi level $g(E_F)$, and it is given by: $\Delta E_{K.E.} = \frac{1}{2} g(E_F)(\delta E)^2$. At the same time, the potential energy decreases as electrons from the discussed energy range stop experiencing Coulomb repulsion, which occurs between two electrons with opposite spins on one energy level. The change of the potential energy can be expressed as $\Delta E_{P.E.} = \frac{1}{2} U(g(E_F)\delta E)^2$ ($U = \mu_0 \mu_B^2 \lambda$ is a correlation energy, or the increase of energy due to Coulomb interaction).

The total energy change can be expressed as:

$$\Delta E = \Delta E_{K.E.} + \Delta E_{P.E.} = \frac{1}{2} g(E_F)(\delta E)^2 (1 - U g(E_F)) \qquad (1.6)$$

and the condition for the spontaneous magnetization (i.e., unequal occupancy of spin-up and spin-down states being a stable configuration) is $Ug(E_F) \geq 1$ [9].

This criterion is known as the *Stoner criterion*. Achieving band polarization and ferromagnetic behavior requires a strong Coulomb interaction U and a high density of states at the Fermi level, $g(E_F)$.

### *1.1.2. Magnetism of actinide series*

The actinide series (atomic numbers ranging from 89 to 103) possess peculiar features. The electronic properties of actinides are primarily governed by their open 5*f* electronic shell, with partially occupied 6*d* and 7*s* outer states. In heavy actinides, this arrangement bears some resemblance to rare earth elements, where the unfilled 4*f* shell is deeply embedded within the atomic core and shielded by the 6*s* and 5*d* outer shells,

preserving the localization of 4*f* electrons even in solid state. Consequently, the magnetic moments of ions cannot directly interact with each other. However, due to such relativistic effect as strong spin-orbit interaction, Hund's rules (*L*-*S* coupling scheme, in particular) are broken in actinides and cannot be used for the description of atomic magnetic properties. This was experimentally proven for Pu [10].

Another notable difference between 5*f* and 4*f* elements lies in the larger spatial extent of the 5*f* wave functions, leading to overlap between neighboring atoms and the formation of a narrow 5*f* band in light actinide elements, similar to 3*d* bands in transition metals (first highlighted by Hill [11]). A significant distinction between 5*f* and 3*d* elements is the narrower band and much stronger spin-orbit interaction observed in 5*f*-electron systems, which couples the spin system with the crystal lattice. This results in big orbital moments even within a band scenario. Spin-orbit interaction gives rise to a remarkable magnetic anisotropy associated with the directions of *f*-*f* bonding [12]. Any reorientation of moments has a profound impact on conduction electrons, leading to the emergence of giant magnetoresistance and other spintronics-related phenomena.

With the increase of atomic number, the bandwidth decreases. The diminishing bandwidth promotes the localization of 5*f* electrons, causing them to move away from the Fermi level. The localization (Mott transition) threshold for elemental actinides falls between Pu and Am, as illustrated in Fig. 1.4.

Energy band calculations are sufficient to describe the behavior of light actinides, whereas heavy actinides require the inclusion of many-body physics [13]. This contrast is illustrated by the Wigner Seitz atomic radii of the 5*d*, 4*f*, and 5*f* elements, which show similarities between the light actinides and the *d*-electron series, and between the heavy actinides and the 4*f* series. The significant increase in atomic volume observed for localized 5*f* systems, as depicted in Fig. 1.4, correlates with the inter-actinide distances. The participation of 5*d* electrons in bonding exhibits a parabolic-like behavior, while the localization of 4*f* electrons results in minimal volume changes. The actinide series uniquely crosses the localization point within pure elements [4]. This critical point holds significant potential for exploring emergent phenomena of fundamental importance. However, it cannot be approached sufficiently smoothly in pure elements, necessitating tuning by chemical composition or other external parameters.

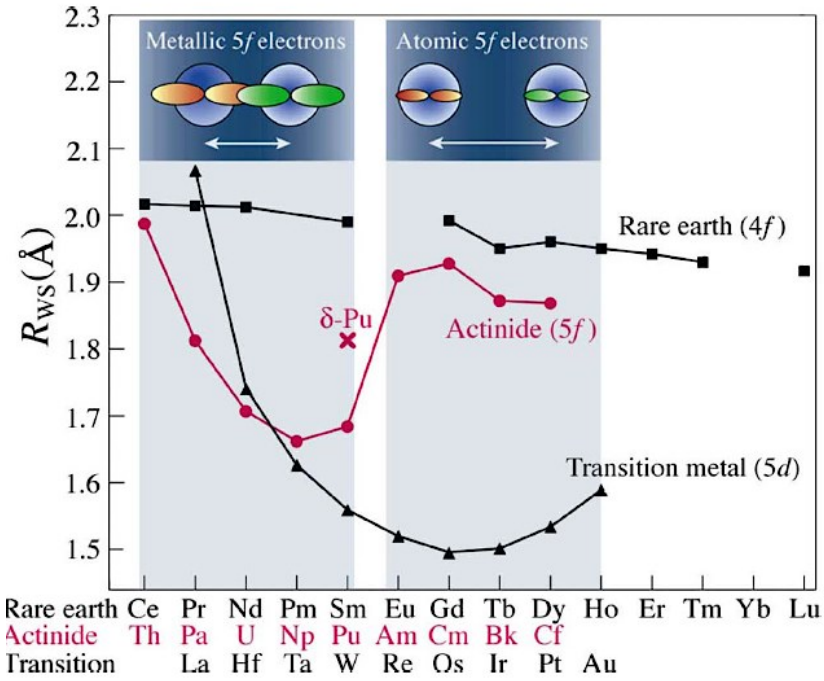


Fig. 1.4 The Wigner-Seitz atomic radii of the 5*d*, 4*f*, and 5*f* elements highlight the similarities between the light actinides and the *d*-electron series, as well as the heavy actinides and the 4*f* series [4].

Hill introduced a convenient scheme for light actinides, considering the shortest inter-actinide distances ($d_{An\text{-}An}$) in compounds [11]. The critical parameter known as the Hill limit ($d_C$) divides the "space" of actinide compounds into two regions: those with $d_{An\text{-}An}$ distances smaller than $d_C$ often exhibit superconductivity, while those beyond the limit tend to be non-superconducting and frequently magnetic. This behavior is attributed to the influence of direct 5*f* wave function overlap. Although Hill's original work included Ce alongside U, Np, and Pu, it is now understood that the loss of magnetism in Ce and Pu is driven by other mechanisms such as the Kondo effect or valence fluctuations. Nevertheless, the cases of U and Np highlight the significance of 5*f* overlap as a primary parameter in exploring the 5*f* states and their magnetism. But even for those elements a bunch of exceptions was found after decades of research.

In addition to the direct overlap between 5*f* orbitals, depending on inter-actinide spacing, 5*f* electrons are also subject to hybridization with the valence states of ligand atoms. This interaction plays a crucial role in determining the width of the 5*f* band,

ultimately impacting the degree of electron localization and consequently influencing the electronic and magnetic properties of actinides.

### *1.1.3. Magnetism of U compounds*

Uranium belongs to light actinide elements. The localization threshold of the 5*f* states, occurring between Pu and Am in pure elements, can be shifted to U in its compounds. The Hill limit for uranium compounds is between 3.40-3.60 Å. The ground state of systems with inter-uranium distance below this number is mainly superconducting [11], slightly above compounds become ferromagnetic (Fig. 1.5). With further increase of $d_{U\text{-}U}$ up to 4.0 Å antiferromagnetic ordering can be observed.

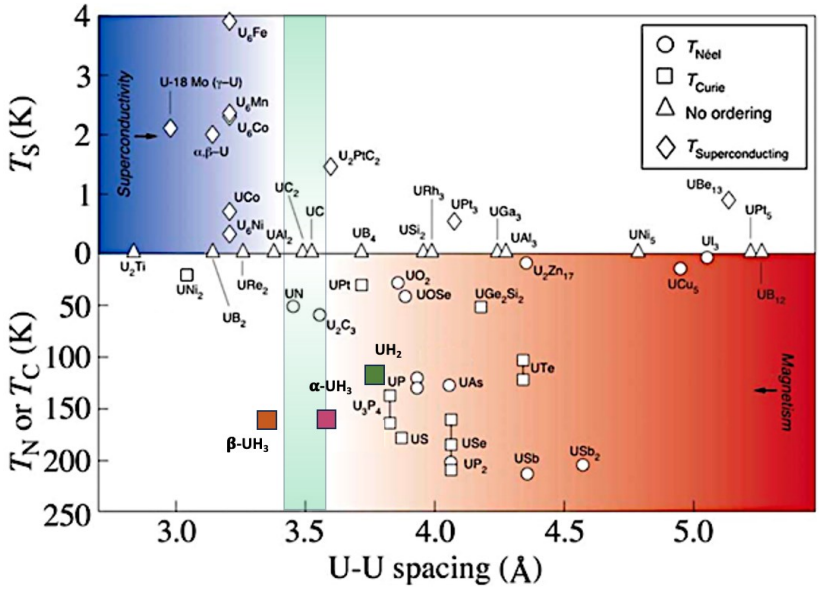


Fig. 1.5 "Hill plot" for selected U compounds taken from [4] which was modified according to the current state of knowledge. The red part of the graph represents the space of the magnetic compounds. The blue area corresponds to non-magnetic materials. Green area shows the Hill limit [11].

This straightforward rule does not consider details of the density of states, which can be influenced by the hybridization with ligand states. Consequently, the Hill limit has several known exceptions, such as $UNi_2$ [14], which exhibits magnetism despite having $d_{U\text{-}U} < 3.10$ A.

In the case of band magnetism, both the Curie temperature and the ordered moment are highly adjustable. For example, in UCoGe [15] both the ordered moment ($m_0$ = 0.07 $\mu_B$/U) and the Curie temperature ($T_C$ = 3 K) are relatively small

and can be easily suppressed to 0 K with a modest external pressure of 1.0 GPa. Similarly, in $UGe_2$, a pressure of 1.6 GPa is sufficient to reduce $T_C$ from 53 K to 0 K.

### *1.1.4. Superconductivity*

Superconductivity is a phenomenon observed in certain materials where they exhibit abrupt drop of electrical resistance to zero when cooled below a critical temperature ($T_c$).

When referring to conventional superconductivity (the prevailing majority of discovered superconductors), the expulsion of the magnetic field from the sample is spectated below the superconducting transition (Meissner effect). The Meissner effect is attributed to screening currents circulating within a thin surface layer of a superconductor. These currents generate a magnetic field that opposes the applied field, resulting in a zero net magnetic field within the superconductor.

The first theory which described conventional superconductivity was derived by Bardeen, Cooper, and Schrieffer [16]. According to conventional BCS theory, lattice vibrations, or phonons, induce an attractive interaction between electrons, leading to the formation of spin-singlet Cooper pairs. These pairs consist of electrons with opposite spins and zero angular momentum (behaving as bosonic particles), collectively reducing the ground-state energy of the electron system and forming the superconducting condensate. The condensate enables dissipationless transport.

External magnetic field suppresses superconductivity, and critical temperature decreases. There exist two types of conventional superconductors. Type I has one critical field ($H_c$), above which superconductivity is lost. Type II superconductors have two critical fields ($H_{c1}$, $H_{c2}$), between which sample exists in the intermediate state, so part of it is in the superconducting state and part is in the normal state [17]. The upper critical field in superconductors with weak electron-phonon coupling is given by the Werthamer–Helfand–Hohenberg (WHH) theory, which predicts a universal function $H_c$ vs. $T$, quadratic in $T$. It provides the $T \to 0$ limit value [18]

$$H_{c2}(0) \approx 0.7 \cdot T_c \cdot (-\mathrm{d}H_{c2}/\mathrm{d}T) \tag{1.7}$$

According to BCS theory, the binding energy of the Cooper pair ($\Delta$) is the only parameter determining the properties of the superconducting state. From absolute zero up to the critical temperature, the DOS of the BCS superconductor is defined by the

energy gap of $2\Delta$ around the Fermi energy. All electrons below the gap are coupled. The specific heat of a material in a superconducting state exceeds that in a normal state. The difference between the specific heats near $T_c$ can be approximated by the formula: $\Delta C = C_S - C_N = 1.43\gamma T_c$. Consequently, $\Delta C/\gamma T_c = 1.43$ serves as the primary indicator of a weak-coupling superconductor, with higher $\Delta C/\gamma T_c$ values typically indicating materials falling within the strong coupling regime.

The strength of superconductor is described by the coherence length $\xi_0$. It represents the distance over which the two electrons in a Cooper pair are bound together. It can be derived from the upper critical field $H_{c2}$ at absolute zero in the framework of the weak-coupling theory [19]:

$$\mu_0 H_{c2}(0) = \frac{\Phi_0}{2\pi\xi_0^2} \tag{1.8}$$

where the flux quantum $\Phi_0 = h/2e = 2.068 \times 10\text{-}15$ T·m$^2$.

An exotic group of unconventional superconductors (UcS) contains materials with non-phononic superconducting mechanisms [15]. In those Cooper pairs consist of electrons with parallel spins (spin-triplets) and finite angular momentum $L = 1$ ($p$-wave superconductivity) or $L = 2$ ($d$-wave superconductivity). Such unconventional superconductors have extraordinary properties (coexistence of magnetic and superconducting ground states, etc.). The attractive interaction between coupled electrons is mediated by spin fluctuations of magnetic moments.

## *1.2. Basic information on U and U hydrides*

### *1.2.1. Uranium metal*

Uranium metal exists in three allotropic modifications (Fig. 1.6) below the melting point (1407.8±2 K). α-U is a phase stable at room temperature (RT) and ambient pressure. It crystallizes in the orthorhombic structure with the space group *Cmcm* and lattice parameters $a = 2.85$ Å, $b = 5.87$ Å, and $c = 4.95$ Å [20], the density $\rho = 19.07$ g/cm$^3$ and the shortest inter-uranium distance $d_{U\text{-}U} = 2.837$ Å. There are three transitions below $T = 43$ K connected with structural instabilities, described as charge-density waves (CDW) [21]. α-U is a weak Pauli paramagnet with almost temperature-independent susceptibility [22]. Due to the stability of this phase, its electronic properties are the most studied among uranium allotropes.

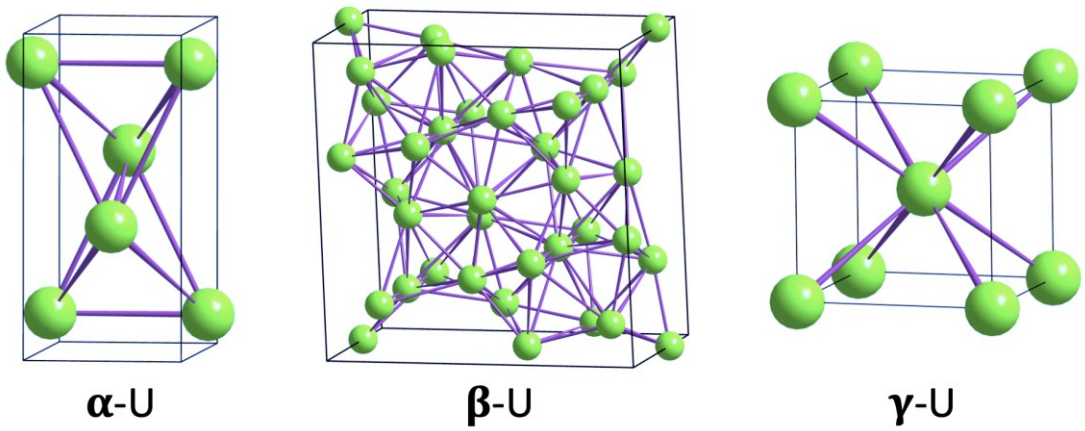


Fig. 1.6 Allotropic modifications of Uranium.

β-U exists between 940 – 1045 K with a tetragonal structure (space group $P4_2/mmm$, $a = b = 10.52$ Å, $c = 5.57$ Å), $\rho = 18.17$ g/cm$^3$, $d_{U\text{-}U} = 2.889$ Å. γ-phase (γ-U) with a body-centered cubic (*bcc*), space group $Im\text{-}3m$, $a = 3.47$ Å, A2-type structure is stable above 1045 K, $\rho = 17.94$ g/cm$^3$, $d_{U\text{-}U} = 3.067$ Å. Each U atom in the A2 arrangement is surrounded by 8 equidistant atoms which form a cubic coordination polyhedron.

There is a keen interest in characterizing low-temperature properties of the cubic γ-U phase due to its improved mechanical properties and behavior under irradiation. Retention of the high-temperature phase to room temperature through alloying with transition metals (4*d* and 5*d* elements) enabled the use of a wide variety of experimental techniques. In addition, applying ultrafast cooling techniques (e.g., splat cooling) allows for the reduction of the concentration of alloying elements needed for the stabilization of the pure cubic phase. For instance, in the case of Mo substitution, 16.5 at. % Mo required for γ-U phase in normal furnace conditions can be reduced to only 8 at. % Mo for splat-cooled samples [23]. The minimal Zr concentration needed for stabilization of single-phase γ-U sample by fast cooling was reported to be 30 at.% Zr [24]. As a bonus, alloying increases the corrosion resistance of the examined material.

Uranium metal, a typical example of light actinides, exhibits weak Pauli paramagnetism with a broad 5*f* band. However, this behavior can be altered in alloys and compounds, where the 5*f*-5*f* spacing expands or hybridization with non-*f* states is weak. From a fundamental research perspective, the 5*f* electronic states in many

uranium-based compounds are on the brink of localization, making them captivating subjects for the study of many-body systems.

### *1.2.2. Hydrides*

As discussed earlier, *f*-electron systems are highly responsive to changes in interatomic distances, which can significantly alter their electronic properties in response to external factors or compositional changes. Consequently, studying compounds under pressure is crucial for gaining a deeper understanding of their electronic structure and corresponding physical properties.

Hydrogenation is sometimes considered as “negative” pressure as, in the vast majority, the hydride lattice is expanded compared to the parent compound. Hydrogenation offers insights beyond those gained from standard experiments conducted under hydrostatic pressure using parent compounds.

The crystal structure of a hydride is influenced by the structure of its parent compound and the conditions (temperature, pressure) during the hydrogenation process. Hydrogen atoms tend to occupy specific interstitial sites, with octahedral and tetrahedral being the primary types of sites in simple crystal structures.

For a compound to form a hydride, certain conditions must be met, including geometrical factors, crystal structure, surface properties, electronic factors, and diffusive kinetics. Geometrical criteria, such as Westlake's criterion, play a role in predicting hydride formation, which states that the parental metal (compound) should have available interstitial sites with a spherical volume radius of $\geq 0.4$ Å [25,26]. Additionally, the minimum H-H distance should be 2.1 Å, and the Shoemaker's exclusion rule dictates that two tetrahedra of one face cannot be simultaneously occupied. While these criteria aid in prediction, exceptions are numerous, highlighting the complexity of hydride formation. When samples are prepared by deposition, these rules are even more blurred.

Until very recently, uranium hydride has been known in two modifications of trihydride, namely, β-$UH_3$ and metastable α-$UH_3$. That situation was exceptional as most actinides and lanthanides are presented in both di- and trihydride modifications. Nevertheless, uranium dihydride $UH_2$ has been prepared only in a thin film form by our group, and one of the objectives of the current work was the identification of deposition parameters that stimulated the growth of the new phase.

The crystal structure of the trihydrides described below corresponds to bulk samples. While $UH_3$ films possess the same structures as their bulk counterparts, lattice parameters may vary significantly and will be addressed in the section on experimental results (Section 3.3).

α-$UH_3$ forms in the early stage of uranium hydrogenation and transforms fast into β-$UH_3$ at elevated temperatures [27]. Usually, α-$UH_3$ is prepared during a slow reaction at low temperatures in a mixture with a large portion of the β-$UH_3$ phase. That was the reason for the uncertainly defined ground state of this phase until the discovery of the Zr substitution effect on the stabilization of α-$UH_3$ [28]. α-$UH_3$ has a cubic crystal structure (space group *Pm-3n*) (Fig. 1.7 (a)) and lattice parameter $a = 4.160$ Å [29]. Uranium atoms occupy (0,0,0) and (1/2,1/2,1/2) sites, and six hydrogen atoms ±(1/4,0,1/2), ±(1/2,1/4,0), and ±(0,1/2,1/4) sites which form an icosahedron (yellow lines on Fig. 1.7) [22,29]. The shortest inter-uranium distance is close to 3.6 Å, which is slightly above the Hill limit.

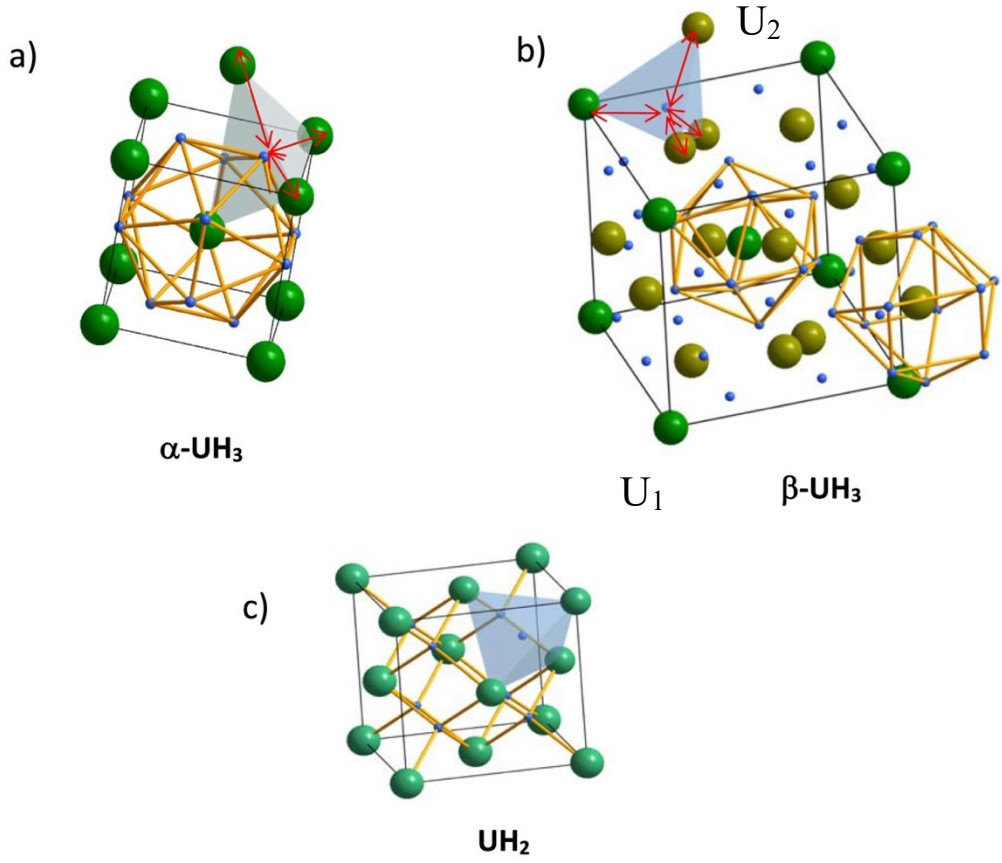


Fig. 1.7 The crystal structures of binary U hydrides with indicated U4 tetrahedra containing the H positions. In β-$UH_3$ (b) the two U sites are distinguished by different shades of green. The 2*a* Wyckoff position positions are dark ($U_1$), 6*c* positions are light ($U_2$) [12].

β-$UH_3$ has also a cubic structure, CrSi structure type (*Pm3n* space group) and lattice parameter $a$ = 6.644 Å. Uranium atoms occupy two different positions: 2 atoms $U_1$ (dark green on Fig. 1.7) in (0,0,0) and (1/2,1/2,1/2); and 6 atoms $U_2$ in ±(1/4,0,1/2) and their equivalent positions [22]. Hydrogenation starts at room temperature and low H pressures, and this is a primary concern regarding the aging or degradation of uranium metal products. Pure β-$UH_3$ is a very fine powder that easily ignites at room temperature in air.

For the first time uranium dihydride was deposited on Si substrate [5]. The analysis has shown the cubic *fcc* $CaF_2$ (*Fm3m*) structure type. The lattice parameter is $a$ = 5.36 Å (similar to that of Np and Pu dihydrides).

Both α- or β-$UH_3$ are based on the *bcc* U lattice. In the latter case, the lattice is expanded by adding U positions on the faces of the cube, but not in the centered positions. Despite the *fcc* $CaF_2$ ($UH_2$) structure not bearing any resemblance to α- or β-$UH_3$, hydrogen occupies almost identical U tetrahedra in all three cases with the same shortest U−H distance 2.32 Å. In the case of β-$UH_3$, tetrahedra are slightly distorted, and for the $UH_2$ those tetrahedra do not fill the space entirely, which is reflected in the lower density (10.41 g/cm$^3$ compared to 10.91 g/cm$^3$ for β-$UH_3$).

Uranium hydride is a reference material for understanding 5*f* magnetism in light actinides, having been identified as the first 5*f* ferromagnet several decades ago [30]. Back then, the emergence of ferromagnetism was attributed to the volume expansion of uranium metal (which can reach approximately 60%). Nonetheless, there are a few discrepancies telling against the dominance of Hill physics (and inter-uranium distance as a decisive parameter) in this system. Firstly, β-$UH_3$ shows a relatively high Curie temperature $T_C$, around 170 K, whereas $d_{U\text{-}U}$ = 3.31 Å is below the Hill limit (≈ 3.4 Å). Secondly, α-$UH_3$, having a different crystal structure and inter-uranium spacing (3.6 Å, above Hill limit), possesses the same $T_C$ and bulk magnetization close to 1.0 $\mu_B$ as a stable hydride phase. In addition, following the logic of conventional Hill physics, $UH_2$ should be more magnetic than trihydrides (due to the longest $d_{U\text{-}U}$ = 3.78 Å among three phases), but experiments have shown a much lower $T_C$ of 120 K [5]. Assuming that U-H bonding is prominent, the lower H/U ratio in uranium hydride would suggest weaker magnetism, which is reflected in the experimentally established transition temperatures. The similarity of U tetrahedra occupied by the H atom in all three phases is another hint at the importance of polar bonding.

Only the combination of two parameters (the inter-uranium spacing and the charge transfer between U atom and ligand) would give an adequate description of the magnetism in uranium hydrides. While polar bonding is traditionally associated with ionic compounds like oxides, it is also relevant in systems exhibiting metallic or semi-metallic properties, such as hydrides. Although the concept of polar bonding is not novel, its influence in systems with conduction electrons is often mitigated by long-range Coulomb screening.

Recent calculations shed light on the electronic structure of the hydrides and their corresponding magnetic properties. Data were obtained from the Density Functional Theory (DFT) utilizing the Vienna *ab initio* simulation package (VASP) [31]. It was shown that in all three hydrides close to the $E_F$ there are mainly the U-5*f* states with some contribution from the 6*d* states. In α-$UH_3$ and β-$UH_3$, the 5*f* states nearly vanish at the Fermi energy, contrasting with $UH_2$, where a substantial number of 5*f* states persists. This phenomenon suggests a more itinerant nature of the 5*f* states in $UH_2$, which contrasts with Hill physics.

The calculations indicate a polar nature of the U-H bonds and strong hybridization of valence 6*d* states of uranium with hydrogen 1*s* states. There is a relatively high occupancy of 5*f* orbitals, ranging from 2.7 to 2.8 electrons per uranium atom. Concurrently, the U-6*d* states experience partial depopulation due to bonding with H-1*s* states, resulting in a significant electron transfer towards hydrogen. This is reflected in positive Bader charges exceeding 1 |e| per uranium atom. The higher Bader charges observed in both $UH_3$ variants compared to $UH_2$ are correlated with the lower Curie temperature in dihydride. This suggests the crucial role of charge transfer in decoupling the 5*f* and 6*d* states and narrowing the 5*f* sub-bands. The variations in the 6*d* states, which are partially hybridized with the H-1*s* states and partially shifted slightly above the Fermi level, play a supportive role in the magnetism of the 5*f* states.

The discrepancy between the calculated Sommerfeld coefficient of electronic specific heat of < 10 mJ/mol K for all the hydrides (note here, for α-U single crystal $\gamma_e$ = 9.13 mJ/mol K [32]), and the experimental values of 30 mJ/mol·K observed in both $UH_3$ variants [28], can be attributed to the high spectral density of quasiparticle states contributing to the experimentally obtained heat capacity values. This phenomenon is also evident through high-resolution Ultraviolet Photoelectron Spectroscopy [33].

The ferromagnetic arrangement, characterized by magnetic moments aligned along [111], is favored for $UH_2$ and $\alpha$-$UH_3$. However, a more intricate arrangement is observed for $\beta$-$UH_3$.

In the case of $\beta$-$UH_3$, the magnetization of the 2*a* sublattice is constrained by symmetry along the body diagonal [111], but the 6*c* sublattice exhibits deviations of approximately 10 degrees. These deviations occur towards the directions of individual chains, along which the U-6*c* atoms are situated. This non-collinearity may be associated with the observed difficulty in achieving magnetic saturation in $\alpha$-$UH_3$ compared to $\beta$-$UH_3$ [28]. In all three hydrides, the spin and orbital moments were obtained mutually antiparallel, as usual in U systems.

In addition to fundamental aspects, practical applications of actinide (primarily uranium) hydrides also hold significant promise, particularly in the realm of hydrogen (deuterium, tritium) storage. Despite their unsuitability for mobile applications due to their high atomic mass, these hydrides offer advantages for stationary applications, including a high volumetric density ($\approx 130$ g/cm$^3$), moderate prices of depleted uranium, and notably, a substantial difference (seven orders of magnitude) in equilibrium pressure of $H_2$ on U, ranging from as low as $10^{-2}$ Pa at room temperature to $10^5$ Pa at 700 K. Uranium metal serves as an effective getter, capturing valuable tritium in nuclear fusion devices at room temperature and releasing it again at moderate temperatures [34]. Moreover, the robustness of hydrogen absorption in uranium, even in the presence of oxygen, enables its use for hydrogen purification [35]. Uranium hydride can also be integrated into nuclear fuel for light-water reactors [36], with thorium hydride being considered for advanced burner reactors [37].

### *1.3. Experimental techniques*

In terms of overall strategy for sample preparation, several essential questions must be addressed:

1. Material type: What kind of material is needed — pure metal, compound, heterostructure. This choice will be the primary determinant in selecting the synthesis method.

2. Goals: what are samples meant for? Structure analysis, surface reactivity, electronic structure, or physical properties. This affects the choice of substrate type, film thickness, requirements to the crystallinity, etc.

3. Starting Material: How much initial material is required and available? Should the initial material be a compound from the outset, or is it preferable to create the composition during the deposition process? Even if the initial material has the correct composition, it may be necessary to modify one or more parameters during growth.

4. Sample Quantity: How many samples are needed? Some synthesis techniques are more suitable for high-throughput production than others.

5. The need for additional layers — such as capping layers to prevent surface oxidation or buffer layers to provide a chemical barrier and mediate lattice mismatch between the substrate and film — affects the choice of synthesis method as well.

These considerations are critical for optimizing the synthesis strategy to achieve the desired material properties and meet application requirements. A variety of methods utilizing chemical or physical processes can be employed for the preparation of U-based thin films [38].

### *1.3.1. Reactive DC sputter deposition*

Sputter deposition is a method of thin film deposition based on the sputtering of a high-purity source material (called a cathode or target) by subjecting it to plasma [39]. It belongs to a group of physical vapor deposition (PVD) methods, which are by far the most frequently adopted techniques in the field of actinide films. In these methods, the material enters the vapor phase from the dense state and returns to the dense phase as a thin film.

In the most straightforward set-up, so-called diode sputtering, a difference in electrical potential is applied between the target and a substrate to form a plasma inside a vacuum chamber. Free electrons are emitted from the negative potential electrode (cathode) and accelerated by the electric field. Electrons collide with neutral gas atoms in their path, causing their ionization. Positive ions accelerate then towards the cathode, causing the sputtering phenomenon. Target atoms are condensed on the substrate. Some ions return to the ground state by absorbing electrons and releasing photons, causing glow discharge. Depending on the target material, the applied voltage can be DC (with constant polarity) or RF (with alternating polarity). In particular, DC sputtering is suitable for electrically conductive materials. The main drawback of the setup is a low deposition rate which can be eliminated by implementing a triode

scheme (Fig. 1.8). In this case plasma is stabilized by a third electrode, filament, which ejects thermally excited electrons. The higher number of electrons significantly increases the efficiency of the ionization process and sputtering.

Sputtered atoms have a wide energy distribution, typically up to tens of eV. Only less than 1% of ejected particles from the target are ionized. However, they can ballistically fly from the target in straight lines and impact the substrates causing re-sputtering. By increasing the pressure, the ion collision probability with a gas atom can be enhanced [40]. Such scattering decreases the energy of ions, leading to their condensation on the substrate.

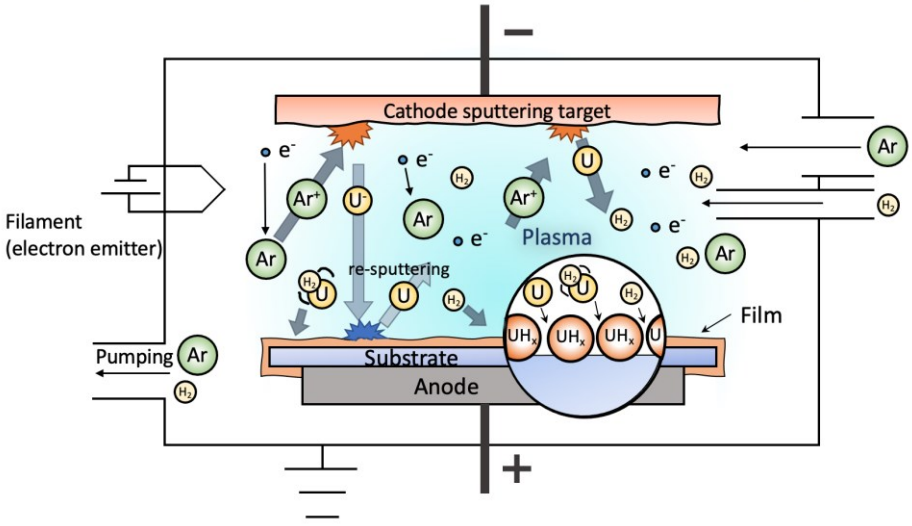


Fig. 1.8 Reactive sputter deposition (triode scheme).

There are two main requirements for the working gas: first, the atomic weight of the sputtering gas should be close to the atomic weight of the target for efficient momentum transfer, and second, it should be inert (must not react with the target) [39]. The most commonly used gas is Argon (Ar) which was proven to be effective for sputtering actinides [41–44]. An average Ar pressure is ~$10^{-3}$ mbar and depends on the specific set-up of each vacuum system. While depositing intermetallic compound (from a stoichiometric target or from separate targets), the composition of such compounds may be controlled by the Ar pressure to a certain extent [41]. If the sputter deposition process can produce stoichiometric replicas of complex materials, it could facilitate surface analysis without the need to cleave or scrape the bulk materials in order to obtain a clean surface XPS studies. This would overcome the limitation of conducting only a few measurements on a single sample.

Films of not only metals, intermetallic compounds and alloys can be prepared by sputter deposition. If the sputtering of an elemental target is performed in the presence of a reactive gas, sputtered particles undergo a chemical reaction, and a compound film is formed. This method is called reactive sputter deposition. By adding nitrogen, oxygen, or hydrogen to the working gas, thin films of nitrides, oxides or hydrides can be obtained [45]. At first glance, this may seem very simple. However, the deposition parameters are significantly affected by the presence of reactive gas, and establishing perfect conditions for film deposition is getting even more tricky. Additionally, the reaction mechanisms between the sputtered material and the reactive gas may cause some process (in)stability problems [46].

The compound can be formed on a substrate (preferable), in-flight, or on the target surface. The latter reaction leads to the classic reactive sputtering problem. The sputtering rate for the compound that forms on the target is usually significantly lower than the rate for the elemental target with the same amount of power delivered to the target. With the increase of the target coverage, the deposition rate decreases. When the entire target surface is covered with the compound material, the target is denoted as poisoned [47].

The relationship between the film composition and reactive gas supply is non-linear. In fact, most reactive-based sputtering processes are characterized as hysteresis-like [45,46], and complete control of the involved parameters is needed. Nevertheless, due to the instability of the process and the complex nature of the glow discharges, the number of essential parameters for a quantitative and complete description of reactive sputtering is not evident. A simple model was suggested by Berg et al. [46], which can describe the hysteresis loop of some experimental parameters. Implementing this model for each specific experimental set-up makes it possible to predict optimum processing conditions where both high rate and stoichiometric film composition may be obtained. Even though the model does not take into account the properties of the plasma, non-uniformities in gas kinetics, complex chemical reactions, and ion implantation of the reactive gas, it gives appropriate agreement with an experiment.

During reactive sputter deposition from an alloy or several targets simultaneously, one should keep in mind that the reactivity of each element with reactive gas and the deposition rates of these compounds might be different, so it is crucial to keep the partial pressure of a reactive gas stable during the whole deposition.

Due to a significant number of parameters available for tuning the deposition process, reactive sputter deposition provides a significant degree of control over the physical properties and microstructure of grown films.

Among other sputtering techniques frequently used for the preparation of U-based thin film are DC magnetron sputtering, pulsed laser deposition (PLD) and Molecular beam epitaxy (MBE).

### *1.3.2. RGA*

Controlling the reactive gas flow is the most straightforward approach during reactive sputtering. However, given that reactive sputtering typically operates in the poisoned mode of the target, the deposition rate is comparatively low in comparison to that from an elemental target, and the partial pressure of the reactive gas is not linearly proportional to the gas flow. Moreover, film properties generated by reactive sputtering with flow control are far from optimal. Control of partial pressure is more complicated and necessitates active feedback control. Nonetheless, this method enables the process to operate in the transitional region between the elemental and poisoned states of the target, resulting in higher deposition rates. Furthermore, it enables keeping the pressure of a reactive gas stable, enhancing the quality and homogeneity of deposited films [47].

A residual gas analyzer (RGA) is one of the instruments that can be used for partial pressure control. It is a small mass spectrometer. The most common type is a quadrupole mass analyzer with an open ion source (OIS, used in our studies) mounted directly to the vacuum chamber. Residual Gas Analyzers measure pressure by sensing the weight of each atom as they pass through the quadrupole. In the OIS type, the filament wire and anode wire cage are exposed to the surrounding vacuum chamber so that all molecules can move easily through the ion source. Analyzer consists of four metal rods parallel to each other. The mass analyzer selects sample ions based on their mass-to-charge ratio (*m/z*). The opposing pairs of rods are connected electrically and subjected to a radio frequency (RF) voltage combined with a DC offset voltage. Ions travel down the quadrupole between the rods. The trajectory of ions only with a specific mass-to-charge ratio is stable, allowing them to reach the detector while other ions collide with the rods. By varying the applied voltage, the operator can scan for a range of *m/z* values. For optimal performance, the rods should have a hyperbolic shape.

However, cylindrical rods with a specific ratio of rod diameter to the spacing between rods can provide an adequate approximation to hyperbolas, with the added advantage of being easier to manufacture. Even minor variations in the ratio can significantly impact the resolution and peak shape [48].

The biggest issue is that the maximum operating pressure of the analyzer is $10^{-4}$ mbar while the pressure of the working gas during deposition is $10^{-3}$ mbar, thus, some technical "trick" must be used to enable proper performance of the mass spectrometer. In our studies, a vacuum chamber with a sputter source was connected to a different vacuum chamber through a needle valve, RGA was attached to a second vacuum chamber.

### *1.3.3. XPS, UPS, BIS*

Photoelectron spectroscopy (PES) is an experimental technique based on the energy measurement of electrons emitted from the examined substance by the photoelectric effect, in order to determine the binding energies of electrons. Depending on the ionization energy, the method is divided into X-ray photoelectron spectroscopy (XPS), Ultraviolet photoelectron spectroscopy (UPS), Extreme ultraviolet photoelectron spectroscopy, etc.

#### 1.3.3.1. X-ray photoelectron spectroscopy

XPS has become a standard analytical tool for investigating near-surface regions of solids, primarily due to its exceptional diagnostic capabilities. It enables both quantitative and qualitative elemental analysis of the specimen, along with the identification of the chemical states of present elements (local environment of the examined atom) and local electronic structures of the materials. The detection limits are within 0.1 - 1 at.% depending on the species [49].

Fig. 1.9 shows the basic components of an XPS system. The system includes an X-ray source, possibly with a focusing optics and monochromator, an electron energy analyzer with appropriate electron optics to transmit photoelectrons through the analyzer. In the majority of modern instruments, a hemispherical analyzer is used to determine the kinetic energy of photoelectrons. The photoelectrons travel between two charged co-hemispherical plates. Electrons with too high or too low kinetic energy collide with one of the plates. Only electrons within a narrow range of energies (the

"pass energy") get to the detector. Typically, detectors operate at a fixed pass energy, and a retarding lens prior to the analyzer is used to scan across the energy range of photoelectrons.

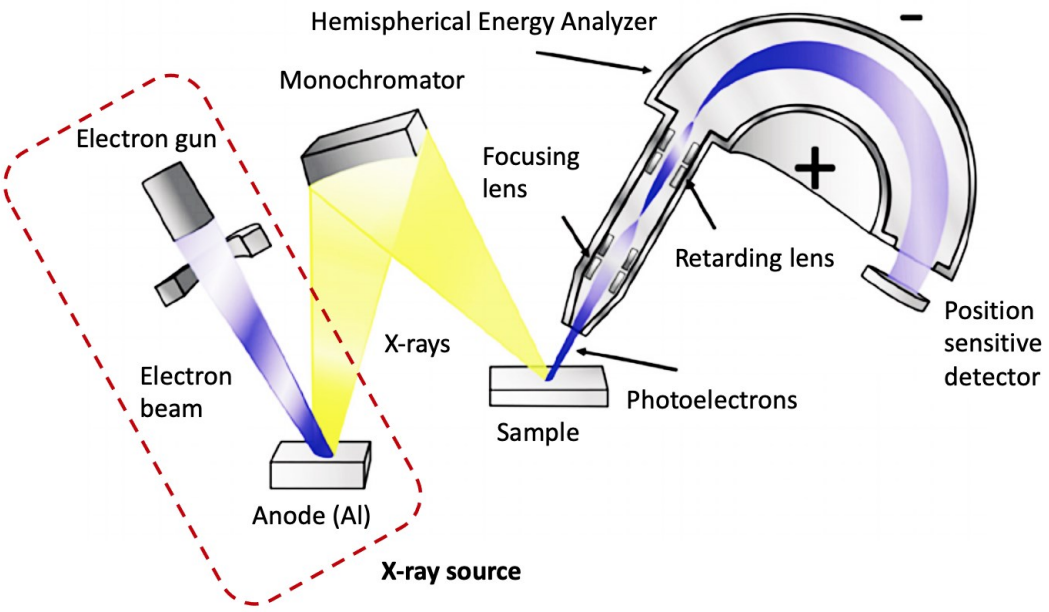


Fig. 1.9 Schematic representation of an XPS system [49].

An electron gun is used to excite characteristic X-ray emission from a metal anode. Aluminum (Al) is the most common material because of its relatively narrow Kα line (1486.6 eV). In our case we used in addition an X-ray monochromator. This reduces the spectral width of the exciting radiation and eliminates unwanted photoelectron excitations of other types, e.g., Bremsstrahlung from the anode, removing the background in spectra and reducing thus the spectral noise. Besides aluminum anodes, magnesium and silver are sometimes installed.

Standard XPS instruments usually operate in the ultra-high vacuum (UHV) regime, with vacuum better than $10^{-9}$ mbar to keep sample surface clean for a reasonable time and to provide sufficient mean free path of the photoelectrons after their excitation. Our equipment dedicated to highly reactive actinides was designed for the base pressure of the order of $10^{-11}$ mbar.

Possibilities are enhanced by a combination of XPS and UPS in one vacuum chamber. UPS using UV photons from a gas discharge lamp is much more limited as to the energy range covered and is also more sensitive to the very surface, but the very narrow natural line width provides much better energy resolution. In general, the experimental energy resolution is determined by a combination of the resolution of

electron energy analyzer and monochromatization of the X-ray beam and can be ultimately as small as 0.5 eV (defined by the full width at half maximum - FWHM - of a core level peak). Better resolution can be achieved by decreasing the Pass Energy value. However, lower Pass Energy produces lower Electron Count-Rate, and consequently data must be collected for a longer time to get a useful signal-to-noise ratio. Using UPS, there is no need for monochromatization. Very high intensity allows to work with low pass energies and the characteristics of an electron energy analyzer is the only factor determining the experimental energy resolution, which was typically ≈ 70 meV for the instrument used in these studies.

As mentioned above, the physics of XPS is based on the photoelectric effect. Fig. 1.10 depicts the basic principle. Atom absorbs photon of a definite energy $h\upsilon$ and ejects a core or valence electron with binding energy $E_B$. This electron leaves the sample with kinetic energy $E_{Kin}$ and is detected by the analyzer.

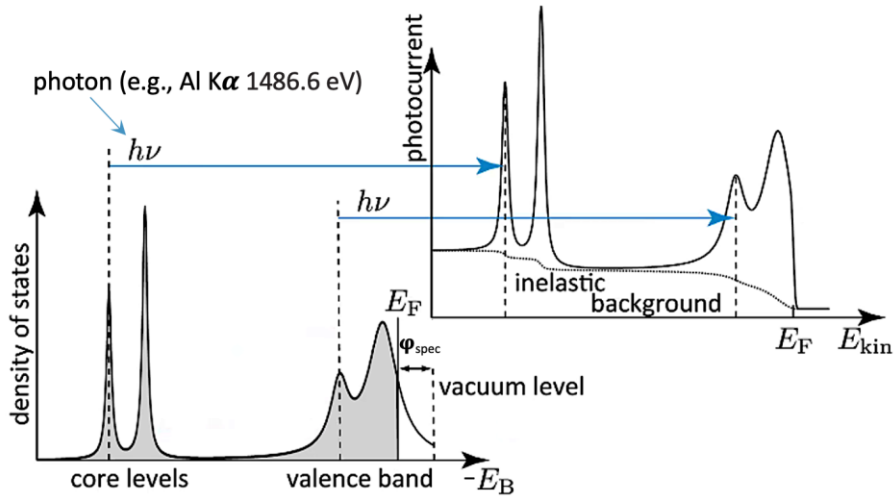

Fig. 1.10 Energy scheme of the photoelectric process in the XPS.

The principal formula of photoeffect is following:

$$E_{Kin} = h\nu - E_B - e\varphi_{spec} \tag{1.9}$$

where $E_{Kin}$ is the kinetic energy of the photoelectron, h is the Plank constant, $\upsilon$ is the frequency of the photon, $E_B$ – the binding energy of the photoelectron with respect to the Fermi level of the sample ($E_B$ at the Fermi level equals 0) and $e\varphi_{spec}$ is the work function of the spectrometer (as the sample is electrically connected to the spectrometer, it is not the work function of a sample). If the spectrometer and the sample are indeed in electrical contact, their Fermi levels are lined up.

Binding energy is the energy required to remove electron from the atom, which depends on the element, the core level from which they are ejected, and the chemical environment of the atom. In the general case, binding energy is not equal to the energy of the orbital from which this electron was emitted (the relaxation processes caused by the reorganization of the remaining electrons of intra- and extra-atomic origin contribute to the kinetic energy of the photoelectron). However, the set of binding energies is characteristic of an element. And due to the dependence of the kinetic energies of the emitted electrons on their binding energies, XPS can be used to analyze the composition of samples [50].

The depth of analysis (information depth), $d$, is taken as $d = 3\lambda\sin(\alpha)$, where $\lambda$ is the inelastic mean free path (IMFP) of the photoelectrons through the sample, $\alpha$ is the take-off angle (Fig. 1.11 (a)) or the angle between the exited photoelectrons and the surface. IMFP is the depth, measured normal to the surface, at which the intensity drops to 1/e of its original value. If electrons are detected on the normal to the sample surface, 99% of the signal originates from distance 3λ within solid. This distance is often approximated to 10 nm, even though IMFP is dependent on the material properties (atomic number Z, density, etc.) and the kinetic energy of electrons. In principle, the measurement of the IMFP is not as trivial and easy as it might seem, the "overlayer method" is usually used [50]. The minimum IMFP between 50-100 eV implies that UPS is generally more surface sensitive than XPS (Fig. 1.11 (b)).

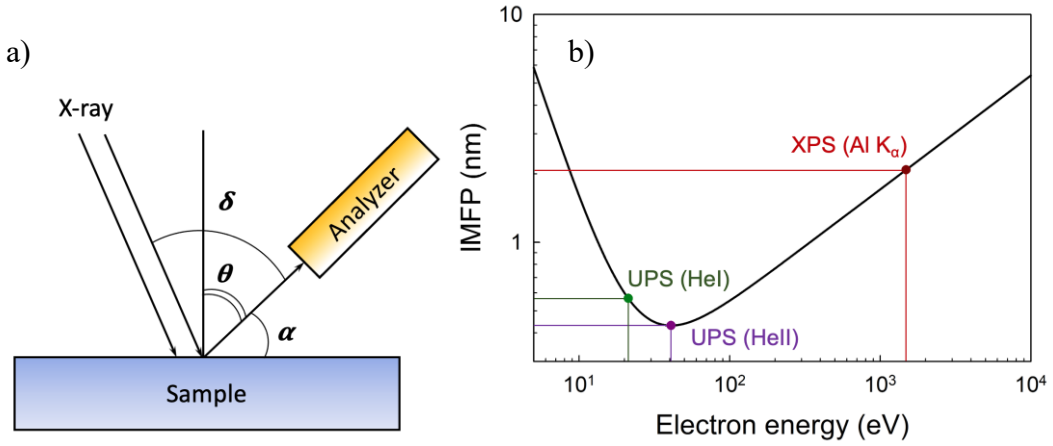


Fig. 1.11 (a) Simplified geometry of XPS and (b) universal curve for the electron inelastic mean free path in pure elemental materials according to Seah and Dench [51].

Commonly, data is collected at only one take-off angle, however, in a more advanced mode, angle-resolved photoelectron spectroscopy (ARPES), photoelectrons

are collected as a function of take-off angle for a single crystal, which allows the mapping of dispersion relations of electrons in bands (energy versus ***k***-vector) in the ground state.

One difficulty connected with the measurement of insulating samples (or thin films on an insulating substrate) is electrostatic surface charging. It affects XPS measurement and subsequent analysis of the spectrum. The charging effect occurs due to the inability to compensate the positive potential obtained by the emission of photoelectrons because of the lack of electrical contact between the sample and the instrument. The influence of the charging on the spectrum consists mainly in the shift of the energy scale towards lower kinetic energies and broadening of the peaks. The most common method to overcome charging is the replacement of photo-emitted electrons with electrons from a low-energy source (flooding gun), however, the absolute positions of the peaks might be still slightly incorrect [52].

***Spin-orbit splitting***

For core level, the spin-orbit interaction is much stronger than electron-electron Coulomb interactions. Core levels in XPS are then indexed with $nl_j$ [53] (for example, U-4$f_{7/2}$) where $n$ is the principal quantum number, $l$ is the angular momentum quantum number and $j = l + s$ (where $s$ is the spin angular momentum number, can be ±½). After the photoionization process, an unpaired electron is left behind. If the core hole belongs to an orbital with non-zero orbital angular momentum (all orbitals except the $s$ levels) there will be a coupling between the unpaired spin and the orbital angular momentum. This coupling gives rise to a doublet [54] (two possible states with different binding energies for the cases of "parallel" or "anti-parallel" nature of the spin). This is known as spin-orbit splitting (or $j$-$j$ coupling) [55]. The area ratios of the doublet peaks are given by the ratio of corresponding degeneracies, i.e. the number of different combinations that can give rise to the total $j$ (equals $2j$+1). For example, for the 4$f$ spectra, where $n$ is 4 and $l$ is 3, $j$ will be 5/2 and 7/2. The area ratio for the two spin-orbit peaks (4$f_{5/2}$:4$f_{7/2}$) will be 3:4 (corresponding to 6 electrons in the 4$f_{5/2}$ level and 8 electrons in the 4$f_{7/2}$ level). Spin-orbit splitting values $\Delta$ (eV) are tabulated. These values are important when fitting spectra with large chemical shifts, as they are elemental specific and do not change with the chemical state. For instance, in the case of U-4$f$ lines, $\Delta$ = 10.89 eV [56].

### *Final state effects*

By “final state” in photoemission experiments, a state of an atom with a positive hole and lacking electron is meant. It can be distinctly different from the initial state, and inferring ground-state properties from the final-state spectra becomes a non-trivial problem. This problem does not arise only for regular band states, for which the hole is filled “immediately” after the photoexcitation event, so that the initial and final states are equivalent.

This however does not apply to core levels. A core-level hole cannot be refilled on the timescale of photoexcitation event ($\approx 10^{-15}$ s) and the positive core hole attracts the photoelectron before it exits the solid. This would reduce the kinetic energy of photoelectron by tens of eV. However, the system can react on such short timescale by a relaxation, screening the positive charge of the core hole. This gives more energy available for the outgoing photoelectron, and therefore measured binding energy of the electron is reduced. Typical relaxation shifts are of the order of 10-20 eV [57]

The screening of the core hole involves two contributions: intra-atomic and extra-atomic. The intra-atomic screening arises from the relaxation of the electrons, primarily the outer shell electrons, within the excited atom itself. In molecules or solids, the creation of the core hole also induces polarization in the neighboring atoms' electrons, albeit to a lesser degree (extra-atomic relaxation). The screening of the core hole is influenced by the electronic environment, resulting in varying relaxation shifts across different systems for a specific core level line. For instance, in metals, the screening facilitated by electron rearrangement is more effective compared to ionic solids due to the presence of valence electrons (conduction electrons) that can freely move within the material. Consequently, the relaxation shift is more pronounced in metals.

Another final state effects that should be taken into account when analyzing the XPS spectrum are: plasmon losses, shake-up and shake-off processes, and multiplet splitting. In the first three processes, the photoemission results in the creation of electronically excited final states.

There is a finite probability that an outgoing photoelectron excites an ion (an additional electron is elevated from an occupied energy level to a bound unoccupied state) and brings it to an energy state a few eV above the ground state. In that case, the kinetic energy of the emitted electron will be lower and “shake-up” satellite peak at a higher binding energy than the main line will be seen. The strength and shape of the

satellite features can aid in the assignment of chemical states [58]. It is commonly believed that the intensity of the satellite is damped in itinerant compounds compared to localized systems [59].

In a process similar to a shake-up, valence electrons can be completely removed and sent into an unbounded state. This process is known as "shake-off" and results in the atom having vacancies in both the core level and a valence zone. Shake-off does not produce distinct satellites in solids. Instead, shake-off features tend to appear in the region of broad inelastic background, and the exclusion of the electron creates broad shoulders of core-level peaks rather than separate peaks.

Plasmon loss satellites arise from the excitation of quantized plasma oscillations, which are collective oscillations of the density of the free electron gas with respect to the positively charged ion cores. These plasmon satellites are displaced to higher binding energy with respect to the "elastic" line.

If an atom contains unpaired electrons in the initial state, during photoemission multiplet splitting occurs (exchange splitting of certain levels [50]). An unpaired electron may interact through its spin momentum with the spin of the additional unpaired electron in the core level from which the photoelectron has left. Parallel or anti-parallel spins' alignment gives final states with an energy difference of 1-2 eV.

A special case are lanthanides. The open 4*f* shell is located in energies of valence band, but the 4*f* electrons are typically localized in ionic states. Hence photoemission leads to a 4*f* hole (formation of the $4f^{n-1}$ state). The dynamics of the process leads to a certain population of higher levels of the $4f^{n-1}$ multiplet, which is then imprinted in valence-band spectra.

The most enigmatic is the situation of the 5*f* states in actinides. Their semi-localized nature makes a blind application of both localized and delocalized models misleading. The situation of strongly correlated states (energies of e-e correlations and band width are approximately equal) is notoriously difficult to describe and one often talks about dual nature of *f*-states [60,61]. The spectra can be theoretically described by advance Dynamical Mean Field Theory (DMFT), which captures both the atomic multiplets and bond formation effects, but the merit depends on particular computation framework (type of solver), and results are still matter of dispute.

### *Chemical shifts*

For the determination of chemical interactions and bonding in the sample, so-called chemical shifts are quite useful. Chemical shift is the energy difference in

binding energies of a particular core level due to different chemical forms of atoms. These shifts contain contributions from both initial state and final state effects (namely charge relaxation). When the later contribution is important, satellites are indistinguishable from the main line, and analysis of peak shifts is getting tricky. Although in many cases the effect of the modified physical and chemical local environment on the initial electron state is considered to be dominant. Only then BE shifts indeed reflect the chemistry in species. A few main mechanisms for BE shifts connected to the initial state will be described.

The first mechanism involves charge transfer to or from the core ionized atom. This term is considered as the dominant one. Fig. 1.12 depicts the simplified electronic structure of lithium (Li) metal and lithium oxide. In metal, 2*s* electrons form a band and their wave function is only partly at the site of a Li atom. In oxide, the 2*s* electron from metal is fully donated to an oxygen atom. Therefore, 1*s* electrons feel a weaker Coulomb repulsion than in Li metal. Consequently, the energy of the Li-1*s* states in the ground state sinks and the binding energy of the Li-1*s* level is higher in oxide compared to metal, giving a chemical shift.

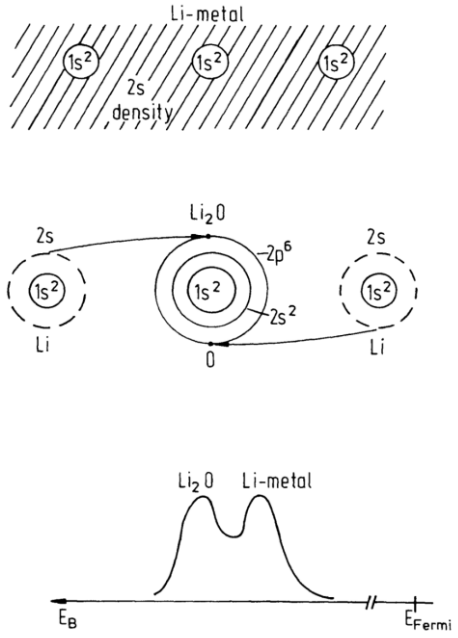


Fig. 1.12 Schematic drawing of the electron configuration of Li metal and $Li_2O$, and corresponding Li-1*s* PES spectrum. In Li metal the binding energy of the 1*s* level is lower than in $Li_2O$ due to 2*s* conduction electrons [50].

If talking about the quantitative description of the effect, a simple model can be adopted. Consider the removal of an entire electron from the outermost valence shell,

denoted $n_l$. The position of a core electron can be taken as at the nucleus since the size of the core orbital is much smaller compared to valence shell orbitals. Thus, the electrostatic potential which a core electron sees due to an electron in the valence orbital, $\varphi_{nl}$, is

$$V_{nl} = -\int \varphi_{nl}^{*}\left(\frac{1}{r}\right)\varphi_{nl}\mathrm{d}v = -\left\langle\frac{1}{r}\right\rangle_{nl} \approx -\frac{1}{\langle r\rangle_{nl}} \qquad (1.10)$$

where atomic units are used (atomic units are: 1 Hartree = 27.21 eV, 1 bohr = 0.53 Å, the electron charge is 1), small core-valence exchange integrals are neglected, and the small spatial extent of the core orbital is also neglected [62]. Removing an electron from the valence shell $n_l$ increases the potential and leads to a shift of the core-level BE for $\Delta BE = - V_{nl} > 0$.

Bagus et al. [63] have shown that this model is a reasonable approximation for shifts in alkaline-earth atoms. These equations can be generalized for the case of polar chemical bonds with partial removal of an electron.

The second mechanism involves the electric field caused by the effective charges of the surrounding atoms. These charges are normally viewed as point charges. The reasoning for BE shifts is similar to the previous case. In general, these shifts will be in the opposite direction to the shifts due to charge transfer.

The third mechanism relates to the bonding charge density of the valence levels of a molecule or the conduction bands of a solid. In this case, a large overlap of the valence orbitals on neighboring atoms, which was small and neglected in the previous mechanism, is taken into account. Chemical bonds are usually connected to this overlap. It leads to a build-up of electronic charge between atoms and an electrostatic potential at the nucleus of the core ionized atom, consequently. The value of this contribution depends strongly on the number of neighbors of the core-ionized atom.

An additional mechanism is the hybridization of valence levels. Hybridization is responsible for the promotion of deeper valence levels to higher levels. The resulting hybrid orbitals are directed toward and can form better bonds with neighbors. Hybridization involves promotion to a more spatially diffused orbital, and thus it leads to higher BEs for the hybridized atom.

The measured shifts of peak positions often represent the sum of different contributions.

### *Quantification*

One of standard application of photoelectron spectroscopy is a quantitative elemental analysis. It is possible to determine the atomic percentage of the elements present in the sample if the photon flux remains constant during the measurement. It is done by dividing the peak area by the relative sensitivity factors (RSF) [64]:

$$[i]\% = \frac{A_i}{s_i \sum_n \frac{A_n}{s_n}} \cdot 100\% \tag{1.11}$$

where $A_i$ – area below peak after background subtraction, $s_i$ – relative sensitivity factor for a particular element and orbital. The RSFs include the photoelectron cross-section, the attenuation length (unlike in IMFP, in the attenuation length the elastic scattering during the photoemission process is taken into account, and thus it is shorter than IMFP by 10-20 %), and the transmission function of the analyzer. Typically, the X-ray source is mounted at the magic angle $\delta = 54.7°$ (the angle between source and analyzer). At this angle, the photoelectron cross section does not depend on the angular term $\theta$ (Fig. 1.11 (a)).

It should be noted that the transmission function varies with selected apertures, lens modes, spot size and $\delta$ angle. In addition, IMFP is dependent on the material of the sample, data applicable to the sample should be included [65]. In the ideal case, the RSFs should be derived empirically for every spectrometer and material inspected. However, there are some tabulated values that can be used. This gives a reasonable quality of the quantitative analysis.

Another source of uncertainty in quantification results is the estimation of the inelastic background. All characteristic photoemission features appear superimposed with a featureless background, coming from inelastically scattered electrons and secondary electrons excited in “cascade” processes.

The removal of background requires a complete understanding of the underlying processes. The background must be distinguished from any peaks, which may be broad, asymmetric, or small due to specific elastic processes (satellite peaks or Auger electron peaks). The choice of type of the background (linear, Shirley and Tougaard are the most common) depends on the system analyzed and the sort of information wanted (peak fitting or quantification of the atomic percentage).

The Shirley method is a commonly used technique for subtracting non-linear background signals. It assumes that the background comes from the inelastic scattering

of electrons with higher kinetic energy and the background at kinetic energy $E$ is thus proportional to the photoelectron intensity of the given peak over kinetic energies higher than $E$. To accurately subtract the background, it is crucial to carefully select the beginning and end points of the particular peak. One has to assess if there is e.g. another peak overlapping. Otherwise, the process of removing the background may unintentionally remove important peak signals. Originally the Shirley method was proposed for the valence band spectra with small difference in intensities at beginning and end points and flat signals beyond the analyzed region. However, it works fine for quantifying core levels, as well.

Shirley background is achieved by calculating the Eq. 1.12 each point of the energy window. In principle, it is given as a weighted sum of the intensities $I_1$ and $I_2$ on the chosen edges of the peak (Fig. 1.13). The difficulty is that peak areas, needed to calculate the background, depend on that background. Hence iteration with the initial estimation of the values is necessary to calculate the background [66].

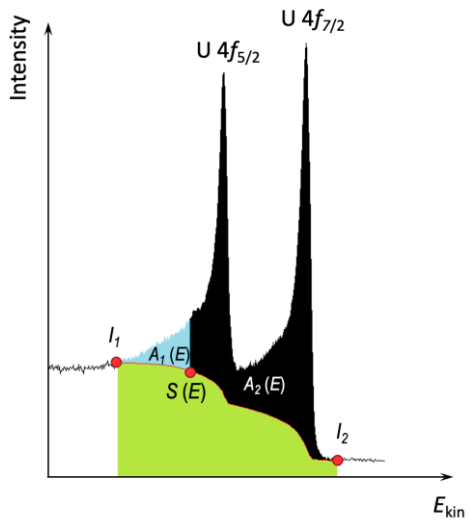


Fig. 1.13 Example of background calculation by Shirley method for U-4*f* lines.

$$S(E) = I_2 + (I_1 - I_2)\frac{A_2(E)}{A_1(E) + A_2(E)} \tag{1.12}$$

Throughout our work, the Shirley type of background was mainly applied. Linear type of background was used only in the case of weak signal with a slope in intensity outside of the peak region.

### *Basic structure of core-level spectra of U-based compounds*

The core-level spectra of strongly correlated materials often possess complex peak structures due to various screening mechanisms in the final state of the photoionization process. In addition, spectra of uranium-based compounds show a variety of satellite structures, the origin of those is still unclear due to the complexity of the initial and final states and their interplay [59,67]. One should not forget about the multiplet effect as well, which originates from the different configurations of *f*-electrons within the *f*-shell. For example, different types of core-level holes giving an unresolved multiplet of states interacting with the multiplet of localized 5*f* states may yield a rich manifold of states, which are nor resolved as individual lines but contribute to different width and shape of $4f_{5/2}$ and $4f_{7/2}$ core-level lines.

Fujimori et al. [68] performed systematic studies of U-based compounds with different degrees of *f*-electron localization. For a better understanding of the structure of the core-level spectra, two typical examples from opposite sides of the localization range (localized and itinerant compound) will be compared, namely, itinerant $UB_2$ and the localized $UPd_3$. Fig. 1.14 (a) displays their U-$4f_{7/2}$ lines which have very different spectral profiles. This is the indication of the different natures of U-5*f* states in these compounds. $UB_2$ has a relatively simple spectral line shape with a single peak at $E_B$ = 377 eV. Whereas the main line of $UPd_3$ has a rather asymmetric shape and is located at around $E_B$ = 379 eV. In addition, a satellite is present on the high-binding-energy side as well as a shoulder structure at around $E_B$ = 377 eV.

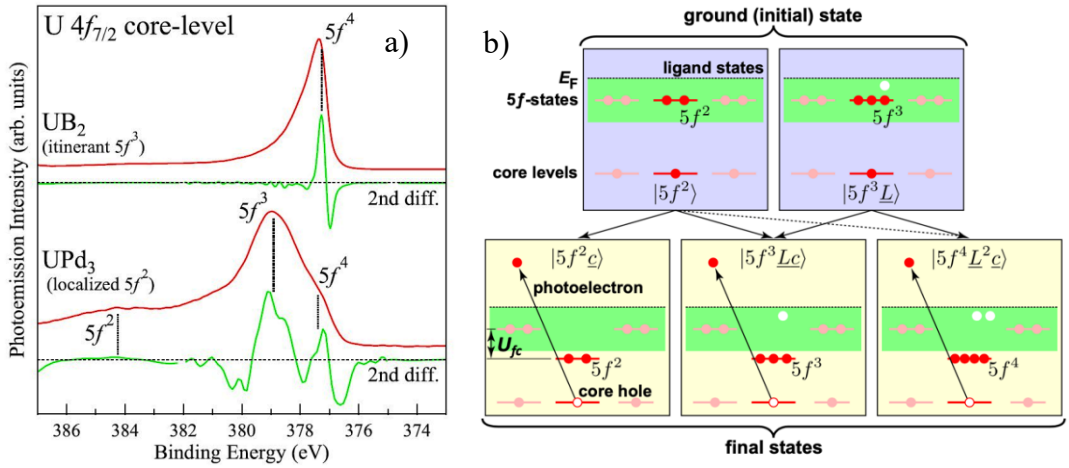


Fig. 1.14 U-$4f_{7/2}$ spectra of typical uranium compounds (a) and a simplified schematic of the photoemission process based on the single-impurity Anderson model (b). The electron configurations in their ground states (U-$5f^3$ for $UB_2$ and U-$5f^2$ for $UPd_3$)

suggest that the main lines of $UB_2$ and $UPd_3$ correspond to the dominant contributions from the U-5$f^4$ and U-5$f^3$ final states, respectively [68].

In uranium compounds, the local electronic structure of the U site in the ground state can be expressed as a linear combination of the $5f^2$ and $5f^3$ configurations. During the photoemission process, the 5*f* levels are lowered by the attractive potential of the core hole ($U_{fc}$, about 4 eV) in the final state. There are two variants then, core hole potential is either screened by the ligand electrons transferred to the lowered *f*-level or not. Considering that the screening and strength of hybridization depend on the ground state, the spectra should split into multiple peaks.

For $UB_2$ with itinerant U-5*f* electrons the band-structure calculation suggests the number of *f* electrons to be 2.82. Consequently, the local electronic configuration of the uranium in the ground state is very close to the U-5$f^3$ configuration. In the final state, the U-5*f* levels are lowered by $U_{fc}$, which are screened by the transfer of electrons from ligand states due to strong hybridization. As a result, the dominant final state in the core-level spectrum corresponds to U-5$f^4$. Thus, the peak observed at $E_B$ = 377 eV can be attributed to the U-5$f^4$ final state.

In contrast, the spectrum of $UPd_3$ exhibits a highly intricate structure. The U-4$f_{7/2}$ peak is composed of three peaks positioned at 384, 379, and 377 eV, respectively. Uranium 5*f* are localized, and the local U-5*f* configuration is U-5$f^2$. The dominant configuration in the final state should be U-5$f^3$, and the peak at 379 eV is attributed to it. Likewise, the peak around 377 eV is linked to the U-5$f^4$ configuration (as in $UB_2$). Furthermore, the peak at 384 eV is ascribed to the final state with the U-5$f^2$ configuration, given its stronger intensity in $UPd_3$ compared to $UB_2$. Strong hybridization between U-5*f* and ligand states results in a more mixed nature of the final-state configurations ($f^n$) in each peak, and these nominal assignments are approximate.

By comparing the core-level spectra of uranium-based compounds with these typical compounds, one can infer the valence state of uranium atoms, specifically the number of *f*-electrons present in the ground state.

As an example of chemical shifts and shake-up satellites uranium oxides were chosen. Energy, shape and strength of the satellites allow the determination of the oxidation state of uranium. The U-4*f* core level photoemission spectra for $UO_2$, $U_2O_5$, and $UO_3$ thin films are shown in Fig. 1.15 [69]. The U-4*f* XPS exhibits narrow and

symmetric peaks for all three oxides with maxima at approx. 380.2(1) and 390.9(1) eV for the 7/2 and 5/2 components, respectively (compare to 378 and 388 eV for uranium metal). The situation with chemical shifts in this system is more complex than that described previously as final states effects are expected in this case. These systems possess localized 5*f* electrons. In the simplest description, the 5*f* electrons have no possibility to screen 4*f* hole which results in higher final-state energy, kinetic energy of photoelectrons is hence lower, and the 4*f* peaks shift toward higher binding energy.

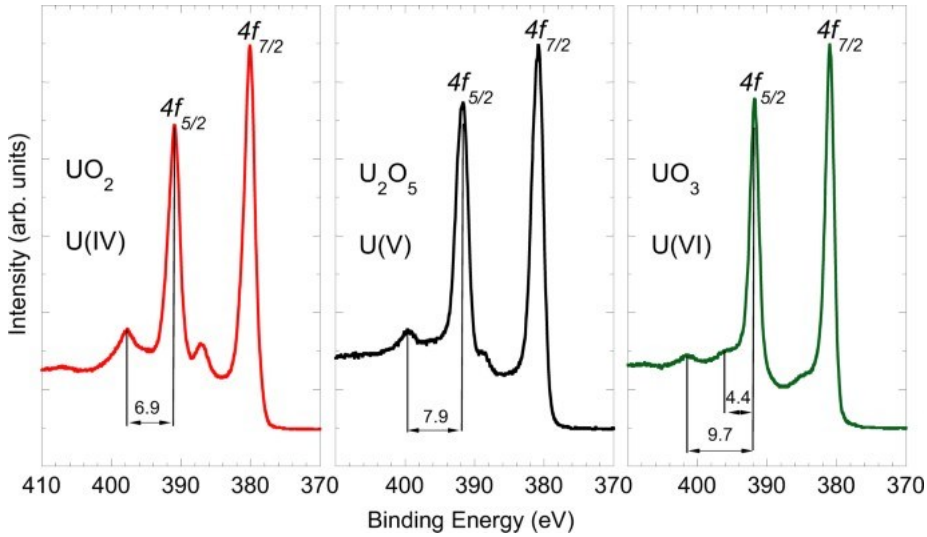


Fig. 1.15 Uranium 4*f* core-level XPS spectra recorded for U(IV) in $UO_2$ (left panel), U(V) in $U_2O_5$ (central panel), and U(VI) in $UO_3$ (right panel). The relative energy between the satellite peak and the $4f_{5/2}$ ($4f_{7/2}$) emission line is used as a marker for the oxidation state of the uranium atoms [69].

The difference of spectra for oxides lies in the satellites. For the $UO_2$ the distance between the satellite and the main line is 6.9(1) eV [70]. In the case of the $UO_3$ there exist two satellite peaks at 4.4(1) and 9.7(1) eV from U-$4f_{5/2}$. For the $4f_{7/2}$ peak the ~10 eV satellite is hidden behind the U-$4f_{5/2}$ peak. In the spectrum of $U_2O_5$ a satellite peak located at 7.9(1) eV higher binding energy for both spin-split peaks is present. This value is intermediate between those observed in $UO_2$ and $UO_3$. This satellite has an inter-atomic origin and has been attributed to charge transfer or shakeup processes [71]. The energy separation between satellite and main line mentioned above depends on the energy difference between the extended occupied O-2*p* states (which stay more or less constant for different oxidation states) and the localized unoccupied U-5*f* states (which are shifted to higher BE with the increase of oxidation

state). It is also known that the degree of covalency in the metal-ligand bond affects the energy of the satellites, which becomes smaller in less-ionic compounds [72].

Another example relevant for the studies described in this work is uranium hydride. Fig. 1.16 depicts detailed U-4*f* core-level spectra for pure U, $UH_2$, and $UH_3$. There is a clear difference between the spectra of metal and hydrides. For the hydrides, both $4f_{5/2}$ and $4f_{7/2}$ lines are asymmetric with significant broadening on the high binding energy side. The broadening is traditionally related to the formation of electron–hole pairs by *e*–*e* collisions around the Fermi level during the photoemission process. The peak asymmetry can, therefore, be taken as an indicator of the enhanced density of electronic states at the Fermi level and strong electron correlation effects [73].

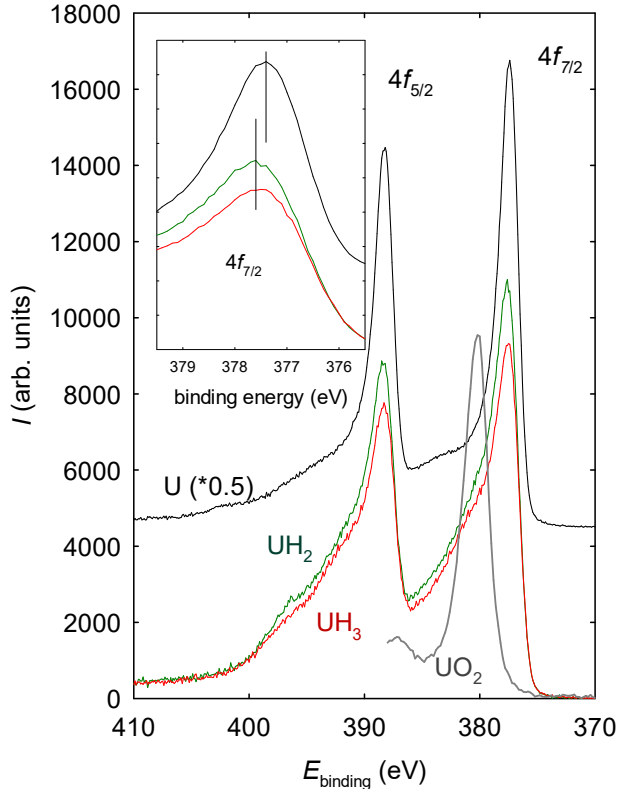


Fig. 1.16 U-4*f* core-level spectra of $UH_3$ (red), $UH_2$ (green), and U metal (black, rescaled to 50% and shifted up for clarity). The inset shows details of the $4f_{7/2}$ peak for all three cases, with vertical lines illustrating the energy shift for both hydrides. For comparison with an insulator, the main figure also includes the $4f_{7/2}$ peak of $UO_2$, located at the binding energy more than 2 eV higher than for U metal, $UH_2$ and $UH_3$ [5].

Another difference is a considerable intensity reduction of 4*f* peaks in the hydrides compared to the U metal. One of the reasons can lie in the almost twice lower density of the hydride [5] and thus the concentration of U in the XPS information depth. Moreover, spectral weight is redistributed to higher binding energies (energy loss side).

Interestingly, spectra of $UH_2$ and $UH_3$ are similar, hinting that the character of the electron subsystem and general bonding properties should be analogous. There is a small shift of the maxima (by 0.2 eV) toward higher binding energies, which can be explained by a transfer of 6*d* and 7*s* electrons from uranium to hydrogen atoms [28]. The shift is much smaller compared to $UO_2$ case. Moreover, 5*f* electrons are believed to have itinerant character, and thus keep their ability to screen the 4*f* hole.

One of the subjects of the current work is U-Mo system (incorporating H as well). XPS studies have been performed by our group before [33]. Interestingly, except for checking U-4*f* lines, additional information was obtained from the Mo-3*d* core level lines (Fig. 1.17). They form a doublet with an energy split $\Delta$ =3.15 eV. $3d_{5/2}$ line was chosen for the evaluation of energy shifts due to narrower shape and higher signal-to-noise ratio.

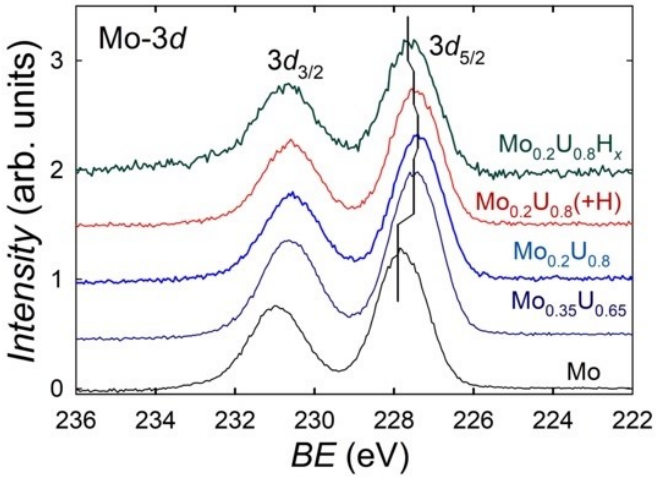


Fig. 1.17 Mo 3*d*-core level lines for varying U-Mo ratios (bottom). The top two spectra reflect the effect of H on $U_{0.8}Mo_{0.2}$ [33].

As a reference, pure Mo film sample was taken with the line position at 227.9 eV BE (228.0 eV is a commonly indicated value). The line shifts to lower binding energies with the increase of U concentration on the film (0.6 eV and 0.7 eV for 65 at.% and 80 at.% of U, respectively). Further decrease of Mo concentration does

not lead to any additional shift. The shift can be associated with bonding, assuming some electron transfer from U to Mo. In the hydrides the opposite variation of energies are detected which can be understood as the interaction of Mo with H, or the partial release of Mo from U bonding due to the strong U-H interaction. These data will be discussed later in terms of the effect of alloying on the Curie temperature in uranium hydrides (see Section 3.4.2).

#### 1.3.3.2. Ultraviolet photoelectron spectroscopy

Ultraviolet photoelectron spectroscopy (UPS) is used to study valence energy levels and chemical bonding. This method operates on the same principles as XPS; the only difference is the radiation used to induce the photoelectric effect: tens of eV for UPS compared to more than 1 keV used in XPS.

Besides synchrotron radiation, typical ionization sources are Ne I (16.6 eV), Ne II (26.8 eV), He I (21.2 eV), and He II (40.8 eV). These lines are usually produced by an ionizing gas discharge in a windowless differentially pumped lamps.

UPS has higher surface sensitivity than XPS. Emitted electrons possess much lower kinetic energies and IMFP, accordingly, than those detected in XPS. That gives an approximate information depth of 2-3 nm [74].

The energy of UV photons is not sufficient to excite electrons from the deep core levels, so UPS is particularly useful to study valence states in the solid. In XPS, the high (compared to the binding energy of the valence states) photon energy results in large electron kinetic energies and small photoionization cross-sections for the valence levels. Consequently, the count rate of detected electrons is low, and the energy resolution is poor, making it challenging to investigate valence levels with XPS. It is insensitive to the empty density of states providing a clear view of the occupied electronic orbital [75].

As mentioned above, PES spectra correspond to a large extent to the density of genuine band states (one-electron density of states). They are, however, affected by a lifetime broadening increasing with increasing distance to the Fermi level. Moreover, each type of states has different photoexcitation cross section, which depends on the photon energy. This helps to identify particular spectral features.

In the case of U, the cross-section for the 5*f*-states is negligible for the He I radiation. However, it increases in He II while the other types of states exhibit a

decreasing tendency (Fig. 1.18). Hence the valence-band spectral features emphasized in He II with respect to He I can be attributed to the 5*f* states (Fig. 1.19).

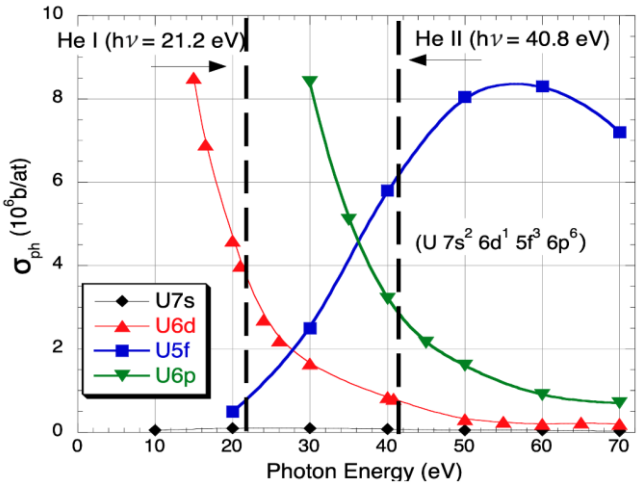


Fig. 1.18 Atomic photoionization cross section dependence on photon energy for U $7s^2 6d^1 5f^3 6p^6$ energy bands [76].

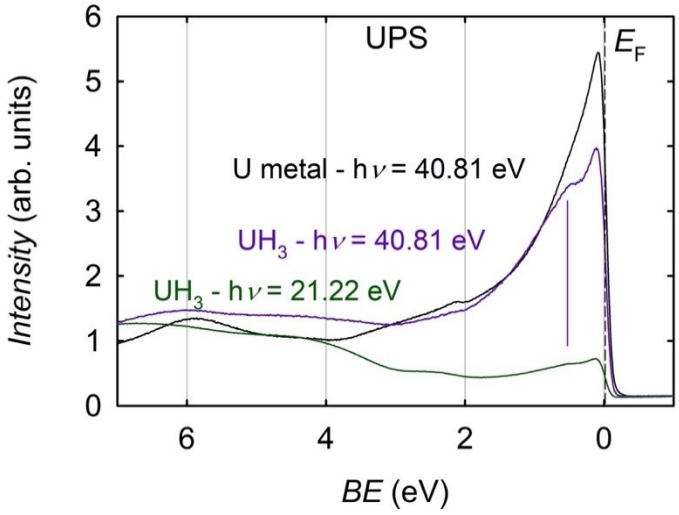


Fig. 1.19 He II UPS spectra of U metal (black) and $UH_3$ (violet) and He I spectrum of $UH_3$(green).

The intensity drops to zero rapidly at a binding energy of 0 eV, which corresponds to the Fermi energy level (border of occupied states). In a solid, the valence states contain the most weakly bound electrons as they possess the lowest energy levels. These electrons play a crucial role in determining the unique electronic and electrical properties of materials. Accordingly, the valence bands make a substantial contribution to the density of states (DOS) in the vicinity of the Fermi level, which is probed by UPS. $N(E) = 0$ at the Fermi level is a characteristic feature of

semiconductors and insulators and reflects the existence of a band gap. Conversely, metals exhibit a finite DOS that crosses the Fermi level, which leads to high conductivity and a large number of free charge carriers. By considering the spin and other effects, a diverse range of density of states can be observed, which gives rise to various phenomena.

Interesting insight has been provided by Pu compounds with variable valencies, as chalcogenides (PuSe and PuSb [77]). They are often described as having mixed $5f^5/5f^6$ ground state configuration with rather localized 5*f* states. This fact is supported by the presence of two multiplets in the UPS spectra, particularly, $5f^4$ (from $5f^5 \rightarrow 5f^4$ transition) at higher BE and better resolved $5f^5$ ($5f^6 \rightarrow 5f^5$ transition) multiplets. For the itinerant systems (as α-Pu) the shape of the spectrum looks different. There is a triangular peak with its maximum right at the Fermi level which is attributed to the 5*f* band. In the system with an intermediate localization (for instance, δ-Pu) the spectrum represents a superposition of the triangular band signal and the multiplet.

The rule of thumb when assessing valence-band spectra of U systems is to compare them with ab-initio calculations (DFT, e.g. GGA) and if agreement is found it is reasonable to conclude the 5*f* delocalization. If the 5*f* spectral density is separated from the Fermi level, it can indicate a tendency to localization, and such situation can be still captured by the DFT+*U* calculations. However, a more advanced DMFT, mentioned already above, is a more adequate way of description, providing the self-energy of the system of interacting electrons, in particular including on-site electronic excitations within an *f*-ion. This all relates to occupied part of electronic states. To probe the empty part, other technique is required.

#### 1.3.3.3. Bremsstrahlung Isochromat Spectroscopy (BIS)

PES can be performed in reverse mode. The technique is called Inverse Photoelectron Spectroscopy (IPES) and is based on bombarding a sample surface with electrons and detecting the Bremsstrahlung photons produced by decelerating electrons into the empty energy levels (above $E_F$). If only photons of one particular energy are detected (and electron kinetic energy is swept up), the technique is termed Bremsstrahlung Isochromat *S*pectroscopy (BIS) [50].

The electronic processes engaged in both spectroscopies are quite similar and become identical at $E_F$. Surface sensitivity and inelastic processes have the same

influence in the two types of spectra, allowing them to merge together at $E_F$ smoothly [78].

Baer and coworkers [78,79] first implemented BIS in the actinides research. Fig. 1.20 depicts the BIS of α-U in comparison with the calculations of Kutepov [80,81] in the improved GGA LDA scheme. From various measurements and investigations, it has long been considered that α-U has three 5*f* electrons and a strong delocalization in the 5*f* states [10,81,82], which can also be derived from the BIS spectrum.

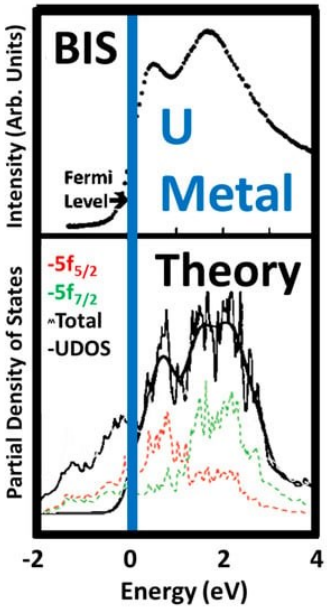


Fig. 1.20 Comparison of the BIS data of Baer et al. [78] with the Unoccupied density of states (UDOS) derived from the calculations by Kutepov [81]. The unsmoothed $5f_{5/2}$ and $5f_{7/2}$ calculated spectra are shown in red and green respectively. The UDOS (thick black line) was derived by applying extensive smoothing to the total DOS (thin black line). Figure adopted from [83].

Two peaks, at 0.5 and 2eV (due to large spin-orbit splitting [80,81]) with a minimum near 1eV are visible on BIS spectrum of α-U. The calculations support the experimental data and show the spin-orbit splitting of the 5*f* states on the scale of 1.5 - 2eV [84]. Whereas *j*-specific calculations display the admixture of the $5f_{5/2}$ and $5f_{7/2}$ states, consistent with strong delocalization. Similar to UPS, there is a sharp drop-off or step at the Fermi level in the BIS data due to the forbiddance of spectral transitions to states below the Fermi level.

### *1.3.4. X-ray diffraction methods*

Present studies mainly concentrated on describing the correlation between the electronic structure and physical properties (magnetic and transport) of chosen uranium-based systems. The methods described below are complementary but crucial for obtaining a full picture of the phase composition and crystal structure of the thin films prepared.

X-ray diffraction (XRD) is one of the most important non-destructive tools to analyze all kinds of matter. It is based on the constructive interference of monochromatic X-rays on the crystallographic planes of a sample. These X-rays are generated by a cathode ray tube, preferably filtered to produce monochromatic radiation, collimated to concentrate, and directed toward the sample.

Crystals consist of regular arrays of atoms. At the elastic scattering, the incident X-ray wave is scattered primarily by electrons at individual atoms, producing a secondary spherical wave. A regular array of scatterers produces a regular array of spherical waves. While destructive interference occurs in most directions and leads to wave cancellation, constructive interference occurs in certain specific directions, as determined by the Bragg's law: Fig. 1.21Here $d$ is the interplanar distance, $\theta$ is the incident angle, $n$ is the integer number of scatterers, and $\lambda$ is the wavelength of the beam. These specific directions appear as spots on the diffraction pattern called reflections. X-rays are used to produce the diffraction pattern because their wavelength $\lambda$ is typically the same order of magnitude (1–100 Å, $CuK_\alpha$ radiation = 1.5418 Å) as the spacing $d$ between planes in the crystal [85,86].

The positions and relative intensities of the peaks can be used for qualitative phase analysis. A more detailed analysis of peak intensities can lead to quantitative phase analysis. Unit cells can be derived from the peak positions. Powder diffraction data can be used to refine crystal structures using the Rietveld method. Peak profiles also contain valuable information about the size of crystallites, strain, and nanostructure. Non-idealities in peak intensities provide insights into the texture of the sample [87].

The basic instrument is a diffractometer. The diffractometer is generally composed of four axes: the $\omega$ axis (sample rotation axis), the $\varphi$ axis (in-plane rotation axis), the $\chi$ axis (tilting axis) and the $2\theta$ axis for scanning the detector.

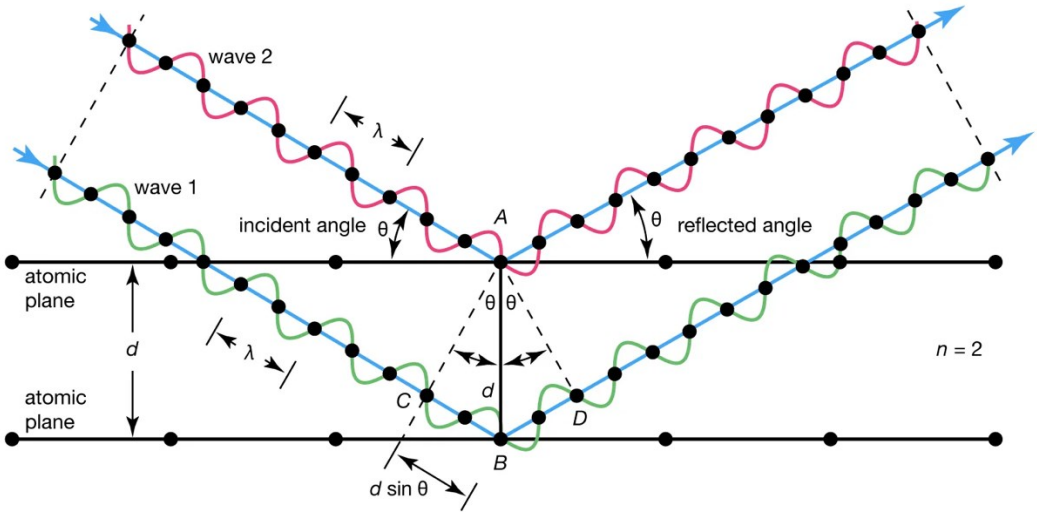


Fig. 1.21 Schematic representation of the electromagnetic radiation scattering with the condition of constructive interference [54].

The $\omega$ axis is often called the $\theta$ axis in conventional X-ray diffraction measurements of powder sample. In this type of measurement, the $\omega$ axis is controlled in conjunction with the $2\theta$ axis so that its rotation angle is always kept to half of that of the $2\theta$ axis. In an X-ray thin-film measurement, however, the sample rotation $\omega$ axis is generally controlled independently of the $2\theta$ axis [88].

Some precautions and constraint conditions must be considered when measuring a sample in a thin film form. In particular, only one set of specific lattice planes can be detected for a film with a strong preferred orientation. This is one of the reasons why measurements of thin films are more difficult compared with powder samples.

#### 1.3.4.1. Arrangements and geometries for X-ray measurements

In a conventional $2\theta/\theta$ measurement, only lattice planes that are parallel to the sample surface are measured. The angles of the incident and the diffracted beams against the sample surface plane are equal ($\theta$), and this geometry is known as "symmetrical-reflection measurement". For a strongly preferred-oriented thin film, especially an epitaxial thin film, the information obtained by a $2\theta/\theta$ measurement is insufficient. There is a need to measure lattice planes that are inclined to the sample surface. Moreover, during symmetrical reflection measurement, the angle $\theta$ is about several to tens of degree. As a result, the incident X-ray beam penetrates deeply into a sample to a maximum of tens of mm. However, the thickness of a thin film is

commonly hundreds of nm, and diffraction intensities from a thin film are generally very weak and often buried under the tail of the strong substrate diffraction peaks.

The asymmetrical-reflection measurement (Fig.1.22) can be used to measure diffraction peaks from a thin film. In this kind of measurement, the angle of the incident X-ray beam is fixed to a given small value (about several degrees or less), and only the detector is scanned to obtain high diffraction intensities from a sample itself and suppress signal from the substrate. Inclined lattice planes can be measured in this geometry [88]. One of the methods performed in an asymmetrical reflection geometry is Grazing Incidence X-ray Diffraction (GIXRD). In this method, the fixed angle $\alpha$ is generally chosen to be slightly above the critical angle for total reflection of the film material (after the critical angle, the penetration depth increases rapidly) [89,90].

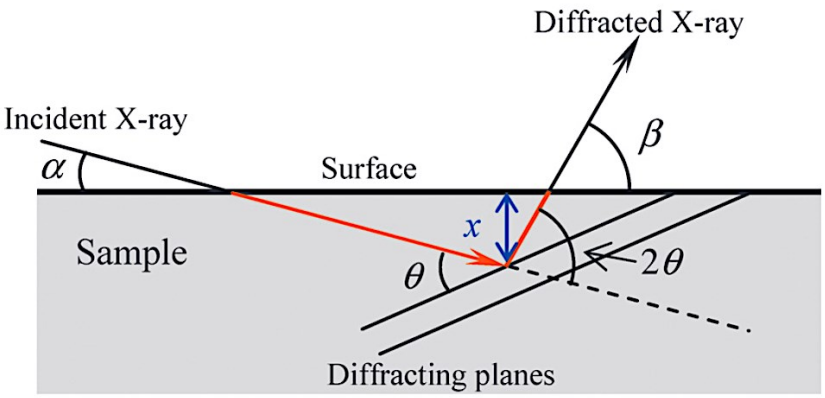


Fig.1.22 X-ray diffraction geometry for the asymmetrical reflection [91].

These two types of measurements are also called “out-of-plane measurements” because in both of them the normal direction of the lattice planes goes out of the sample surface. It is possible to directly measure lattice planes that are perpendicular to the sample surface. In this case, the measurement is called “in-plane measurement” [88].

#### 1.3.4.2. X-ray optical geometries

The Bragg–Brentano focusing optics have been widely used in X-ray powder diffractometry. It is used for the data collection of symmetrical reflections. This optics fully uses a divergent incident X-ray beam to obtain high diffraction intensities and has high resolution. Only a qualitative phase-identification analysis can be performed when measuring a thin film sample with focusing optics. The main issue is that different incident angles mean different probing depth. Therefore, for a quantitative

analysis the parallel incident X-rays at fixed angles are more suitable. The incident divergent X-ray beam is converted into a parallel beam by employing an optical element, such as a multilayer mirror. A parallel beam is used in an asymmetrical-reflection measurement of the thin-film structure and residual stress in a sample.

#### 1.3.4.3. Pole figures

A pole figure (PF) measurement is an XRD technique employed for observing textures in polycrystalline samples or the analysis of the orientation or domain configuration of epitaxial thin films [92]. It allows the analysis of textural information of samples averaged over a large area/volume. Traditional pole figure measurements are made by recording the intensity of a given Bragg reflection (fixed $2\theta$ angle) as a function of rotation and tilt of the sample.

The intensity of a given reflection is proportional to the number of (*hkl*) planes in the reflecting condition. Hence, the pole figure gives the probability of finding a given (*hkl*) plane normal as a function of the specimen orientation. In an in-plane pole figure, the incident beam, sample rotation, and detector angle are all moved, eliminating the necessity to tilt the sample. The in-plane pole figure also allows a greater range of texture to be recorded, as it contains the in-plane sample (sample surface) texture [93].

#### 1.3.4.4. Reciprocal space mapping (RSM)

The diffraction angle ($2\theta$) remains constant at the PF measurement. That means, in the reciprocal space diffracted intensity distribution is measured on the curved surface at a constant distance from the coordinate. On the other hand, in the case of reciprocal space map (RSM) measurements, the signal intensity distribution on a flat cross-section plane passing through the coordinate origin is observed (Fig. 1.23) [92].

The use of a fixed diffraction angle in PF measurements results in insensitivity to minor variations in diffraction angles which should be measured in elastically deformed epitaxial thin films constrained to substrates. In this case, RSM measurements are more effective. Conversely, PF measurements are more suitable for determining the orientation relationships between epitaxial thin films and substrates.

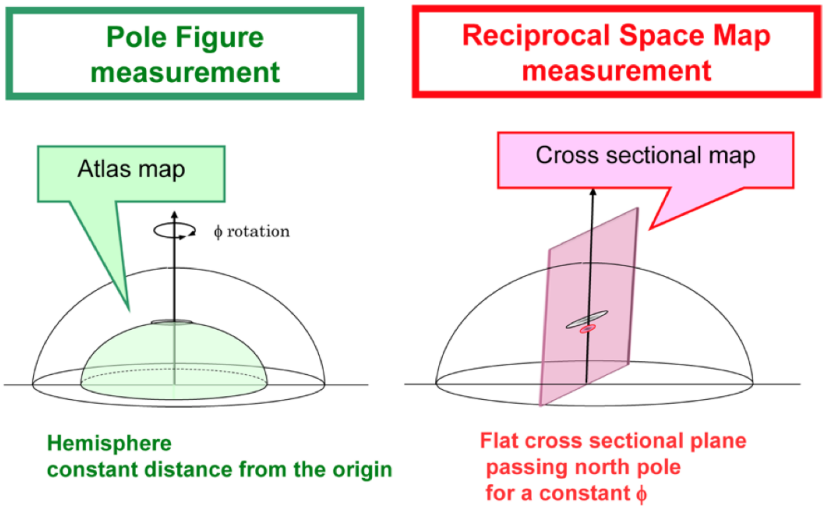


Fig. 1.23 Schematic illustration of pole figure and reciprocal space map measurements [92].

In situations where complex domains are present in the epitaxial thin films, a more detailed analysis involving a combination of measurements, such as PF measurements, wide-range RSM measurements, and in-plane RSM measurements, should be carried out.

#### 1.3.4.5. X-ray reflectivity (XRR)

X-ray reflectivity (XRR) is a standard technique for thin film characterization. Unlike previously described techniques, XRR does not deal with diffraction phenomenon. The XRR measurement method involves analyzing the X-ray reflection intensity curves from a grazing incident X-ray beam to extract important thin-film parameters such as thickness, density, and surface/interface roughness. It is possible to study single-crystalline, polycrystalline, and amorphous substances.

XRR analysis involves irradiating the flat surface of a sample with a grazing X-ray beam at specific angles of incidence. The X-rays are reflected by the sample atoms, and the total reflection angle occurs at or below a critical angle $\theta_c$, which varies with the electron density. The XRR analyzer measures the intensity of the reflected X-rays in such a direction, where the reflection angle of the X-rays is equal to the grazing incident angle of the original X-rays. For ideally flat samples the reflectivity decreases proportionally to $\theta^4$ as the angle of the reflected beam rises above the critical angle (Fresnel reflectivity), and the depth of penetration increases [94]. For rough

samples, the larger the roughness of a film, the faster the decay rate of X-ray reflectivity.

If for some reason only part of the X-ray beam is reflected, refracted wave penetrates the film and reflects on the substrate-film interface. The X-rays reflected from different surfaces (the interface of the substrate and the coating, and the free surface) interfere. This creates an interference-induced oscillation pattern (Kiessig fringes). Fig. 1.24 shows the summaries of the information which can be determined from the shape of a reflectivity pattern.

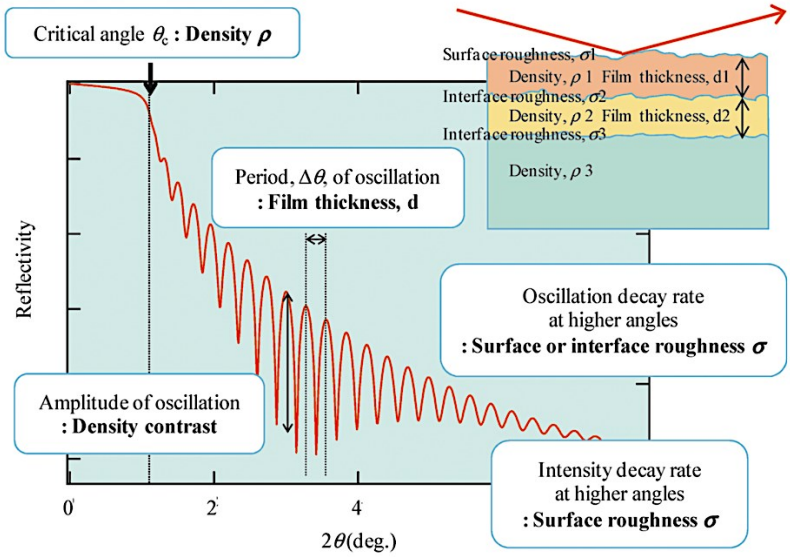


Fig. 1.24 Information provided by the X-ray reflectivity profile [95]. The reflectivity curve is a combination of the Fresnel reflectivity component, which follows a $1/\theta^4$ dependence, and an interference pattern, known as Kiessig fringes, resulting from scattering at various layers.

The thicknesses of the layers can be determined from the periodicity of the oscillation pattern (the thicker film, the shorter period of the oscillations). The roughness of the surface and the possible interface of the two materials can be deduced from the angular dependency of the amplitude of the oscillation pattern. The amplitude of the oscillation and the critical angle for total reflection provide information on the density of films. The larger the difference between the densities of the film and its substrate, the higher the amplitude of the oscillation. A similar picture happens with the critical angle, the higher the film density – the higher the critical angle [95].

# 2. Experimental details

## *2.1. Labstation: UHV system for surface science (JRC Karlsruhe)*

All the thin film samples were produced in the Labstation [43], a modular machine developed at JRC Karlsruhe. This system is composed of different interconnected chambers kept under dynamic ultra-high vacuum (UHV), reaching pressures of $10^{-9}$-$10^{-11}$ mbar. It is dedicated to the preparation of films, surface treatment (gas absorption and temperature-programmed desorption) and *in situ* studies of sample surfaces using X-ray and ultra-violet photoemission spectroscopy (XPS and UPS, respectively). The most important advantage of the setup is that the films are transferred under an ultra-high vacuum from preparation to an analysis chamber without exposure to the atmosphere. Due to the high surface reactivity of actinides, this condition is a key factor for obtaining spectroscopy data of high quality.

### *2.1.1. System description*

The Labstation (Fig. 2.1) consists of a linear transfer chamber (LTC) and several specific vacuum chambers. The Labstation base has been manufactured by SPECS company. The sputter source extensions have been developed in-house along with the sputter and data acquisition programs.

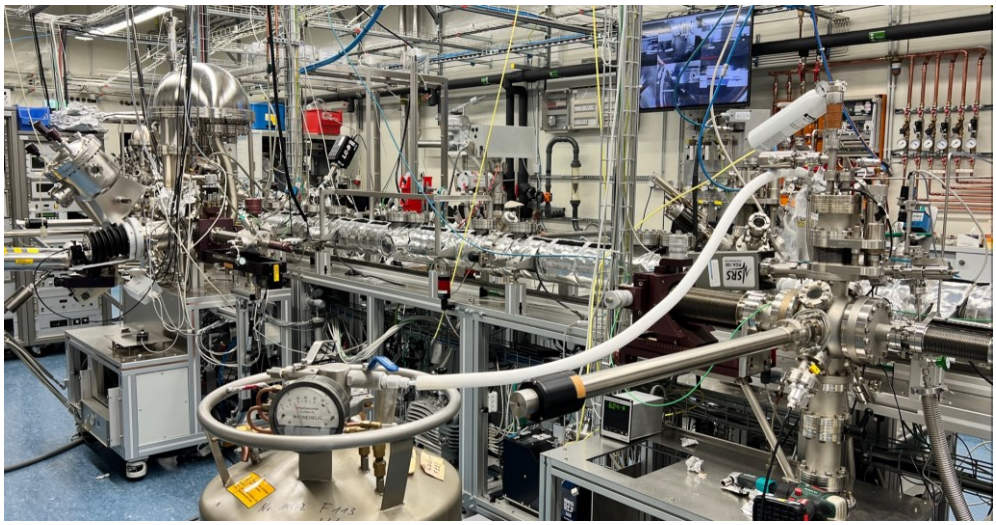

Fig. 2.1 Photograph of the Labstation system.

The scheme of the system is depicted in Fig. 2.2. Individual chambers can be isolated from the backbone transfer tunnel by a valve, allowing for easy gas filling or

servicing. That lets maintain the whole system under UHV and any baking can be restricted to individual chambers only. Each node has its own pumping unit (diffusion and turbo-pumps, ion sorption pumps, pressure gauges).

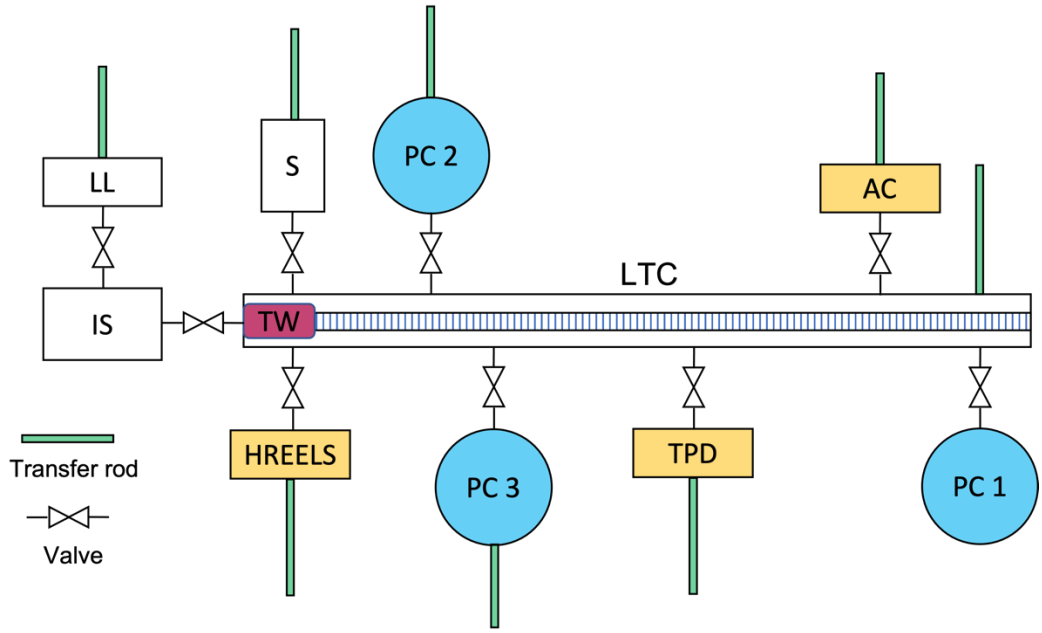


Fig. 2.2 Scheme of the Labstation: LL – load lock; IS – intermediate station; S – storage; TW – transfer wagon; HREELS – high-resolution electron energy loss spectroscopy chamber; LTC – linear transfer chamber; PC 1-3 – preparation chambers (1 – with ion gun and sputter source; 2 – with sputter source; 3 – with atomic source); TPD – temperature-programmed desorption chamber; AC – analysis chamber attached to photoelectron spectrometer.

### *2.1.2. Load lock*

In order to operate with the samples inside the system, substrates are fixed on stainless steel holders, the shape of which allows easy handling by manipulators (Fig. 2.3 (a)), by spot-welded tantalum (Ta) wires. Ta is used as a material with a high melting point, and thus poorly sputtered by gas ions, preventing contamination of the samples with the wire material. The substrate and holder are cleaned by acetone before and after mounting.

The loading of the sample holders into the system from an ambient atmosphere is done *via* a load lock chamber. It is specially designed to perform multiple sample handling (5 at a time) and minimize the time of reaching the final pressure $10^{-8}$-$10^{-9}$ mbar, thus limiting air contamination of the system. The load lock and

intermediate station (IS) are separated by valves from the LTC and each other. In other words, the intermediate station and central chamber are never exposed to significant vacuum drop. Cameras installed above each chamber give a live image of all the movements inside.

### *2.1.3. Linear transport chamber*

A transport wagon (Fig. 2.3 (b)) is used to pass samples from one chamber to another. The system comprises a wagon with five slots for samples, two magnets (one attached to a wagon and a second outside the vacuum on a rail connected to the motor controlled by a computer program), and rail for the wagon. The motor is controlled by a computer program (Fig. 2.4), it moves the wagon along the linear transport chamber of about 7 m long to *predefined* stop positions in front of each vacuum chamber. There are cameras on each position which monitor specific bar codes carved on a wagon. When a needed sample position code is detected, the wagon stops. Transit of the sample holder from/to the linear transfer chamber is accomplished by a transfer rod attached to each chamber.

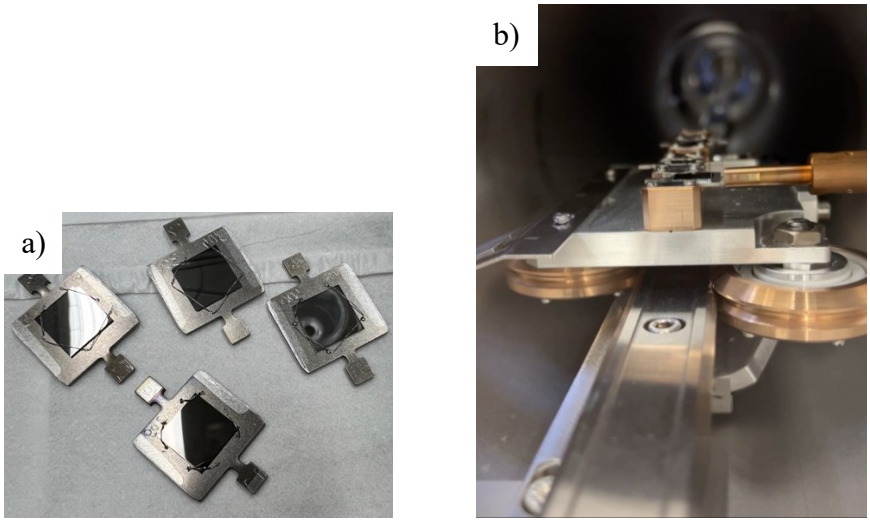


Fig. 2.3 Substrates mounted on sample holders (a) and transfer wagon with manipulator (b).

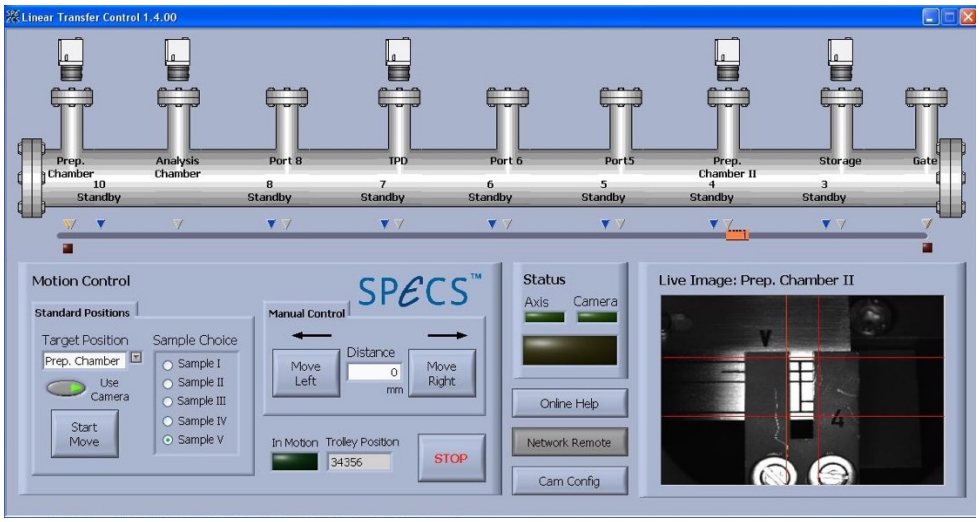


Fig. 2.4 The program Linear Transfer Control supplied by SPECS. The needed wagon position is recognized by a specific bar code (depicted on the bottom right corner).

### *2.1.4. Preparation chamber I*

All the side vacuum chambers are multifunctional, and their configuration can be adjusted to the demands of the experiment by adding various extensions. For our purpose chamber was equipped with an ion gun for sputter cleaning of the substrates and sample stage (Fig. 2.5).

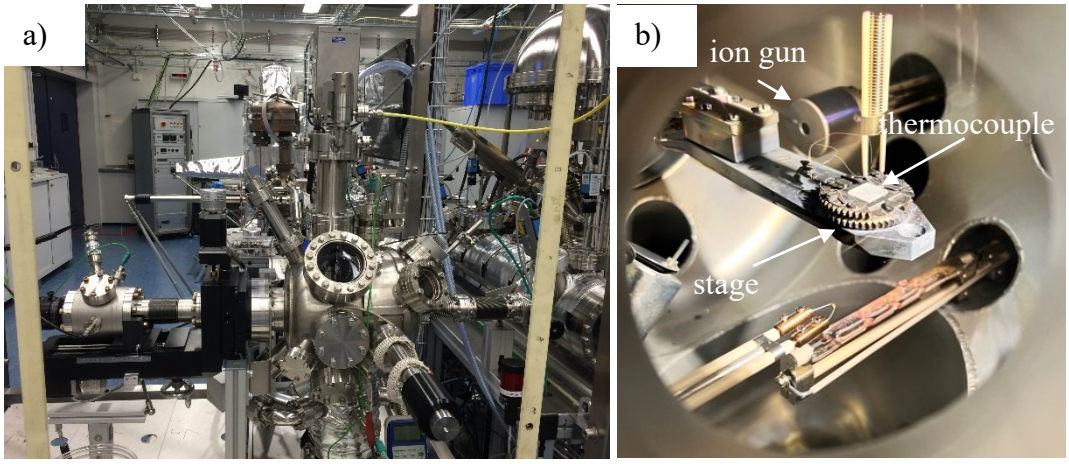


Fig. 2.5 Preparation chamber I: outside (a) and inside (b).

The manipulator of the stage allows to change sample position in three directions and rotate it around the horizontal axis. Motion is done by three step-motors and controlled remotely. Scanning of the surface by an ion beam is realized by moving the substrate in two directions. The stage includes electron beam heater (tungsten filament

below the sample) and leak cooler (cooling agents are air, water, liquid nitrogen, etc.). The range of temperatures is as wide as from 120 K up to 1000 K.

### *2.1.5. Preparation chamber II (sputter source)*

This chamber is equipped with a sputter source, residual gas analyzer and two sample stages: one with leak cooling and a second one with a PG-PBN heater. This type of heater consists of a pyrolytic graphite (PG) element track formed on a pyrolytic boron nitride substrate (PBN) [96]. These heaters are mainly used if fast temperature ramping is required in a reactive environment. The drawback of separate stages for cooling-heating is that stabilizing some intermediate low temperatures (for instance 170 K) is tricky and is executed by manual opening-closing the valve on the reservoir with liquid nitrogen.

For the reactive sputter deposition, Argon and Hydrogen gas are injected through needle valves. Additionally, the Ar pressure is kept stable by the flow-controller. As mentioned previously, flow control is not optimal for reactive gas, thus, we came up with a different method how to monitor $H_2$ partial pressure in the chamber during deposition.

Residual gas analyzer (RGA 100) from SRS company was used to control the purity of the residual atmosphere. The limits for partial pressure measurements are $1.33 \cdot 10^{-5}$ (maximum $10^{-4}$ mbar with switched off multiplier) to $6.7 \cdot 10^{-11}$ mbar [97]. Considering the fact that the average Ar pressure in the chamber during deposition was $6 \cdot 10^{-3}$ mbar, this mas-spectrometer could not be used for direct control of $H_2$ pressure stability. Preparation chamber II was connected via stainless steel tube to the preparation chamber III, and the gas amount was controlled by the needle valve. Similar RGA in preparation chamber III was monitoring the $H_2$ pressure continuously during deposition. The signal from the mass-spectrometer was proportional to the partial pressure of the gas and such method was quite sensitive to small pressure changes ($3 \cdot 10^{-8}$ mbar signal corresponded to the $H_2$ pressure of approx. $4.5 \cdot 10^{-4}$ mbar).

#### 2.1.5.1. Sputter source

Fig. 2.6 depicts a sputter source installed in the system for the deposition of all thin films mentioned in this work. A triode scheme with a thoriated W filament and DC power source was implemented. Plasma is constrained into a grounded cylinder

which covers targets and filament (not shown in the figure). For the deposition of films with substitution of U, two separate targets with independent power supplies were used. That gives better control over film composition and more freedom in the stoichiometries compared to deposition from an alloy target. The shape and size of targets and filament, as well as the placement of all the elements, were empirically optimized. Natural uranium (3N) rod, Mo (3N) and Zr (3N) wires were used as targets.

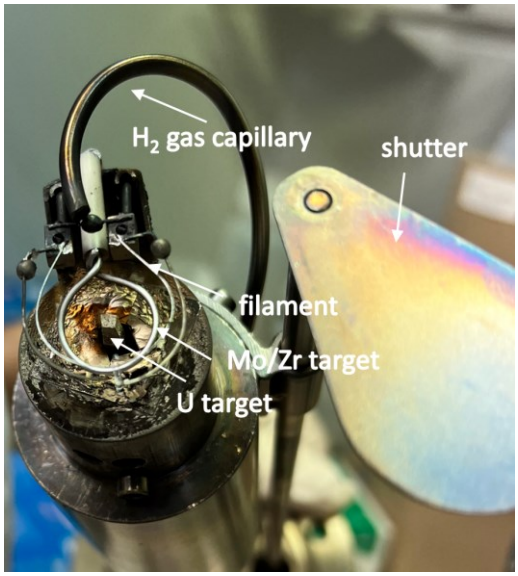


Fig. 2.6 Sputter source.

There is a shutter which is used for pre-sputter the target before exposing the substrate for film deposition. The idea is to clean the target from surface oxidation and to obtain stable processing conditions before exposing the substrate. However, the use of a shutter influences to some extent the process conditions, and therefore there is a new stabilization period after opening the shutter. During this period, the composition of the deposited film may vary significantly. In the present system, the shutter is placed immediately at the cylinder closer to the substrate which reduces (but does not eliminate completely) the effect of a closed shutter on the sputtering parameters [98].

Sputtering parameters were controlled through an in-house developed software. There are two parameters (Filament voltage and Working (target) voltage that are responsible for plasma ignition and maintaining. The sample composition is mainly controlled by target voltages. There is non-linear dependence between target voltages/currents and stoichiometries of obtained films. However, it is possible to determine sputter parameters for obtaining the desired composition, and these conditions are well reproducible from deposition to deposition. The program

automatically keeps the assigned target current by tuning filament and working voltages during deposition, which assures the homogeneous composition of thick films. The approximate thickness of the films was calculated from the time of deposition and a typical deposition rate of 1 Å/sec (deduced from previous experiments [99]).

For the preparation of hydride films, a hydrogen bottle with $H_2$ gas (5N purity) is connected to the chamber in such a way that the gas is supplied directly to the area where the plasma is formed. For the deposition of hydrides, sputter parameters had to be slightly adjusted. There is no such a significant target poisoning as in the case of $O_2$ or $N_2$ due to lower reactivity of $H_2$. In addition, U-H is sensitive to heating, our studies with thin hydride films of a few atomic layers have shown that hydrogen starts to desorb at 353 K and is fully desorbed at 413 K. The temperature of targets during sputtering is within this range or higher.

#### 2.1.5.2. $H_2$: gas purity

Even the best commercially available (5N) purity of the $H_2$ gas is not sufficient to prepare clean hydride films. By tuning sputter parameters (Ar pressure, filament heating, and acceleration voltages) we were able to reduce the O content from 50% to 15% of $UO_2$ in the best case. Only after adding gas filtering (Fig. 2.7) to the line we obtained pure films with less than 3% $UO_2$. Both Oxisorb (gas filter) and liquid nitrogen trap work similarly well.

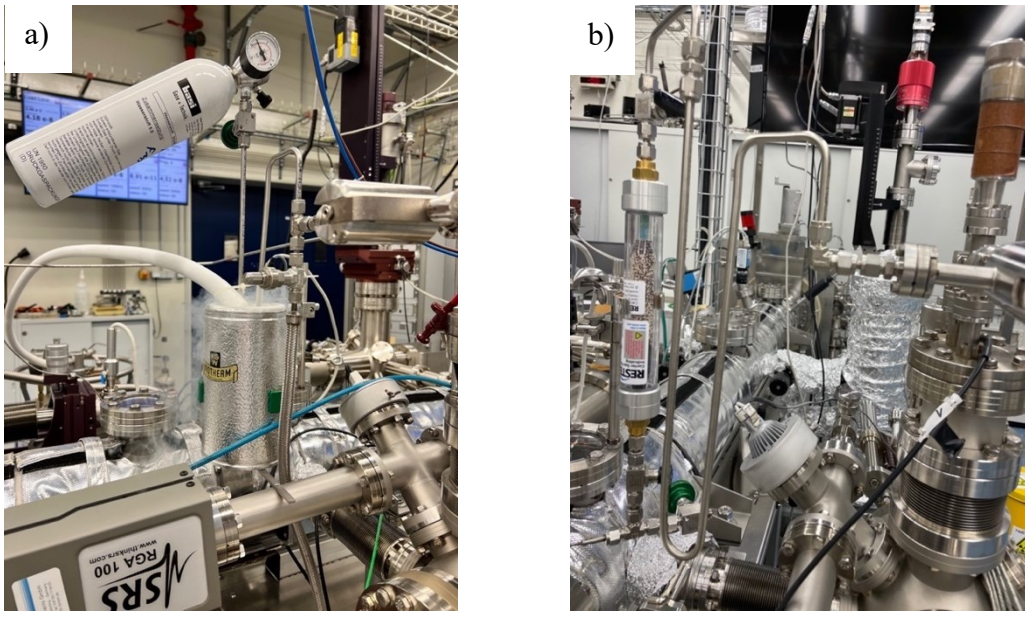


Fig. 2.7 Purification of $H_2$ gas: (a) liquid nitrogen trap, (b) Oxisorb.

The trap is slightly more complicated in operation as the U-tube must be kept in liquid nitrogen all the time during experiments, otherwise, all the contaminants which condensed on the cold tube walls will enter plasma and eventually contaminate the film.

### *2.1.6. Analysis chamber*

The Analysis chamber (Fig. 2.8) is the crucial component for the *in-situ* spectroscopic study. It is the ultra-high vacuum chamber with base pressure in the range $10^{-10}$-$10^{-11}$ mbar. The sample holder is the same as in preparation chamber I. It can be heated or cooled, tilted, and moved in three directions. An additional clamp is attached to prevent the sample from sliding when tilted. Ar and He gas lines are connected to the chamber through leak valves. The SPECS system is equipped with a monochromatized X-ray source (XRC-1000 MF, Al-Kα radiation, 1486.6 eV photon energy), $e^-$-beam heater with thermocouple sensing temperature directly from the steel sample holder plate, and an electron energy analyzer SPECS PHOIBOS 150 MCD-9. The combined energy resolution for the XPS is 0.4-0.5 eV for the typically used configurations of entrance slits and pass energy. For obtaining fine details around the Fermi level one can use an UV source for the UPS with HeII ($h\nu = 40.81$ eV) and HeI ($h\nu = 21.22$ eV) radiation. The energy resolution in the UPS mode is about 50 meV.

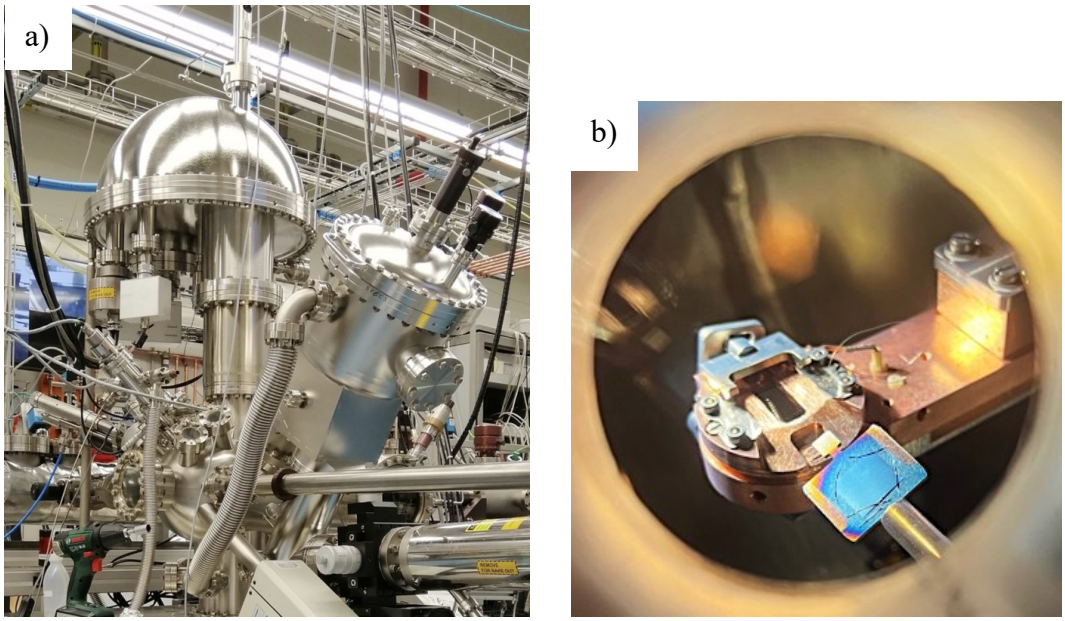


Fig. 2.8 Analysis chamber with hemispherical energy analyzer (a) and sample holder (b).

A scanning Ion Gun can be attached to the chamber for cleaning the surface directly in the analysis chamber or for depth profiling. An electron Flooding Gun FG-500 (low electron energies) in the chamber is used for the prevention of charging of non-conducting samples. A high-energy electron gun can bombard the sample for BIS measurements.

In-home developed software is used for collecting spectra. Once the measurement conditions (energy window, pass energy, slit size, scan time, etc.) are introduced, a series of measurements can be performed automatically after switching on the X-ray source. The adjustment of the sample position can be done to optimize the intensity of the signal.

### *2.2. Sample preparation*

A few different types of substrates were used for film deposition, namely polished amorphous $SiO_2$ (fused silica), MgO (100) single crystals, Si wafers (001), single-crystalline $CaF_2$ (100) (same crystal structure as $UH_2$ with the lattice mismatch below 3 %), and gold (Au) foil. Conducting substrates (Si and Au) were mainly used for short depositions for the purpose of photoelectron spectroscopic studies. The average size was 10×10 mm.

Prior to thin film deposition, $SiO_2$, $CaF_2$ and MgO substrates were heated to 673 K for 20 min for degassing. Si and Au substrates were sputter cleaned in the PC1 for 30 min while heated to 473 K to eliminate the surface oxide layer and other possible contaminants.

One of the important deposition parameters is the substrate temperature. Throughout the study we experimented with substrate cooled by $LN_2$ to various temperatures down to 77 K. For the deposition at room temperature, we cooled the stage by a flow of air. Without such cooling, the substrate temperature was elevated to ≈ 340 K by the heat coming from the sputter source.

For the XPS and UPS analysis, films were deposited for a short period of time about 600 s. For saving experimental time and material resources, we deposited films above the previous one. Mentioned deposition time was sufficient for total coverage of lower layers and prevention of collecting signal from them (that was checked the absence of lines from the substrate on the spectra). Films obtained for *ex-situ* experiments were deposited for 3600 s, which provides a sufficient amount of material

for all measurements needed. In the case of hydrides produced without cooling, shorter deposition times up to 1000 s were used to prevent excessive surface heating and hydrogen escape. The deposition times < 1000 s were chosen experimentally by monitoring XPS spectra of the films.

Some of the samples had a capping and/or buffer layer made of Mo or Zr depending on the installed second target. In the case of Si substrate buffer was used to prevent the formation of $USi_3$ compound [100]. Samples for the resistivity study in their majority were neither buffered nor capped, allowing them to oxidize and to form a non-conducting $UO_2$ layer on the top during an atmospheric exposure. Due to large compressive residual strains, preventing cracking of the $UO_2$ cap, such "coating" is much more efficient than in the case of bulk metallic actinide materials.

The U target voltage -690…-900 V was used typically. U target current was varying from 0.7 mA to 3.1 mA. For the deposition of alloys or hydrides with U substitutions, U target current was usually kept constant at 2 mA, and different stoichiometries were achieved by changing the potential on a second target (and its current accordingly). Details of sputtering parameters for the U-H samples are summarized in Attachment A.1, alongside buffer or capping layers.

Overview XPS spectra of each sample were used for the basic check of chemical composition and exclusion the presence of contaminants as O, N, or C (their concentration is less than 3 %).

However, these spectra cannot be used to determine the stoichiometry of the hydride. The H-1*s* states are part of the valence band, hydrogen cannot be quantified, and the H/U ratio cannot be deduced. However, the presence of H strongly affects the shape of the U-4*f* core-level spectra (Fig. 2.9). Starting from pure uranium, the spectra change continuously when increasing the partial pressure of $H_2$ in the sputter gas. The formation of homogeneous hydride can be identified as the situation, from which the spectra no longer change upon increase of the $H_2$ pressure. This happens typically around 5% $H_2$ in Ar. We found that changes of U spectra are practically completed for $H_2$ pressure $1 \cdot 10^{-4}$ mbar (total pressure $6.8 \cdot 10^{-3}$ mbar). This should guarantee that at given conditions of $3.5 \cdot 10^{-4}$ mbar of $H_2$ gives us a safe margin for the hydride synthesis.

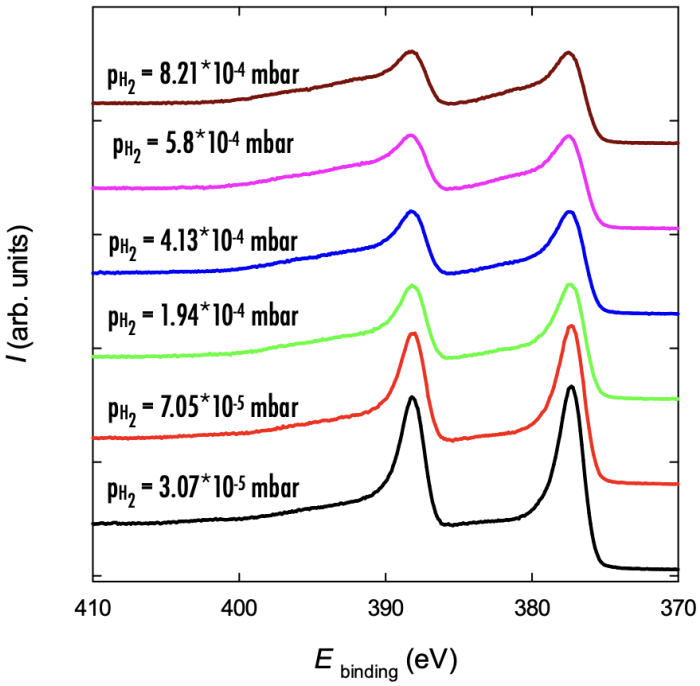


Fig. 2.9 Evolution of the U-4*f* lines with the changes of the $H_2$ partial pressure.

### *2.3. Structure analysis*

The structure of the films was analyzed using X-ray diffraction (XRD) methods on a Rigaku SmartLab diffractometer equipped with a 9 kW copper (Cu) rotating anode X-ray source, Panalytical X'Pert Pro MRD and Panalytical X'Pert Pro MPD diffractometers with Cu X-ray radiation (wavelength $\lambda = 0.15418$ nm). A few different geometries were used in the experiments. Parallel beam (PB) geometry was used for the XRR and GIXRD with the incidence angles of the primary beam, $\alpha_i$ = 0.3 - 10°. Parallel X-ray beam was produced by a parabolic multilayer mirror behind the line focus source. The obtained diffraction patterns were fitted using the whole powder pattern refinement method (Rietveld method). The computer program MStruct [101] was used for the fitting. To reveal the texture (preferred orientation) for some of the samples, we employed the RSM measurements on a Rigaku SmartLab diffractometer and pole figures. The RSM measurements were performed with a HyPix-3000 2D detector. The final RSM maps were obtained by combining $\Theta$-$2\Theta$ scans for various axial tilt angles $\chi$ of the sample. Pole figures were collected in the PB setup utilizing the in-plane arm that allows moving the detector to the arbitrary equatorial and axial position [102]. Symmetrical $\Theta$-$2\Theta$ scans were measured in the Bragg-Brentano geometry. XRR measurements provided information about the thickness of the films

which were used afterwards for the recalculation of the absolute resistivity values.

### *2.4. TEM*

A transmission electron microscopy (TEM) study was performed by means of the JEOL JEM-2200FS microscope operating at 200 kV. This method provides local information about the layers' thickness, grain size, orientation and crystal structure, and phase location. The TEM samples were prepared for the studies of cross-section in a scanning electron microscope (SEM) ZEISS Auriga Compact equipped with a focused ion beam (FIB) and easy-lift manipulator designed for In-Situ Lift-Out thin lamella preparation.

The process of lamella manufacturing consists of 6 individual steps [103]:

1. Deposition of a protective platinum (Pt) layer.
2. Prepare lamella via cross-sectioning.

Material is removed from both the front and back faces of the target area by $Ga^{2+}$ ion beam with 30kV acceleration voltage. The thickness of the cross-sectioned area is typically around 1-2 µm.

3. J-cut

A J-cut is made to disconnect the bottom and sides of the cross-section from the bulk of the sample (Fig. 2.10).

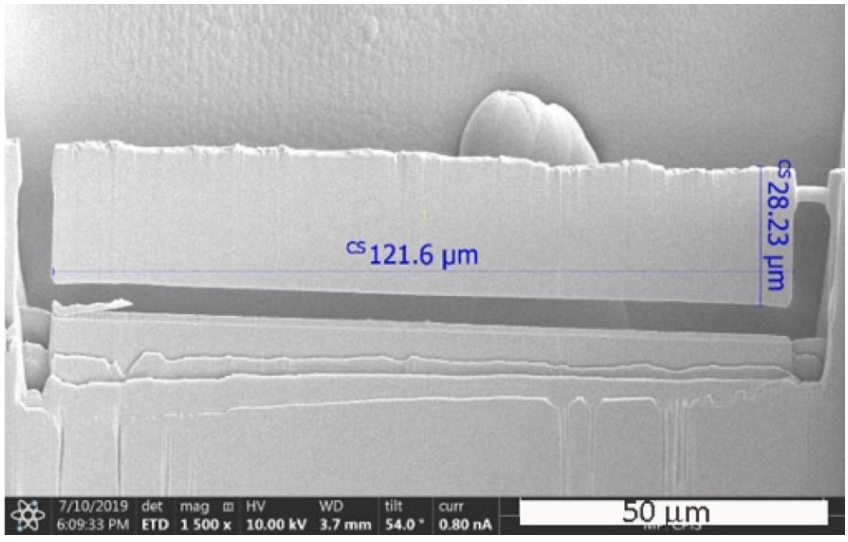


Fig. 2.10 SEM image of a lamella after J-cut.

4. Lift-Out

Once a sample is only attached to the bulk by a thin bridge, the cross-sectioned material is removed from the bulk *in-situ* with a micromanipulator setup (tiny needle,

using electrostatic attraction). After a section is removed, it is attached to the TEM grid for final thinning.

5. Lamella Thinning

The sample is thinned until the point of electron transparency. The approximate thickness of a section is determined using low electron accelerating voltages in SEM imaging.

6. Final Polishing

A final polishing of the sample is performed to minimize sample contamination by ion implantation and remove amorphous material that is generated by ion beam damage. At comparatively low energies (60 keV), the ion mean free path in metals is on the atomic length scale, and typical effective stopping distances are in the 10-nm range, which must be removed. Low accelerating voltage perpendicular milling was used (with a low current of 50-500 pA).

The thickness of the prepared lamella in chosen depending on the accelerating voltage of the TEM. A good rule is 0.8-1.5 nm per kV of accelerating voltage. In our case with 200 kV microscope samples were ranging from 160-300 nm thick.

### *2.5. Magnetization measurements*

Investigation of magnetic properties of hydride films was performed by VSM (vibrating sample magnetometer) option of PPMS 9 (physical property measurement system) and MPMS (magnetic property measurement system) by Quantum Design. Both systems allow to measure temperature $M(T)$ and field $M(H)$ magnetization dependences in the temperature range of 1.8-400 K. The highest magnetic fields are 7 T (for MPMS) and 9 T (for PPMS). The determination of the magnetic moment for both systems is based on the same physical principle – Faraday law. Drive motors oscillate the sample in the magnetic field created by one coil, the magnetic moment of the sample is proportional to the current induced in the pick-up coil.

MPMS provides the highest detection sensitivity of $10^{-8}$ emu within the whole temperature range due to the SQUID sensing device based on two Josephson junctions. However, long measurement time, lower field limit and relatively difficult sample preparation pushed us to use the VSM option for most of the performed magnetization measurements. VSM increases the sensitivity of PPMS. A low-background quartz

paddle was used as a sample holder. For the measurements, samples were cut into 4×4 mm pieces so they fit into the collecting coil.

### *2.6. Resistivity measurements*

Transport (electrical in particular) properties can give additional information about atomic and magnetic disorder in the films. Measurements were conducted on the PPMS 9 with the resistivity option. In order to cover 0.4-2 K temperature range, $^3$He refrigerator was used. PPMS has current limits ± 0.01−5000 μA and voltage limit 1−95 mV. For our experiments, 10 μA current was used, the measurement precision was around 2 mOhm (resistance of the films is the Ohm range). As standard 4-probe scheme cannot be used for thin films, Van der Pauw scheme [104] was applied.

There are a few requirements to the sample and experiment set-up for using this technique, among them flat homogeneous samples of uniform thickness with no isolating holes. Contacts must be located at the edges of the sample and the area of contact should be as small as possible, at least an order of magnitude smaller than the area of the entire sample. Deviations in the sample thickness bring uncertainty into the absolute values of the resistivity.

Films were glued to $^3$He pucks which allow to measure two channels simultaneously (Fig. 2.11 (a, b)). Aluminum (Al) with 3% of Si wires of 30 μm thickness were used to form the contacts to the film by an ultrasound wire bonder (grey wires on Fig. 2.11). Further electrical wiring was performed the way that current could be applied in two perpendicular[1] directions (blue and red lines). The total resistivity was recalculated afterwards by the formula [105]:

$$\rho = \frac{\pi d}{ln2} \cdot \frac{R_{BA,DC}+R_{CB,DA}}{2} \cdot f, \quad (2.1)$$

where $f$ is a factor which is a function only of the ratio $R_{BA,DC}/R_{CB,DA}$ (Fig. 2.12), $d$ – sample thickness, $R_{BA,DC}$ and $R_{CB,DA}$ – resistance measured in perpendicular directions.

[1] Current is applied along AB and BC contacts directions, which are not obligatory perpendicular.

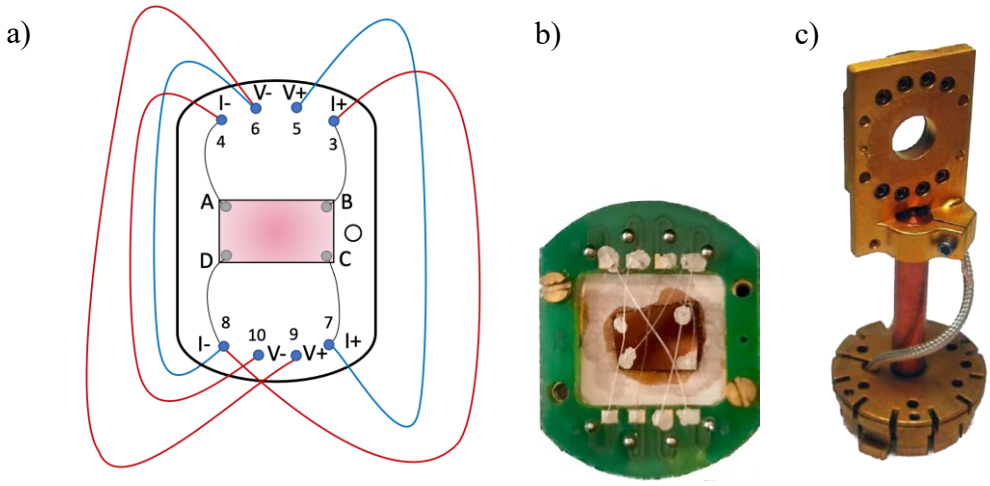


Fig. 2.11 (a) Electrical connections used for Van der Pauw resistivity measurements (blue – channel 1, red – channel 2); (b) mounted sample with wiring (c) vertical puck for MR measurements [106].

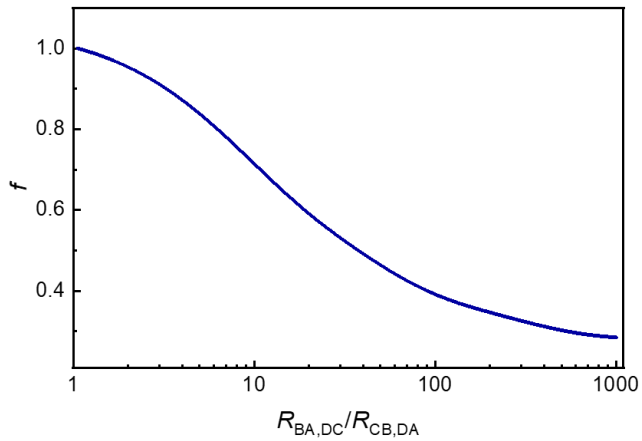


Fig. 2.12 Function *f* in the formula 2.1.

Magnetoresistance (MR) was measured in longitudinal configuration (field along the sample substrate surface) using vertical puck (Fig. 2.11 (c)).

## 3. Results and discussions

Originating from the investigation of potential candidates for low enriched uranium (LEU, <20% $^{235}U$) fuels [107], research on U-T (T – transition metal) films has concentrated into two main directions [38].

The first direction, spearheaded by the group from Bristol University, focuses on the synthesis of epitaxial films at elevated temperatures using magnetron sputtering. This method has enabled the production of films of materials that do not exist in single-crystal form as bulk samples, such as $U_3O_8$, $U_2N_3$, and alloys of U-Mo that form in a modified body-centered cubic (*bcc*) structure. The primary objective of these experiments was to observe structural variations, with low-temperature properties, such as superconductivity, remaining largely unexplored, partly due to the use of a Nb buffer layer. Additionally, there are concerns about the purity of these thin layers, as the vacuum chamber used for magnetron sputtering cannot be baked.

The second direction, pursued by our group at Charles University, focuses on polycrystalline films prepared at room or low temperatures, often on insulating substrates. This approach allows for the determination of transport properties, including superconductivity. Low-temperature deposition reduces the intermixing of substrate and film materials, and buffer layer is not needed in many cases. This effort has also incorporated the initiative to synthesize related hydrides, which cannot be prepared at elevated temperatures or in contaminated environments, as discussed in previous chapters of this work. The present thesis is a continuation of this endeavor.

This chapter presents the experimental findings of the current studies, highlighting both the confirmation of previous results and the discovery of new phenomena.

The first section focuses on the spectroscopic investigations of uranium alloys and hydrides, employing techniques such as XPS, UPS, and BIS. These studies clarify the impact of hydrogen atom incorporation and the addition of alloying elements on the electronic structure of the materials.

Following the spectroscopic analysis, the chapter delves into the structural characterization of U-T thin films alongside with their physical properties. Subsequent sections address the structure and properties of hydrides, with a particular emphasis on their transport and magnetic characteristics. This includes a detailed discussion on how various deposition parameters — such as substrate type, substrate temperature,

and target currents — affect the phase composition of the samples. These properties are analyzed in the context of the previously discussed electronic structure and phase composition, providing a comprehensive understanding of the material behavior.

## *3.1. Spectroscopic studies*

An essential question about uranium hydrides that needs to be resolved is whether the electron-electron correlations in these systems are strong or whether the hydrides behave as simple band magnets akin to transition metals. The interpretation of photoelectron spectra holds significant potential in clarifying this uncertainty.

### *3.1.1. Pure hydrides*

#### 3.1.1.1. Valence band XPS, UPS, and BIS on $UH_3$ and $UH_2$

Historically the first photoemission measurements on $UH_3$ (Fig. 3.1) were conducted on a cleaved monolithic sample prepared by hydrogenation at high temperature and high pressure. These measurements suggested that the 5*f* states were separated from the Fermi level, meaning a significant localization [108]. However, the data strongly resembled those of $UO_2$, especially when compared to a spectrum of an oxidized hydride obtained by us. The reactivity of hydride surfaces, especially for actinides, poses a significant challenge for their photoemission analysis. Subsequent attempts to synthesize films *in situ* led to much cleaner surfaces [99], revealing considerable 5*f* spectral emission near the Fermi level. This fact emphasizes the importance of clean surfaces for spectroscopic studies and the usefulness of the thin film approach.

Fig. 3.2 (a) displays VB XPS spectra of U metal and its hydrides. It can be concluded that, within the energy resolution of XPS (approximately 0.4 eV), the energy levels of the 5*f* states exhibit similarities between U metal and $UH_3$. Additionally, the spectrum of $UH_2$ closely resembles that of $UH_3$. The strong 6*d*-1*s* hybridization is forming a band between 4 and 8 eV below the Fermi energy in hydrides, however, the 5*f* states remain in the vicinity of $E_F$ as band states, similar to U metal. Nevertheless, there is a notable difference in intensity, which is reduced with increasing hydrogen concentration. Computational analyses suggest that the 5*f* occupancy remains largely consistent (approximately $n_{5f} \approx 2.7$ [12]); the decrease in

intensity can be attributed qualitatively to the lower density of U in the hydrides, resulting in fewer U ions within the information depth of XPS.

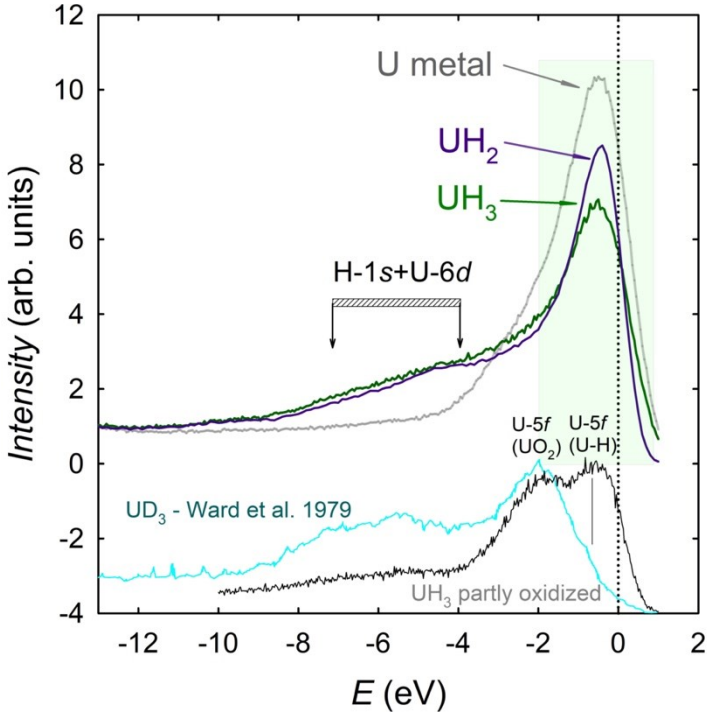


Fig. 3.1 Valence-band XPS spectra of elemental U (gray), $UH_2$ (violet), and $UH_3$ (dark green) films. At the bottom, historical spectra of $UD_3$ [108] and of partly oxidized $UH_3$ films provide insight into the challenging process of obtaining oxygen-free surfaces of uranium systems.

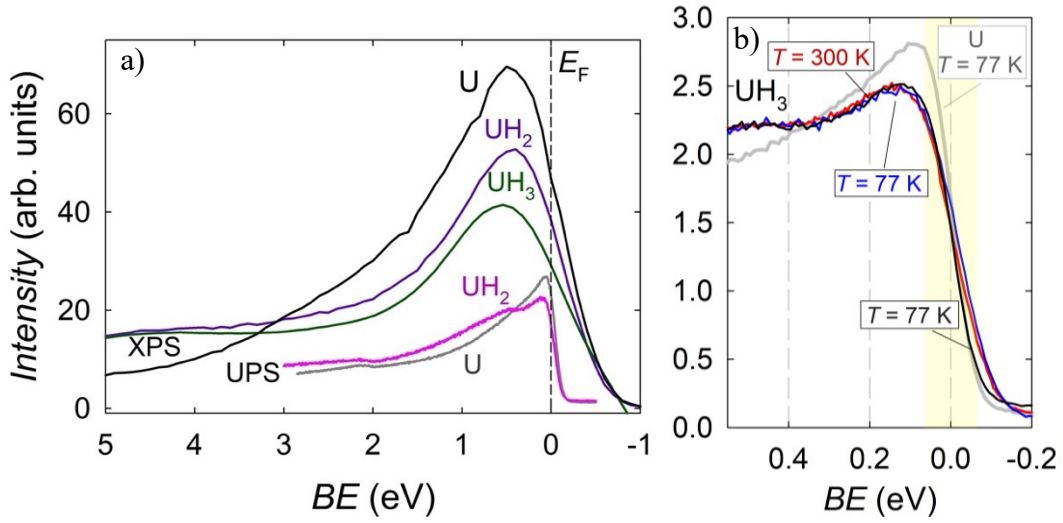


Fig. 3.2 (a) Valence-band XPS and UPS (He II) photoelectron spectra of $UH_3$ and $UH_2$ compared to U metal. (b) Details of He II UPS spectra of $UH_3$. The UPS spectra of

$UH_3$ are very similar to $UH_2$. The UPS spectra of $UH_3$ do not vary between the paramagnetic ($T$ = 300 K; red) and ferromagnetic (77 K; blue) states. The spectrum with enhanced energy resolution at $T$ = 77 K (black) has the reduced Fermi level broadening visible only above the Fermi level. The maximum located at 120 meV below the Fermi level is not affected by the Fermi-Dirac broadening with the given spectrometer energy resolution, marked by the yellow rectangle. The spectrum of elemental U for the same temperature and energy resolution (gray) exhibits a monotonous increase up to the Fermi level cut-off, forming a maximum at 90–100 meV. The comparison demonstrates that the U hydride has the dominant feature separated from the Fermi level.

The high-resolution UPS spectra presented in Fig. 3.2 (a) provide a complementary view of valence band photoemission. The intensity, mainly stemming from the emission of the 5*f* states for a photon energy of 40.81 eV (He II spectra), increases as it approaches the Fermi energy. Unlike in U metal, this increase shows a shoulder at 0.5 eV, followed by a further rise up to the Fermi level.

A closer examination of the region around the Fermi level (Fig. 3.2 (b)) reveals that the peak is not formed by a density of states that gradually increases with energy (as observed in elemental U), which would be limited by the Fermi-Dirac statistics. Instead, it is positioned at approximately 120 meV, i.e. below the range of Fermi-Dirac broadening. The few UPS scans taken in the ferromagnetic state ($T$ = 77 K) did not reveal any significant variations compared to the paramagnetic state except for a slightly better resolution due to reduced Fermi-Dirac broadening.

The DMFT calculations (Fig. 3.3) yield a spectral function that characterizes a reaction of the system to a photoexcitation event and that can be directly compared with photoemission spectra, which are not necessarily reflecting the ground-state density of states obtained in DFT and DFT + $U$ methods. These calculations indicate that the spectral characteristics primarily come from the dominant atomic final-state $5f^2$ multiplets, remaining after photoexcitation from the initial $5f^3$ state. Specifically, the main line $^3H_4$ is found near the Fermi level, while the first excited line $^3F_2$ contributes to a shoulder at a binding energy of 0.5 eV [109]. The multiplet structure observed in the valence-band spectra clearly indicates strong intra-atomic electron-electron correlations, which emerge gradually in 5*f* band systems as the bandwidth decreases.

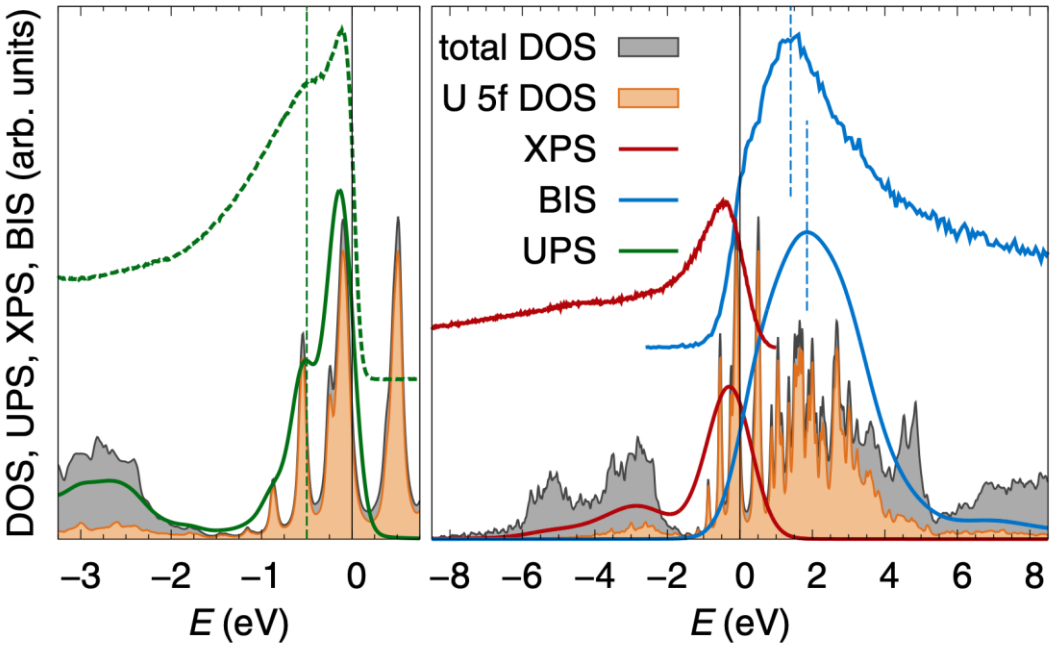


Fig. 3.3 VB spectra for the paramagnetic phase of α-$UH_3$ computed with LDA + DMFT are compared with the experimental spectra: UPS (green, photon energy 40.81 eV), XPS (red, photon energy 1486.6 eV), and BIS (blue). The experimental spectra are shifted up along the vertical axis for clarity. The theoretical spectra are constructed as linear combinations of the orbital-resolved spectral densities (denoted as DOS) weighted with appropriate photoionization cross-sections [110]. Gaussian broadening with FWHM 0.27 eV (UPS) and 1.3 eV (XPS and BIS) is applied to the theoretical spectra to model the instrument resolution [109].

The size of the U moments, approximately 1 $\mu_B$, is small in comparison to localized $f^2$ or $f^3$ states (3.20 and 3.27 $\mu_B$, respectively, in the *L*-*S* coupling scheme). Moreover, the presence of significant spontaneous magnetostriction, leading to an increase in volume in the ferromagnetic state, suggests additional spin splitting induced in the ordered state [111]. This phenomenon is attributed to the band character of magnetism. The increase in the $\gamma$ coefficient to 60 $mJmol^{-1}K^{-2}$ in the paramagnetic state represents the other side of the same coin [12]. Finally, the decrease in $T_C$ under pressure indicates that the magnetism of $UH_3$ primarily originates from the 5*f* band, but its modest pressure or volume derivatives suggest that the band picture does not tell the whole story, and a partial 5*f* localization must be acknowledged [112].

Experimental BIS spectra for $UH_3$, shown in Fig. 3.4, exhibit a noticeable difference with spectrum of U metal shown in Section 1.3.3.3 (Fig. 1.20). The distinct

division between $5f_{5/2}$ and $5f_{7/2}$ is not reproduced in the hydride. Calculations suggest that the additional exchange-correlation splitting in ferromagnetic $UH_3$ is the reason for this discrepancy. Consequently, the BIS spectrum exhibits one clear maximum above $E_F$ in $UH_3$ at 1.5 eV.

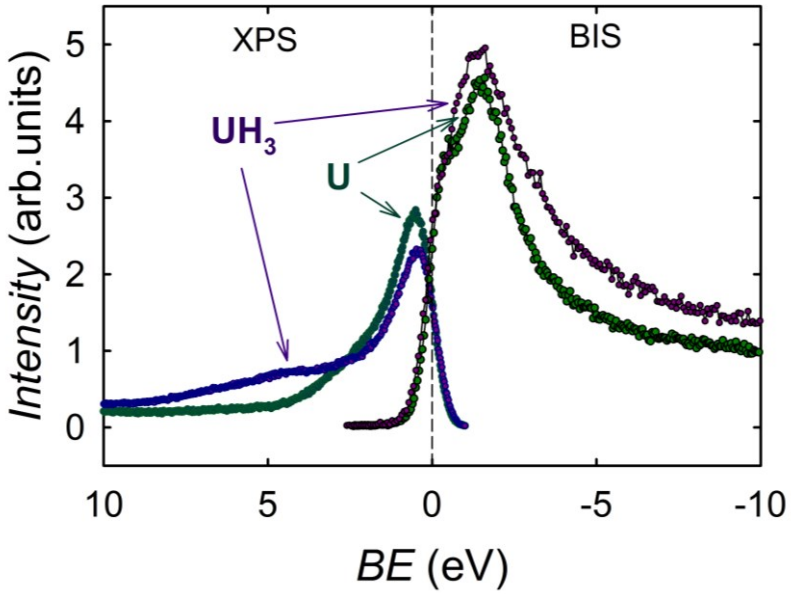


Fig. 3.4 Combined XPS and BIS spectra of U metal (green) and $UH_3$ (violet).

Comparison of both spectra at higher energies reveals additional intensity, manifested as slower decay, for the hydride. This can be associated with the 6*d* and 7*s* states transferred from the occupied part of the valence band. However, their effect on the BIS spectra is limited. The Bremsstrahlung emission follows the same probabilities as XPS spectra taken with the same photon energy. Hence, the spectra are dominated by the 5*f* states, the photoexcitation cross-section of which is more than one order of magnitude higher than for the 6*d* and 7*s* states of uranium [113].

#### 3.1.1.2. Core-level spectra

To recap the findings outlined in Section 1.3.3.1 regarding the core-level 4*f* spectra of uranium hydrides and show consistency of current results to the previous studies, U-4*f* lines are presented at Fig. 3.5. The $4f_{5/2}$ and $4f_{7/2}$ peaks are wider and more asymmetric compared to U metal. The less steep high binding energy side indicates an enhanced density of states at the Fermi level, resulting in energy loss of photoelectrons through an electron-hole pair creation. Additionally, the peak intensity decreases. Notably, only a tiny shift of the peak maxima toward higher binding

energies is observed, amounting to approximately 0.2 eV. This slight "chemical" shift can be attributed to the relatively invariable 5*f* occupancy in both U metal and its hydrides. The 5*f* states of U are close to the 4*f* core states.

As deduced from ab-initio calculations [28], the polar bonding predominantly influences outer electrons, namely the 6*d* and 7*s* states, leading to repopulation of the H-1*s* states in the hydrides. Consequently, the shifts in the shallower levels (U-5*d* and 6*p*) are more pronounced, although their intensities are significantly weaker and less suitable for quantification (Fig. 3.6 (a) and (b)). Indeed, bigger shifts of 0.6 eV for the 5*d* peak and over 1 eV for the $6p_{3/2}$ peak between U and its hydrides were detected. Interestingly, $UH_2$ and $UH_3$ exhibit practically identical energy and shape in all cases, with only minor differences in intensities, similar to what was observed in the 4*f* spectra.

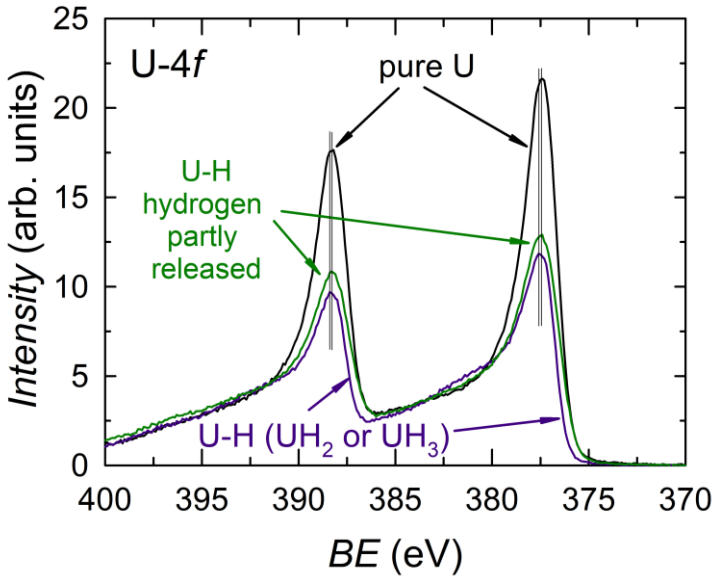


Fig. 3.5 U-4*f* core level spectra of U metal (black) and U-H systems. The spectra of a hydride ($UH_2$ or $UH_3$, depicted in blue) is presented alongside the U-H spectrum with partially released hydrogen (depicted in green). Each spectrum consists of the $4f_{5/2}$ and $4f_{7/2}$ lines, split by 11 eV due to the spin-orbit interaction.

In Fig. 3.5, spectra of the U-H samples prepared without cooling of the substrate for deposition times shorter and longer (by roughly a factor of 2) than the typical time of 1000 seconds are shown (green). In the latter scenario, the hydrogen concentration is likely lower due to excessive heating of the surface by the sputter source.

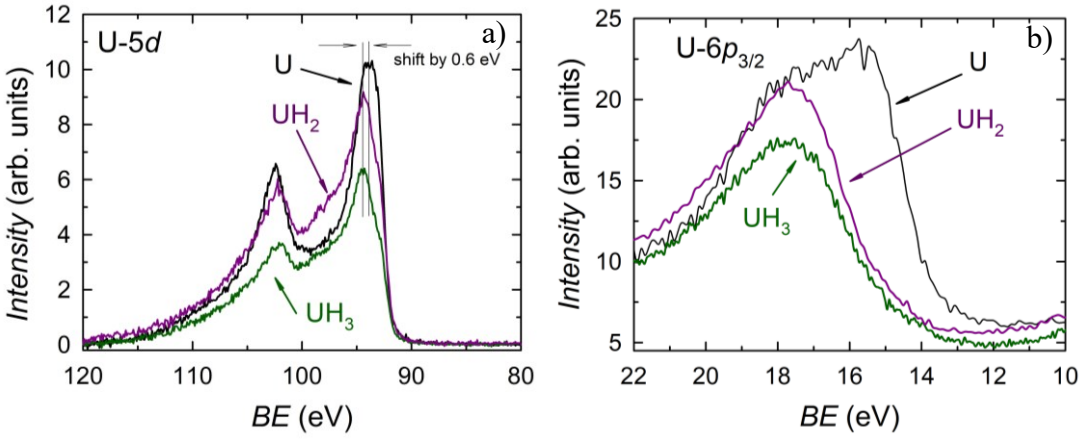


Fig. 3.6 U-5*d* (a) and U-6$p_{3/2}$ (b) core level spectra of U, $UH_2$ and $UH_3$. Each spectrum of U-5*d* states consists of the 5$d_{3/2}$ and 5$d_{5/2}$ peaks, separated by 8 eV due to the spin-orbit interaction.

It is visible that the intensity of the peaks begins to increase from the fully hydrogenated state towards the level found in U metal films, although it still closely resembles the fully hydrogenated state. Subsequently, it was determined that the longer runs gave predominantly $UH_2$, while the shorter ones exhibited the structure of β-$UH_3$. However, in cases with higher peaks (and nearly complete loss of asymmetric shape), the films were determined as containing a mixed phase composition of non-hydrogenated phase and $UH_3$. Such situation can be identified on the basis of magnetization data (see below in the section on U-Zr-H).

### *3.1.2. U-Zr and U-Zr-H*

#### 3.1.2.1. VB XPS and UPS

Valence band spectra were obtained by XPS (h$\nu$ = 1486.6 eV) for various U-Zr alloy compositions are shown in Fig. 3.7 alongside the spectrum of pure U film. The spectral intensities were not adjusted; thus, they are reflecting the decreasing U concentrations across the alloy series. In the valence-band spectra, the emission associated with the 5*f*-6*d* states, which extends nearly 5 eV below the Fermi level ($E_F$) in U metal, experiences a reduction in energy to approximately 4 eV below $E_F$ with increasing Zr concentration. Although the Zr-4*d* states theoretically possess a slightly higher photoexcitation cross section compared to U-5*f*, the overall intensity decreases. Additional insights are provided by the U-6*p* spectra (6$p_{3/2}$), which exhibit a characteristic broad shape with a plateau in the case of U metal. While this shape is

retained at lower Zr concentrations, 85% Zr substitution results in a narrower peak, with a slight shift in spectral weight towards higher binding energies.

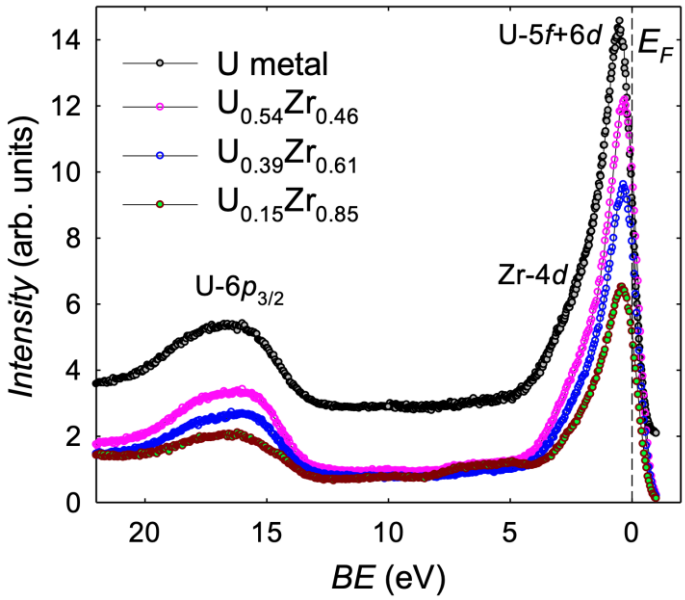


Fig. 3.7 VB XPS spectra of U metal and U-Zr alloys. The spectrum of U was shifted up. The dashed line indicates the Fermi level. The intensities of the spectra for the alloys are intact.

Fig. 3.8 compares VB XPS spectra of Zr hydride with U-Zr hydrides for two different Zr concentrations. The visible difference in spectra is the loss of intensity attributed to the H-1*s*+Zr-4*d* hybridization and bonding, which appears around 6 eV [114], suggesting the release of Zr from bonding with H when U is added to the system (proven by core-level spectra features described later). The Zr-H sample was not analyzed off situ for its crystal structure, and the amount of H in Zr-H films was not identified.

It is worth comparing valence-band XPS spectra with ultraviolet photoelectron spectroscopy (UPS) ones, which have a limited energy range but a higher energy resolution. Due to lower kinetic energy of photoelectrons and consequent shorter mean free path, the information is more surface sensitive.

Typically, spectra using HeI ($h\nu = 21.2$ eV) and HeII (40.8 eV) photons were recorded, with the latter exhibiting a significantly higher photoexcitation cross section for the U-5*f* states (see Fig. 1.18). UPS spectra of U-Zr alloys and hydrides are compared with those of pure U and $UH_3$ in Fig. 3.9 and Fig. 3.10.

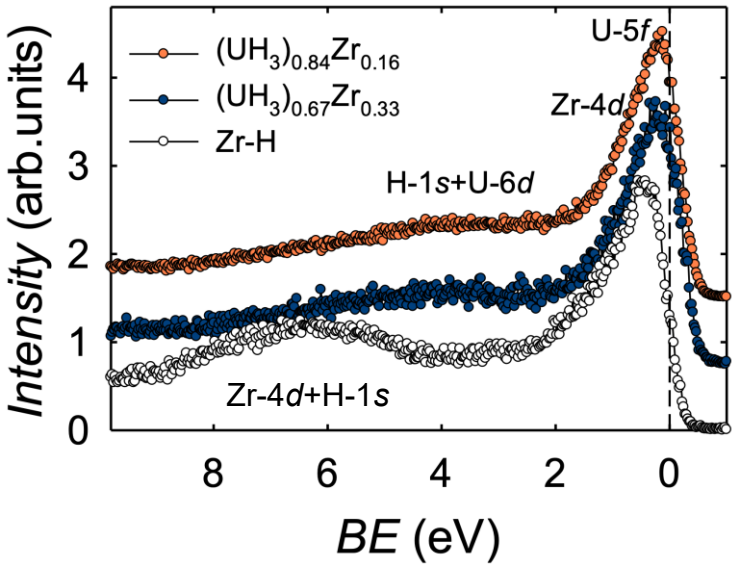


Fig. 3.8 VB XPS spectra of Zr hydride and U-Zr hydrides with 16 and 33 at.% Zr.

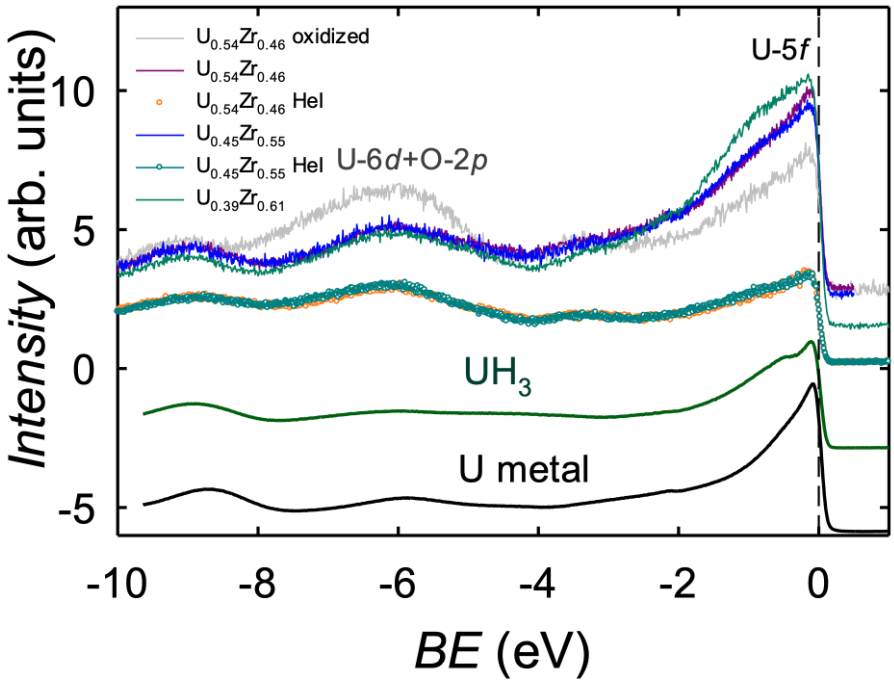


Fig. 3.9 VB UPS spectra of U metal and U-Zr alloys. One can compare the alloys $U_{0.54}Zr_{0.46}$, $U_{0.45}Zr_{0.55}$, and $U_{0.39}Zr_{0.61}$ in HeII with respective HeI spectra (for the two former concentrations) and with $UH_3$ and U metal in HeII. The effect of partial oxidation on $U_{0.54}Zr_{0.46}$ is shown for the HeII spectrum (grey) as increase in the energy range 4-7 eV below $E_F$, where the O-2*p* states appear. In comparison with this spectrum, the one with 61% Zr, even if slightly oxidized, has the shoulder at 1 eV binding energy intrinsic; practically no increment in the range of the O-2*p* states is visible.

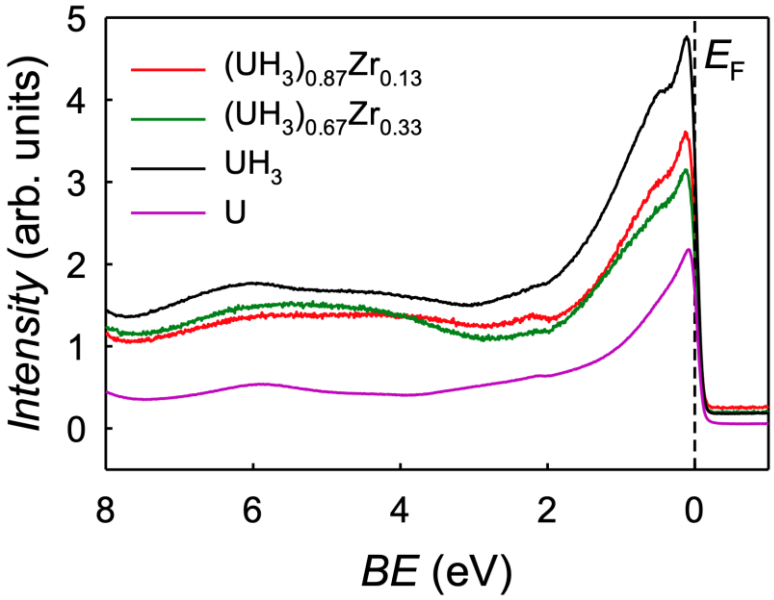


Fig. 3.10 HeII spectra of U-Zr hydrides compared with pure U and $UH_3$.

As observed earlier, the valence band emission increases for the alloys up to the Fermi level, while the total intensity near the Fermi level decreases with increasing Zr concentration (deduced from the data adjusted to the same background, not shown on the figure though). The spectrum of the 61 at.% Zr alloy initially resembled that of $UO_2$, but surprisingly the oxygen content is not higher than in the other films (well below 5% calculated from the O-1*s* line intensity), and oxidized alloys exhibit distinct characteristics. The intensity increase around 1 eV with increasing Zr concentration seems to be intrinsic (corresponding to Zr-4*d* line).

Turning to the hydrides (Fig. 3.10), a noteworthy feature of the spectrum — the shoulder around 0.5 eV — becomes less pronounced with increasing Zr concentration, while the 5*f* peak broadens on the higher binding energy side due to the contribution from Zr. The origin of the small cusp at 2.2 eV, present in both alloy and hydride spectra, remains unclear.

#### 3.1.2.2. Core level XPS

Examining the U-4*f* lines in high resolution (with $E_0$ = 20 eV) across different Zr concentrations in alloys (Fig. 3.11 (a)) shows no energy shift; the lines remain at 377.2 eV and 388.0 eV. Hydrides (Fig. 3.11 (b)) display a 0.2 eV shift of maxima to higher binding energies, similar to $UH_3$. The energies are 388.2 eV and 377.4 eV for the $4f_{5/2}$ and $4f_{7/2}$, respectively. The shape (hydride peaks are more asymmetric) does

not change in either case compared to systems without Zr substitution. Comparison with slightly oxidized alloy reveals traces of $UO_2$ at approximately 4 eV higher energies.

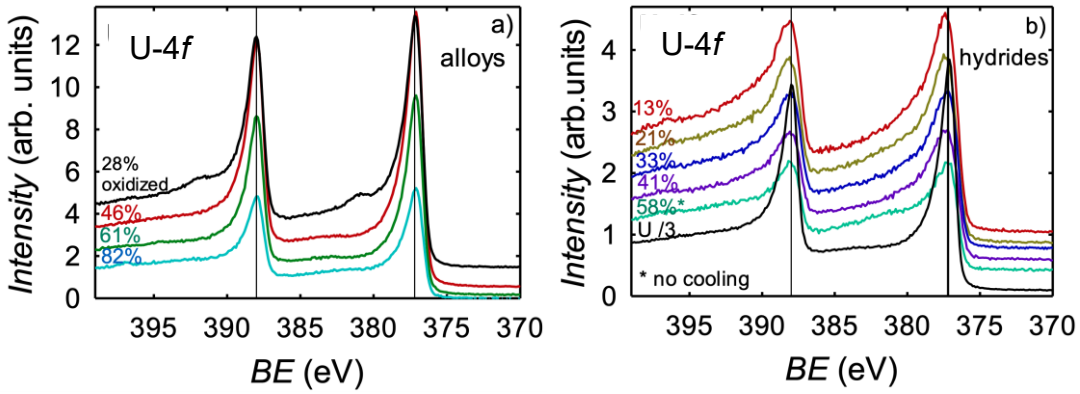


Fig. 3.11 Photoelectron spectra U-4*f* lines for varying Zr concentrations: (a) U-Zr alloys; (b) hydrides. Percent numbers correspond to the concentration of Zr in films. Vertical lines indicate peak positions in pure U metal. The pass energy for all the spectra was $E_0 = 20$ eV. The hydrides were deposited at $T = 100$ K (except for $U_{0.42}Zr_{0.58}$-H which was deposited without substrate cooling).

The feature around 396 eV observed in the hydrides may tentatively be linked to the N-1*s* emission (at 396.2 eV). This suggests possible air contamination of the $H_2$ gas, with $N_2$ remaining after the $O_2$ capture by the Oxisorb cartridge (it should be mentioned that this feature is present in the data for the samples deposited with the $LN_2$ trap. This is understandable when considering the fact that at pressures below the atmospheric one, Nitrogen liquifies at lower temperatures than 77 K, so only some fraction of $N_2$ impurity condenses on the walls of the trap. In addition, the feature becomes more pronounced when the substrate is cooled during deposition). Referring to the $UN_x$ systems [44] allows us to estimate the N/U ratio to be < 0.1. However, an alternative explanation is that the feature is actually a shake-up satellite of the $4f_{5/2}$ emission. The satellite corresponding to $4f_{7/2}$ peak would have been covered by the $4f_{5/2}$ peak, making it difficult to resolve. Nonetheless, this feature is not evident in earlier 4*f* spectra on pure U films, making an extrinsic origin a more plausible explanation.

A notable discovery is the higher intensity observed in the energy range of 381-385 eV in the hydrides, indicating intrinsic intensity in these materials. It is surprising as typically a satellite arises due to electron-electron correlations in this energy range. However, the hydrides show a continuum of gradually decreasing intensity, which, as

observed at $4f_{5/2}$, can extend over a 10 eV range. While the presence of two broad satellites might be assumed, the data do not provide clear evidence of this.

XPS 4*f* core-level spectrum is a good indicator of the hydrogenation completeness (if we can say so for the deposited films) of the sample. Hydride films with the inclusion of the non-hydrogenated phase exhibit higher and more symmetric peaks, (Fig. 3.12 blue line). Spectroscopic data were subsequently corroborated with the magnetization studies (wasp-waist hysteresis loops described in Chapter 3.4.2).

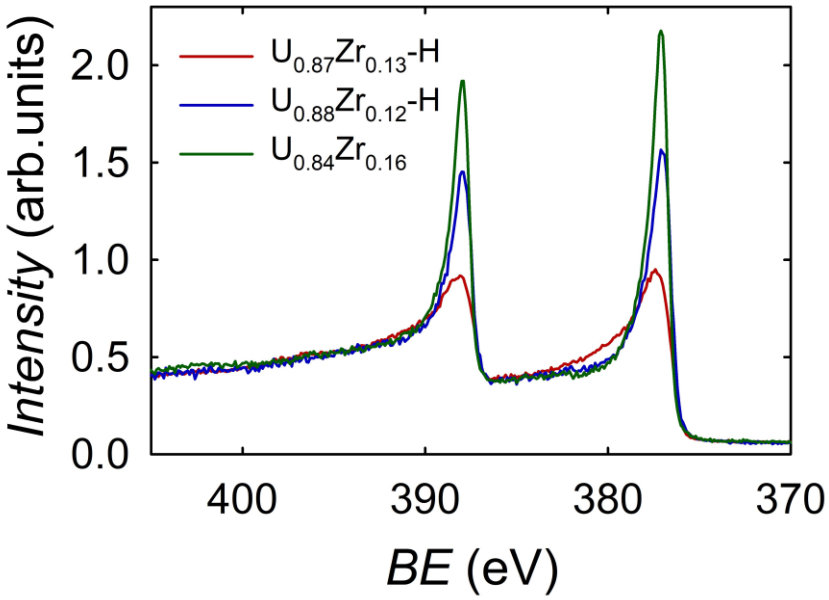


Fig. 3.12 Comparison of XPS spectra of the U-4*f* lines for "good" hydride film (thin $U_{0.87}Zr_{0.13}$-H film, red line), film with non-hydrogenated minor phase (thick film $U_{0.88}Zr_{0.12}$-H, blue line, magnetization data presented on Fig. 3.32), and film of an alloy (thin film $U_{0.84}Zr_{0.16}$, green line) with similar Zr concentrations. Intensities were normalized to the background.

In Fig. 3.13, complementary Zr-3*p* spectra are presented. Similar to the U-4*f* lines, a non-systematic shift of 0.1-0.2 eV to higher binding energies has been observed in the alloys (compare to Mo-substituted films, Fig. 1.17). Unlike the U-Mo case with a charge transfer from U to Mo there is no such polarity between U and Zr (which have very similar electronegativity).

However, a weakly oxidized film shows a notable 0.5 eV shift towards higher energies (Fig. 3.13 (c)). This can be attributed to the presence of lower Zr oxides, which precede the formation of $ZrO_2$ with a separate peak located at binding energies 3 eV higher [115]. The main line appears at 330.3 eV for $3p_{3/2}$ in elemental Zr, 330.6 eV in its hydrides (presumably $ZrH_2$). Nevertheless, in the alloyed hydrides, the

Zr-3*p* emission returns to the position in Zr metal, meaning that the presence of U pulls Zr from the bonding with H. A similar pattern was observed when hydrogenating U-Mo alloys.

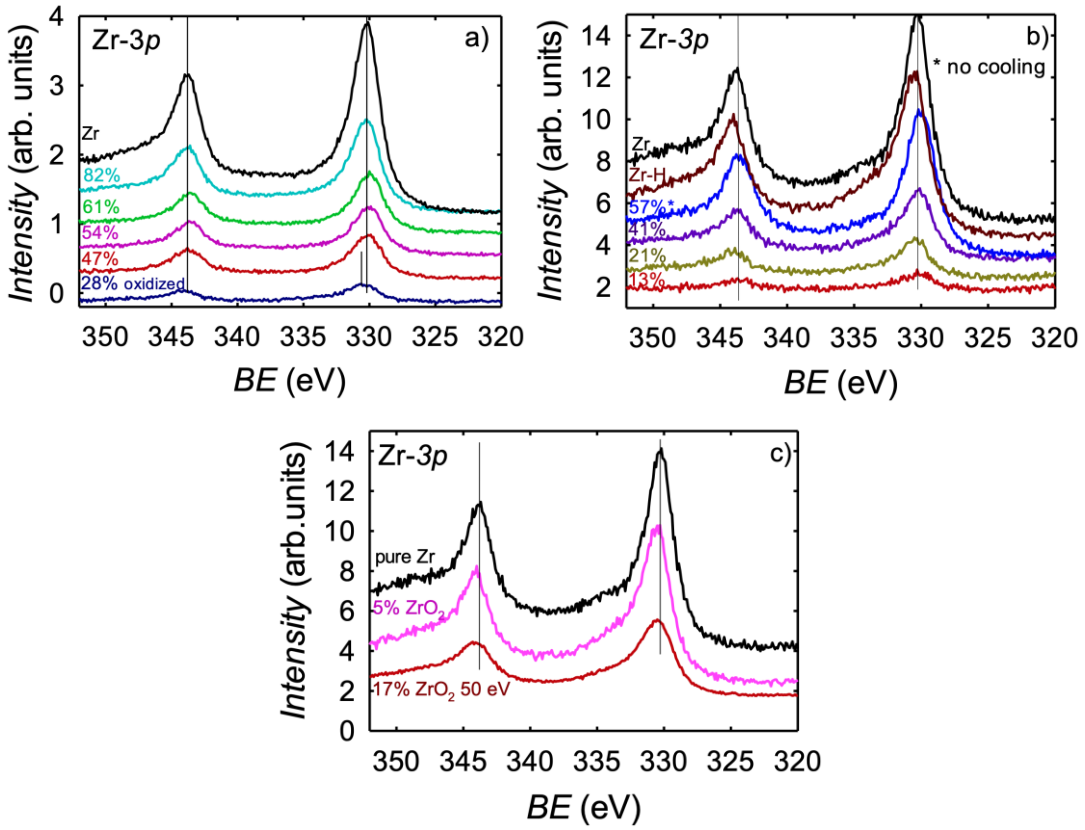


Fig. 3.13 Photoelectron spectra of the Zr-3*p* lines for varying Zr concentration in (a) alloys; (b) hydrides; (c) Zr hydrides with different oxidation levels compared to Zr metal spectrum (black lines). Vertical lines indicate positions of 3*p* peaks in elemental Zr.

As a side information, some U-5*d* spectra for U-Zr alloy (61% Zr) and hydrides were collected for comparison with pure U (Fig. 3.14). The alloy with 61% Zr does not show any shift of $5d_{3/2}$, whereas there is some variation in $5d_{5/2}$. Spectra of the hydrides are very similar to $UH_3$.

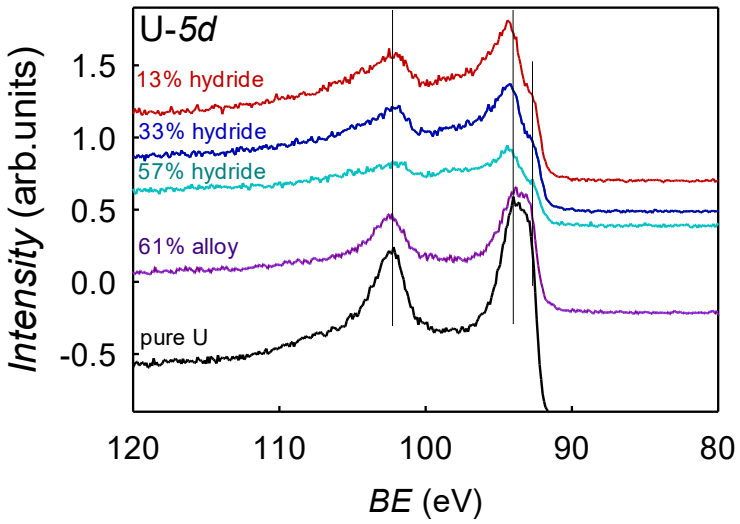


Fig. 3.14 XPS spectra of U-5*d* lines for U-Zr hydrides with varying Zr concentration (labelled above each spectrum). Pure U and $U_{0.39}Zr_{0.61}$ alloy spectra are added for comparison.

### *3.2. Structure and physical properties of U-T thin films*

The next step after *in situ* XPS in the characterization of thin films is using X-ray diffraction methods for structure determination and following correlation with their physical properties.

#### *3.2.1. Structure of U-T films*

Structure analysis of thin films is challenging, hence a thorough investigation corresponding only to $U_{0.92}Mo_{0.08}$ film will be presented. For the series of U-Zr films some generalized conclusions about the structure details will be included in the end of the subchapter.

Fig. 3.15 displays a comparison of GIXRD profiles for the $U_{0.92}Mo_{0.08}$ film, where the angle of incidence $\alpha_i$ varies from 0.3 to 10°. The increase of the incidence angle of the primary beam in the PB geometry increases the penetration depth of X-rays. As $\alpha_i$ alters, the XRD patterns exhibit changes, hinting at the presence of a contaminated surface layer. This layer is likely composed of a U–Mo phase with oxygen, a consequence of the film interaction with air and moisture after being removed from the vacuum chamber. Basically, only the $UO_2$ phase is distinguishable on the pattern, which corresponds to 0.3° angle.

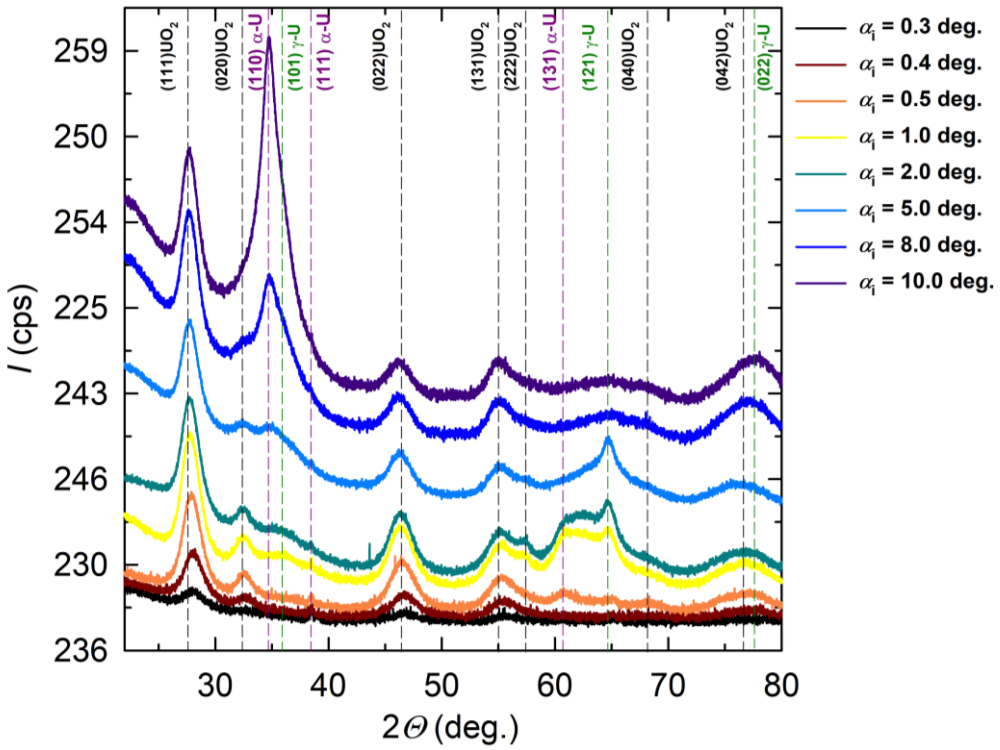


Fig. 3.15 XRD patterns of the $U_{0.92}Mo_{0.08}$ film obtained in the parallel beam geometry for different angles of incidence of the primary beam ($\alpha_i$ = 0.3–10°). Identified peaks and phases are denoted. Some of the patterns were shifted up for better clarity of the figure.

The XRR analysis (not depicted here), employing a two-layer model, provided the thickness of the $U_{0.92}Mo_{0.08}$ layer as 111 ± 10 nm (with a density of 15.8 ± 3.0 g/cm$^3$ and roughness of 6.1 ± 1.5 nm). This layer is covered by a 38 ± 8 nm-thick Mo–U oxide layer (with a density of 10.6 ± 0.5 g/cm$^3$ and roughness of 1.5 ± 0.5 nm). The profiles in Fig. 3.15 could not be interpreted with a single phase of bcc γ-U-Mo. To identify the peaks, a low-resolution wide reciprocal space map (RSM) of the $U_{0.92}Mo_{0.08}$ film was recorded (see Fig. 3.16). Circles from the polycrystalline phase of $UO_2$ indicate that the upper layer contaminated by oxygen lacks any texture, whereas the U–Mo layer beneath is highly textured, with the γ-U-Mo phase growing with two different texture components, namely (121) and (101), perpendicular to the sample surface. For simulation, the lattice parameter of $a$ = 3.50 Å was used for the γ-U-Mo phase.

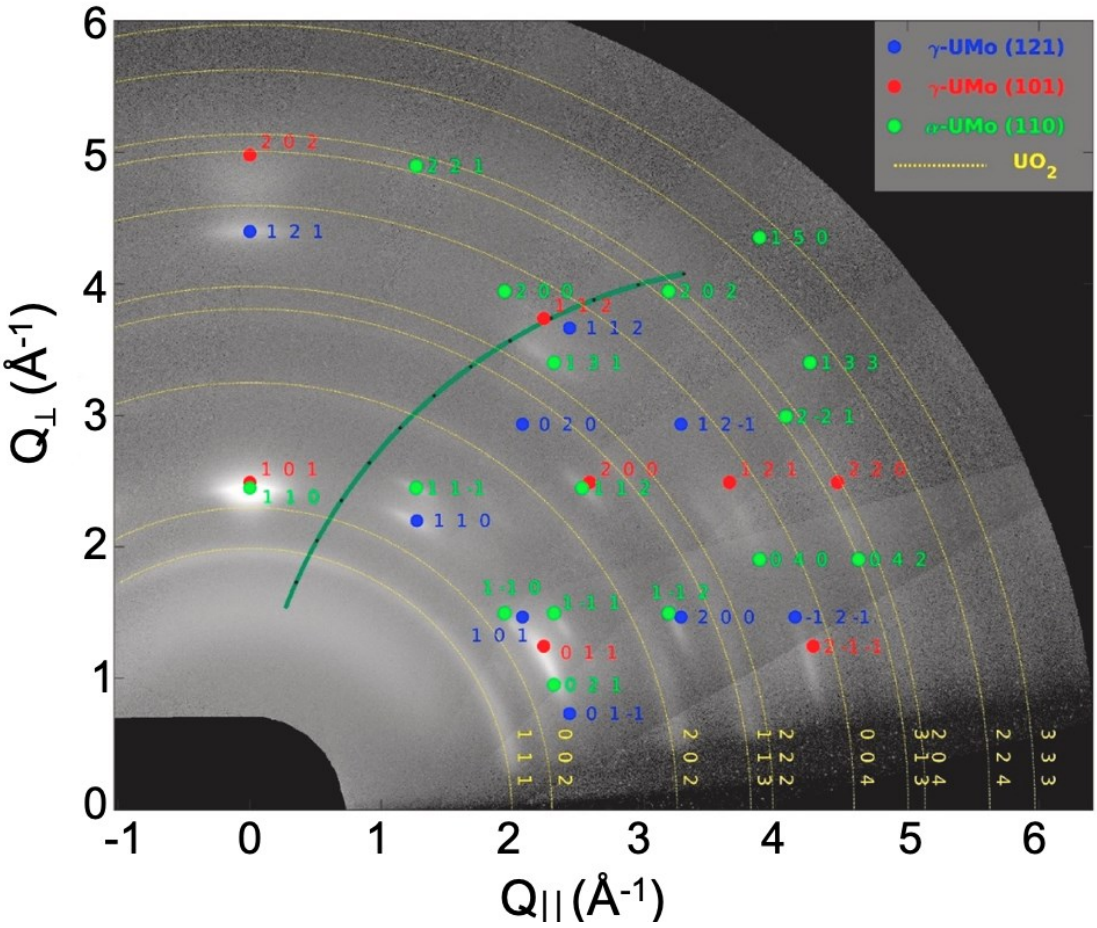


Fig. 3.16 Low-resolution wide RSM mapping of the $U_{0.92}Mo_{0.08}$ film, presenting a complete cut of one quadrant in reciprocal space. Circles indicating the polycrystalline $UO_2$ phase (yellow) and (*hkl*) indexes of Bragg reflections from textured phases are highlighted. The γ-U-Mo phase exhibits two distinct texture components: (121) in blue and (101) in red. The α-U phase displays a (110) texture in light green. The dark green line corresponds to the PB scan at $\alpha_i = 1°$ (refer to Fig. 3.15).

It was established previously that unalloyed γ-U, acquired through the hot rolling of the cast as reported in Ref. [23], displayed a lattice parameter of 3.474 Å. Considering the documented trend of decreasing lattice parameter in γ-U-Mo with increasing Mo concentration [23,116], the present simulation yields an apparently elevated value for the *bcc* U–Mo with $x = 0.08$. This disagreement can be ascribed to the substantial influence of strains and defects, factors not considered in this simulation. This idea is corroborated by Ref. [117], where higher lattice parameters in polycrystalline $U_{1-x}Mo_x$ films were found comparing to single-crystalline ones. However, the closest Mo concentration, realized in a single-crystalline film with $x = 0.1$, showed $a = 3.423(1)$ Å, significantly lower than in the present simulation.

Prior investigations indicate the observation of a pure cubic γ-U phase in splat-cooled samples at 13–15 at.% Mo [116,118]. In the thin films of $U_{1-x}Mo_x$ [117], the pure cubic uranium γ-phase was established for $x \geq 0.22$, while below this Mo concentration, the resultant thin film alloys exhibited a mixed α-γ uranium phase composition. Given the Mo concentration in the described sample $x = 0.08$, the presence of the α-U-Mo phase was identified, as well, which exhibits growth in the (110) direction perpendicular to the sample surface. All the U-Mo films prepared for these studies have a lower Mo concentration than the γ-U limit, thus all of them showed a mixed phase composition.

As films of U-Zr were intentionally left without cover for resistivity measurements, it is challenging to define structure from XRD patterns as signal from $UO_2$ layer surpasses that from other phases (even more than for U-Mo films, and even for higher incidence angles). Interestingly, the film with high Zr concentration ($U_{0.35}Zr_{0.65}$, α-U phase, strongly textured, (110) preferred orientation) is almost oxide-free even on the surface. The main conclusion is that similar to the films with Mo substitution, films with Zr are of a mixed composition of α- and γ-U. The increase of Zr concentration suppresses the presence of α-U and supports γ-U. The same tendency was found for bulk U-Zr alloys prepared by splat cooling [116]. The threshold for stabilization of pure γ-U phase (30 at.% Zr in bulk) seems to be relevant for film samples as well with $U_{0.69}Zr_{0.31}$ sample showing mainly γ-phase. δ-$UZr_2$, spectated by authors [119] in their U-Zr films, is probably present in our samples, peaks are difficult to distinguish (overlapping with those from γ-U). Although for defining fine structure variations a thorough XRD analysis is needed.

### *3.2.2. Transport properties of U-T films*

#### 3.2.2.1. Superconductivity

It is well known that β- and γ-uranium ($T_c$ = 1.8 K [4]) are bulk superconductors at zero pressure. The situation with α-U is less clear. “Filamentary” superconductivity with $T_c$ = 0.7 K [120] was found in single crystals with RRR = 206, however, no superconductivity was found in high-quality single crystals with RRR = 570 [121]. Bulk superconductivity was revealed only under pressure with suppression of the charge-density state. Later, the presence of SC state in α-U was shown to be based

only on a limited volume of sample also in rapidly solidified splat, exhibiting only a weak anomaly of heat capacity and low $H_{c2}$ [116].

All previously investigated U-T alloys (as-cast, thermally treated or splat-cooled [116,122–124]) are conventional BCS superconductors with superconducting (SC) transition below 2.11 K (the highest transition temperature was found for U-15 at.% Mo sample). In the case of samples with mixed phase composition (both α- and γ-U) there are two variants of an abrupt drop in resistivity temperature dependence indicating SC transition. Either a broad transition of α-phase is present (if γ-U is a minor phase not sufficient for the evolution of bulk SC, i.e. in splat-cooled U), or two drops (representing SC transitions of α- and γ-U as in U-6 at.% Mo [122]) are observed.

Despite the superconducting ground state of the U-T alloys, only one of the films ($U_{0.92}Mo_{0.08}$) from our studies exhibited superconductivity. The rest of the samples (both with Mo and Zr substitutions) did not show SC transition down to the lowest $T$ limit of our studies (0.4 K).

It was established that the superconducting transition in the $U_{0.92}Mo_{0.08}$ thin film starts at $T = 0.55$ K [125]. The true zero resistance state is reached at 0.4 K (Fig. 3.17 (a)). As expected for conventional BCS-type superconductors, the transition shifts towards lower temperatures with increasing external magnetic field. The upper critical field for the thin U–Mo film can be estimated from WHH theory as $\mu_0 H_{c2} = 1.0$ T (Fig. 3.17 (b)), i.e. lower that for the splat-cooled U–Mo ($\mu_0 H_{c2} > 5$ T) [118], but more than three-times that of α-U.

The attempt to estimate the coherence length by using the upper critical field $H_{c2}$ in the framework of the weak-coupling theory (Eq. 1.7) gives the coherence length of 18 nm for thin film, compared with $\xi_0 = 7$ nm for U-15 at.% Mo splat. Considering the critical field exceeding that of α-U (0.33 T [126]), superconductivity in $U_{0.92}Mo_{0.08}$ film is unlikely to be related to a residual α-U phase.

While zero resistivity is a classical signature of superconductivity, it is important to note that such measurements cannot discriminate between bulk and filamentary states (the term “filamentary” is often used in a broad sense when there is a contiguous superconducting path, e.g. from grain boundaries, even if it is formed by “filaments”). This is because resistance drop is observed whenever a SC percolation path exists.

Unfortunately, heat capacity [122] or high-sensitivity AC magnetization measurements [120], which could disentangle the problem, are impossible or difficult

to give absolute values for thin film samples due to the prevailing signal from the substrate.

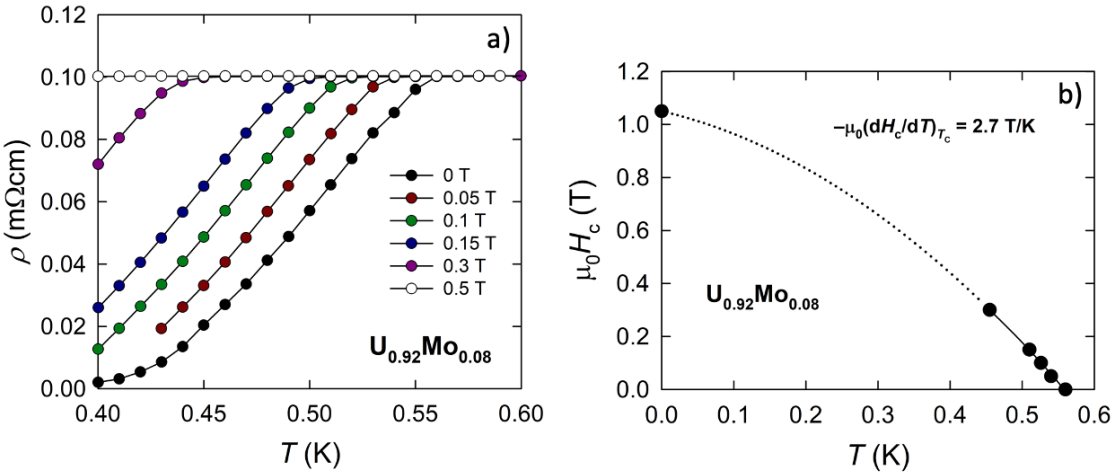


Fig. 3.17 Low-temperature dependencies of resistivity of the $U_{0.92}Mo_{0.08}$ thin film in various fields (a) and critical magnetic field $H_c$ vs. temperature $T$ (b). The fit by second-order polynomial function is shown by dotted line.

The possible reason for the absence of the γ-U bulk superconductivity in our thin films may be the crystal structure details of our samples. There are two situations for the thin films for being superconducting: a totally amorphous state [127,128] or epitaxially growth single crystal films [129–131]. Typically, amorphous superconductors are strongly coupled Type II superconductors, some of them showing $T_c$ higher than their crystalline counterparts. In the case of single crystal films, disorder (structural or chemical) suppresses superconductivity. Concerning our films, those are neither amorphous nor single-crystalline. Apparently, the structural disorder on a lengthscale similar to the BCS coherence length is the most detrimental for superconductivity. Consequently, our films with γ-U structure and significant disorder on the mesoscopic scale do not show superconductivity. Another explanation, which cannot be excluded, is the distribution of α- and γ-U phases in the film in a such manner that continuous path for electric current is not created.

#### 3.2.2.2. Uranium Alloys. Resistivity

Fig. 3.18 (a) compares the resistivity in the normal state for thin films with Mo and Zr substitutions and some of the splat-cooled materials obtained earlier. Data for bulk splat-cooled samples were adopted from Ref. [116] and [122]. The pure-U splat (consisting of an α-U phase) exhibits a common metallic behavior: quadratic

temperature dependence below 50 K and almost linear dependence up to 300 K with a positive temperature coefficient of resistivity, TCR, ($d\rho/dT > 0$). Increasing the Mo content significantly increases the absolute low-temperature resistivity values (due to atomic disorder), thus dramatically changing $\rho(T)$ overall dependence. As pointed out first by Mooij [132], this is a generic behavior of substitutional solid solutions of elements with very different scattering potential. In particular, $\rho(T)$ curves rapidly flatten with increasing Mo concentration, getting a negative slope ($d\rho/dT < 0$) and saturation in the low-$T$ limit for alloys with pure γ-U structure (> 11 at.% for Mo). Interestingly, a small amount of α-U in the thin film sample $U_{0.92}Mo_{0.08}$ does not manifest itself in the resistivity data. The negative TCR and high absolute values exceeding 100 μΩcm are comparable to those observed for bulk materials with similar composition [116,133]. We assume that the low α-phase concentration and its space distribution is not sufficient for dramatical change of the resistivity slope.

The tendency in variations of $\rho(T)$ is analogous for most of T metal substitutions. An exception is the U-Zr case. For the Zr substitution in bulk systems, the negative slope has not developed in U-30 at.% Zr (lowest Zr concentration which granted pure γ-U phase) yet [122]. Instead, a very small but still positive slope of the temperature dependence was found. A negative temperature coefficient was reported for U-Zr system with 70 at.% Zr [134]. In thin film form, the negative slope is already visible for much lower Zr concentration, sample $U_{0.77}Zr_{0.23}$. And it is getting even higher for $U_{0.35}Zr_{0.65}$ film (Fig. 3.18 (b)). This fact can indirectly prove that disorder is responsible for negative values of $d\rho/dT$, as sputter deposition brings additional structural and chemical disorders to the studied systems. The significance of Zr is in its chemical similarity to U (electronegativities are 1.33 and 1.38 for Zr and U, respectively [135]), which does not evidently produce the sufficient variations of stochastic scattering potential for conduction electrons, needed to bring the weak localization phenomenon [136]. The weak localization is taken responsible for negative TCR of metallic alloys which have nothing to do with Kondo effect[2] and other magnetic phenomena.

[2] Kondo effect is a phenomenon where the resistivity increases while temperature decreases with a minimum at $T_K$ (Kondo temperature) due to scattering process different from scattering of electrons on lattice vibrations. Below $T_K$, the resistivity rises logarithmically (described by perturbation theory). This behavior is explained by the interaction between conduction electrons of non-magnetic host and localized magnetic impurities within the metal. The phenomenon occurs only at low temperatures [160].

In particular, the resistivity is increased due to a higher probability of backward scattering of electrons. Elevated temperature destroys the quantum coherence, which leads to a resistivity reduction [137]. A behavior, that breaks the Matthiessen's law[3], is not unique. Similar tendencies were observed in various amorphous systems [138], Heusler alloys [139], substitutionally disordered crystalline materials [140], and even in the moderately disordered uranium heavy fermion compound $URh_2Ge_2$ [141].

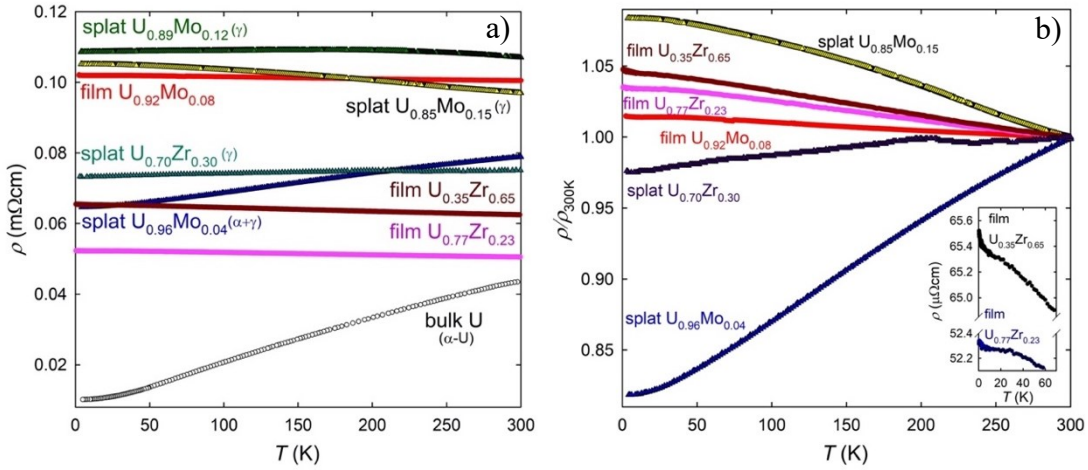


Fig. 3.18 Comparison of temperature dependencies of electrical resistivity (a) and normalized resistivities (b) for various U–Mo/Zr splats and bulk splat U (adopted from Ref. [116]) and selected thin-film U-Mo and U-Zr samples.

Unlike $\rho(T)$ curves of splats with negative slope which reach saturation at low-$T$ region, temperature dependences of all non-superconducting thin film exhibit a weak upturn, about the origin of which we do not want to speculate.

### *3.3. Structure and physical properties of U hydride thin films*

Similar to the films of U alloys, also the films of hydrides were subjected to XRD studies after the initial spectroscopy analysis. There are a few reasons that make the phase and structure analysis of uranium hydride thin films a challenging task. For instance, uncapped samples, intended for resistivity measurements, have the surface

[3] Matthiessen's rule states that the total resistivity ($\rho$) of metallic system is the sum of the resistivities due to different scattering mechanisms: $\rho(T)=\rho_0 + \rho_{e\text{-}ph}(T) + \rho_{mag}(T)+ \rho_{el\text{-}el}(T)$, where $\rho_0$ – the residual temperature-independent contribution due to impurities and imperfections; $\rho_{e\text{-}ph}(T)$ is the temperature-dependent electron-phonon scattering with $T^5$ dependence below the Debye temperature ($T \ll \Theta_D$) [161] for simple metals; $\rho_{mag}(T)$ is the temperature-dependent contribution due to magnetic interactions, this term exhibits a pronounced decrease below the temperature of magnetic ordering ($T_C$, $T_N$) due to gradually suppressed spin disorder; $\rho_{el\text{-}el}$ is the electron-electron contribution which follows the Fermi liquid scaling $aT^2$ at low temperatures.

severely contaminated with oxygen, hence the patterns exhibit a remarkable resemblance, differing only in subtle details around the peaks near 30 deg. In addition, both $UO_2$ and $UH_2$ (which does not exist in a bulk) possess *fcc* structures with relatively close lattice parameters of 5.46 Å and 5.36 Å [5], respectively. These structure similarities make it challenging to differentiate between them in the diffraction data. On the other hand, $UH_3$, comprising both metastable α and stable β modifications, features distinct crystal structures and lattice parameters compared to $UO_2$ and $UH_2$. However, the broadening of diffraction lines, induced by a combination of microstrain and grain size limited down to several nanometers, along with the pronounced texture often observed in samples deposited on amorphous fused silica substrates [33,125], imposes limitations on the capabilities of the XRD method in these studies. The overlap of several strong peaks adds to the uncertainty.

Nevertheless, magnetization and resistivity measurements can bring additional information about the phase composition. Due to different Curie temperatures of $UH_2$ (120 K) and $UH_3$ (around 165 K), these two phases are easily identified from $M(T)$ and $\rho(T)$ curves.

### *3.3.1. The effect of deposition parameters and substrate type on phase composition of thin films*

After the discovery of uranium dihydride existing in a thin film form [5], the urge to identify the combination of deposition conditions that stimulate stabilization of either $UH_2$ or $UH_3$ has appeared. During these studies three main parameters were chosen: substrate type and temperature and target current (or the deposition rate). A list of substrates included fused silica $SiO_2$ as a basic substrate for polycrystalline samples, single-crystalline Si with (100) orientation, MgO (100) ($a$ = 4.21 Å), $CaF_2$ (001) ($a$ = 5.462 Å). Substrates were cooled either by air to room temperature or by liquid nitrogen to 100-170K, or self-heated by plasma to 350K. Heating of the substrate to 500 K needed for single-crystalline film preparation is not suitable in this case, as hydride in a thin film form decomposes completely above 350 K.

#### 3.3.1.1. Deposition on amorphous $SiO_2$ (fused silica, quartz glass) substrates

Fig. 3.19 depicts GIXRD patterns of selected (uncapped) samples deposited on $SiO_2$ substrates at room temperature (gas cooling of the substrate) using different deposition currents (see Attachment A.1).

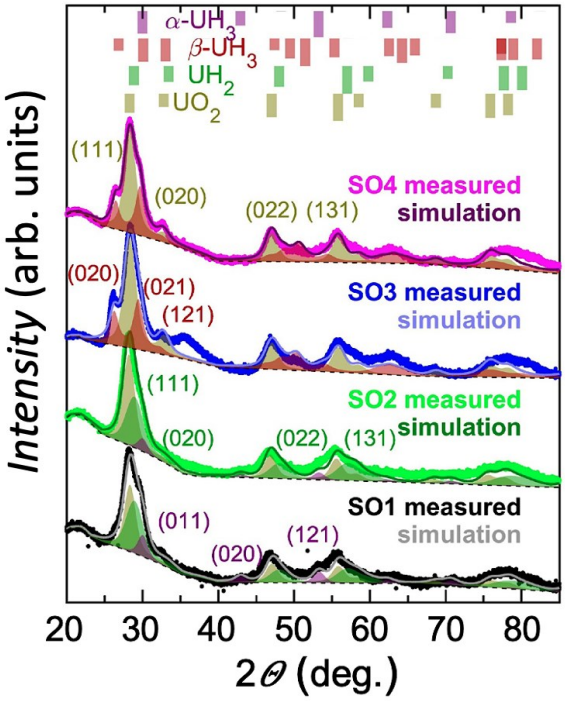


Fig. 3.19 GIXRD patterns of the uncapped U-H films deposited on air-cooled to room temperature $SiO_2$ substrates, an angle of incidence of a primary beam was $\alpha_i = 1.5°$. The XRD patterns of the phases $UO_2$, β-$UH_3$ and α-$UH_3$ were simulated using bulk lattice parameters. The lattice parameter from Ref. [5] was used for $UH_2$ spectrum simulation. Colored bars at the top of the figure represent the positions of Bragg reflections for each phase. Figure adopted from [142].

It was revealed that varying the target current while depositing on an air-cooled substrate (and keeping other parameters constant) allows to change the U-H ratio in the deposited film. The target current determines then deposition rate and to some extent also the deposition temperature. The deposition rate affects for how long time each deposited atom stays in the uppermost surface layer, in which the atoms are much more mobile and reactive than in the bulk. Higher deposition rates be expected to promote a phase with the highest thermodynamical stability, i.e. $UH_3$. If the concentration of $H_2$ in the sputter gas is reduced, one can expect rather a separation of

U and $UH_3$ phases. One has to consider different substrates, differing both in parameters as thermal conductivity and in crystal structure, which can be in some cases favorable for an epitaxial match of one particular U-T phase. In such multi-parameter convoluted processes it is on experiment to determine ranges of parameters promoting a particular phase. Here we observe that reducing the deposition current, enhances the presence of the $UH_2$ phase and suppresses the $UH_3$ phase. Intriguingly, in samples where the $UH_2$ phase is predominant (SO1 and SO2), the residual $UH_3$ phase is in the α-$UH_3$ modification. The estimated content of this phase does not exceed 10–20%. The β-$UH_3$ phase prevails in samples obtained using a higher deposition current (SO3 and SO4). Pure α-$UH_3$ film could not be obtained by any means.

Naturally, the value of the deposition current influences the thickness of the layers (see Fig. 3.20); a lower target current results in less material being deposited. Fig. 3.20 (a) presents only the thicknesses of the films, as analyzing individual $UH_x$ and $UO_2$ layers in the XRR data is not feasible due to their very similar densities (Fig. 3.20 (b)). In addition, oxygen penetrates the uncapped U-H layer unevenly after the sample is removed from the ultra-high vacuum conditions.

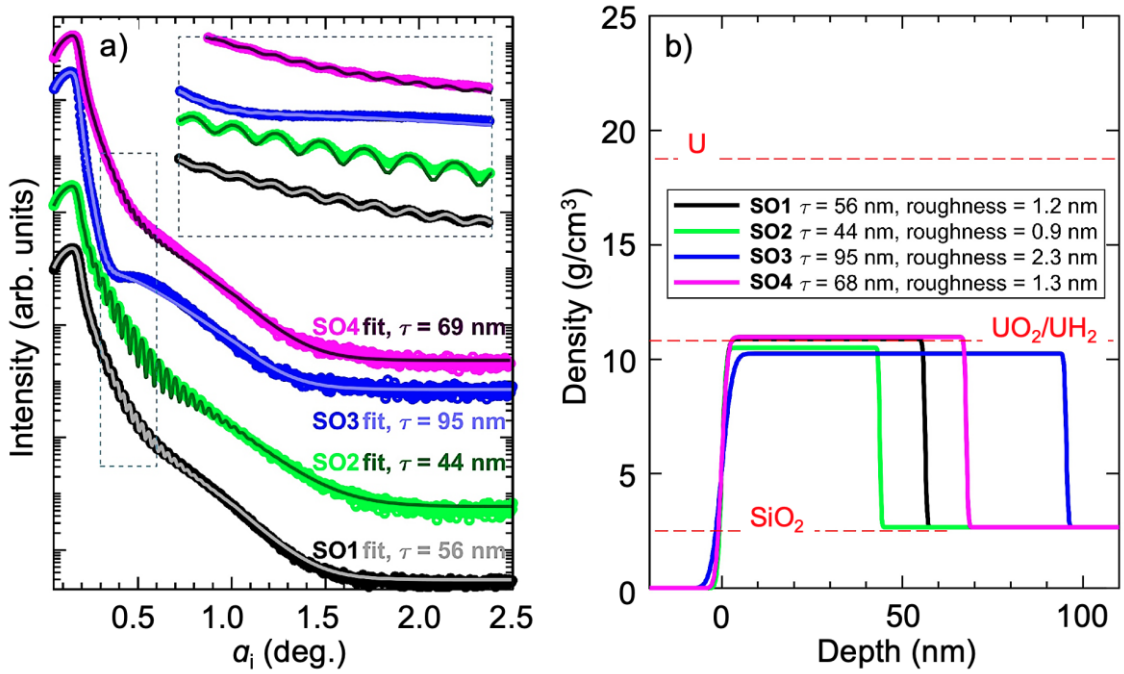


Fig. 3.20 X-ray reflectivity curves (a) and the density profiles (b) of the U-H films prepared with air cooling at room temperature on the $SiO_2$ substrates. Fits of the experimental data and calculated thicknesses $\tau$ are shown. The discernability of the fringes decreases with the thickness increase (in the inset), and they completely

disappear for the thickest sample SO3. Horizontal red dashed lines on the density profile indicate nominal densities for various species. Figure adopted from [142].

An additional complication in the phase analysis mentioned previously is the texture, which not only modulates individual intensity ratios, but as some peaks vanish completely, it reduces the number of peaks in XRD pattern. For β-$UH_3$, the texture typically manifests as the (00*l*) type, and it is most effectively observed in capped samples when interaction with air and moisture is minimized. Fig. 3.21 (a) depicts the GIXRD profiles of the Mo-capped $UH_3$ film (sample SO5 in Attachment A.1), measured at various angles of the incident beam $\alpha_i$, with the data acquired in the Bragg-Brentano geometry. In the Bragg-Brentano measurement, only the (002) and (004) peaks of β-$UH_3$ are observed, indeed indicating a pronounced (00*l*) texture in the SO5 sample. Pole figure measurements (Fig. 3.21 (b) and (c)) corroborate the (00*l*) texture, wherein the (00*l*) lattice planes are predominantly oriented parallel to the sample surface, while there exists a random orientation of crystallites within the sample plane.

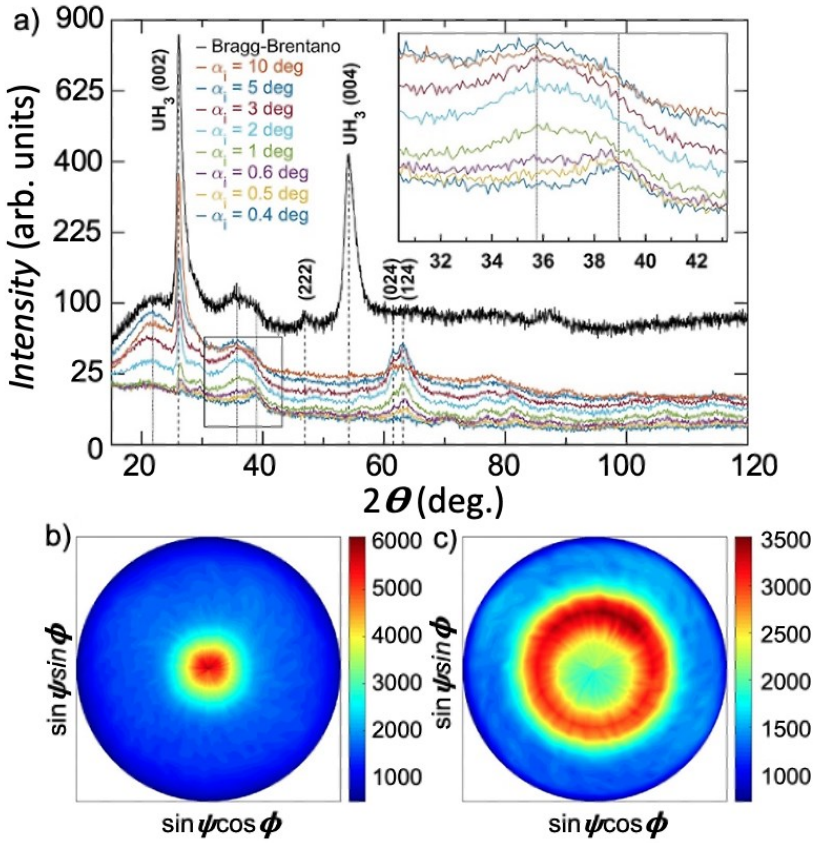


Fig. 3.21 (a) Comparison of the GIXRD patterns of Mo-capped β-$UH_3$ film (sample SO5) obtained with angle of incidence $\alpha_i$ = 0.4–10° in the Bragg-Brentano geometry.

The inset shows an enlarged area around spurious peaks at 35.8° and 38.8°, which can be associated with a small amount of non-hydrogenated U or U-Mo. (b) Experimental (002) and (c) (210) pole figures of the β-$UH_3$ thin film sample.

Typically for these studies, there is a considerable compressive residual stress in the films. In the case of sample SO5, the out-of-plane parameter is $a$ = 6.83 Å, the in-plane parameter is $a$ = 6.64 Å, and the determined stress-free lattice parameter $a$ = 6.816(3) Å is notably higher than that of bulk β-$UH_3$, $a$ = 6.644 Å [143]. This significant compressive strain[4], quite typical for sputter deposited films, tends to inhibit corrosion in the presence of air by impeding the formation of cracks that could facilitate the propagation of oxidation into the bulk of the film. Consequently, the body of the films retains its metallic character over an extended period, spanning years. Worth mentioning, Zr was not the best choice for capping material as Zr-capped samples fully oxidized in a period of months (due to low electronegativity of Zr).

The inset in Fig. 3.21 shows details of spurious peaks at 35.8° and 38.8° (these peaks are visible in the XRD profiles obtained in the parallel beam geometry of some of the uncapped or capped samples). Analysis of $\alpha_i$-scans revealed that they are most probably related to the two different phases. One of the phases is located close to the sample surface (≈ 3–28 nm) and is associated with the surface contamination of Mo or Mo-U phase with oxygen. The conclusion was made based on the strong variation of the peak at ~ 36 deg. with the angle of incidence, i.e. depth. The other phase related to peak at 38.8 deg. is distributed in the "body" of the film between 6 to several hundred nm and can be associated with a small amount of non-hydrogenated U due to the slightly higher density of a sample compared to $UH_3$ (densities of bulk U metal and β-$UH_3$ are 19.07 g/cm$^3$ and 10.91 g/cm$^3$, density of thin $UH_2$ film was fitted as 10.41 g/cm$^3$).

In samples prepared on a $SiO_2$ substrate without air cooling (plasma-heated to ≈ 350 K during deposition), the $UH_2$ phase is the prevailing one, regardless of the deposition current (Fig. 3.22, bottom). Cooling by liquid nitrogen works in a similar way; only the grain size is affected. Fig. 3.22 compares the XRD patterns of the $UH_2$ samples on $SiO_2$ substrates obtained at temperatures 170 K (top) and 350 K (bottom).

[4] One of the models used for the description of compressive stress in thin films incorporates the flow of atoms into the grain boundary, in which the driving force is an increase in the surface chemical potential caused by the deposition of atoms. Addition of atoms to the grain boundary results in compressive stress [162].

Crystallites of $UH_2$ deposited at low temperatures measure 16 nm (Fig. 3.22, top), while the mean crystallite size surprisingly diminishes to 3–4 nm in films deposited at 350 K (Fig. 3.22, bottom). Full profile refinement using the MStruct program [101] affirms the cubic *fcc* structure in the $UH_2$ sample prepared at $T = 170$ K (SO6), with a lattice parameter $a = 5.3317 \pm 0.0007$ Å. The film exhibits a significant compressive residual stress of $\sigma = -1.31 \pm 0.05$ GPa, calculated using the elastic constants of $UH_2$ from Ref. [144].

We can assume that the higher $H_2$ pressure in the working gas could have helped with stabilization of $UH_3$ phase, as higher temperature affects the mobility of H atoms in the structure (some escape, and total amount of hydrogen is lower). The reason why films prepared without cooling do not show two-phase composition ($UH_3$ and non-hydrogenated phase) lies in the higher mobility of atoms as well, which supports homogenization of the sample.

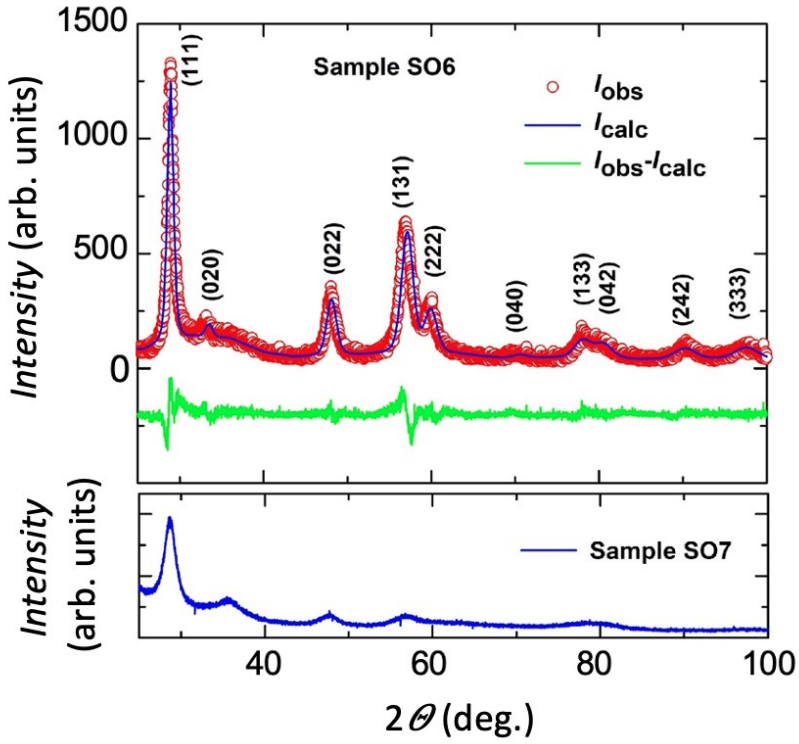


Fig. 3.22 GIXRD pattern of the $UH_2$ thin films on $SiO_2$ substrate obtained with an angle of incidence of the primary beam $\alpha_i = 1.5°$. Top: sample prepared at 170 K (SO6). Bottom: a self-heated to 350 K sample (SO7).

### 3.3.1.2. Other types of substrates

By using suitable substrates, the formation of the $UH_2$ phase can be supported irrespective of temperature. For example, silicon (Si) possesses a cubic structure with a lattice parameter $a$ = 5.431 Å, closely matching that of $NpH_2$ (5.343 Å) and $PuH_2$ (5.359 Å) [145,146]. Fig. 3.23 contrasts the XRD diffraction patterns of $UH_2$ films on Si (100) substrates obtained at room temperature and below. $UH_2$ with a mean crystallite size reaching almost 100 nm is achieved using a Si substrate at 173 K [5], while the grain size drops below 10 nm in samples produced at lower temperatures or at room temperature. Samples deposited on Si substrates exhibit a lattice parameter $a = 5.355 \pm 0.005$ Å. For the $CaF_2$ substrate temperature is important, higher deposition T gives $UH_2$ (SC14), cooling facilitates stabilization of β-$UH_3$ (SC15-16).

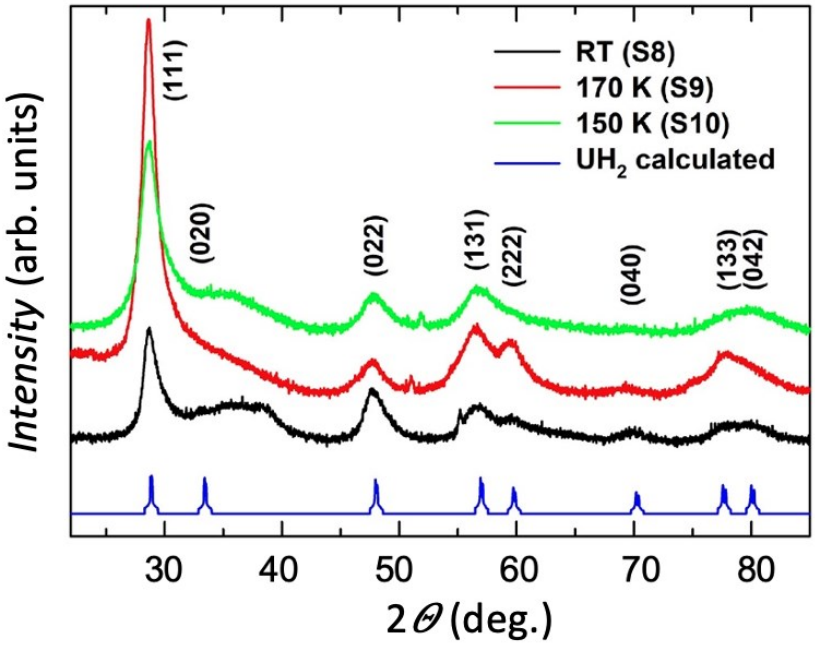


Fig. 3.23 GIXRD patterns of the Mo-capped U-H films deposited at different temperatures using a Si substrate, an angle of incidence of a primary beam $\alpha_i = 1.5°$. The pattern of $UH_2$ was calculated using the lattice parameter taken from Ref. [5].

Further step was to try to stabilize pure α-$UH_3$. MgO substate with lattice parameter $a$ = 4.21 Å, close to that of α-$UH_3$ ($a$ = 4.16 Å), was chosen. MgO substrate, however, worked similarly to $SiO_2$ in stabilization of β-$UH_3$ phase. In particular, the higher the target current – the higher the content of β-$UH_3$ in a sample (SM11-SM13 in Attachment A1). Temperatures of substrates, nevertheless, were close to 170 K. α-$UH_3$ was found only as a residual phase in samples with prevailing $UH_2$ phase.

There are too many variables which define the final result. In particular, an interplay of kinetic and thermodynamic processes, amorphization at low *T*, and decomposition of hydrides at high T on the other side prevent from the determination of exact deposition conditions for stabilization of pure hydride phases in the samples. The extend of these studies allows only to indicate which situations (higher/lower deposition rates, or temperatures, substrate type) are more favorable for obtaining each phase.

### *3.3.2. TEM study of the $UH_2$ film*

To characterize the microstructure of the $UH_2$ thin film sample and perform elemental mapping, a TEM study of the film cross-section was conducted. Fig. 3.24 depicts an overview of the $UH_2$ film on the $SiO_2$ substrate (labelled as sample SO6). The line profile in Fig. 3.24 (a) clearly indicates the position of the Pt protection overlayer (prevents excessive damage to the surface during lamella fabrication), the Mo cap and buffer, and the uranium-containing slab. The entire thickness of the film, where the lamella was extracted, is approximately 215 nm. Both the Mo buffer and cap exhibit similar thicknesses, approximately 9 nm each, as highlighted by dashed rectangles in Fig. 3.24 (a).

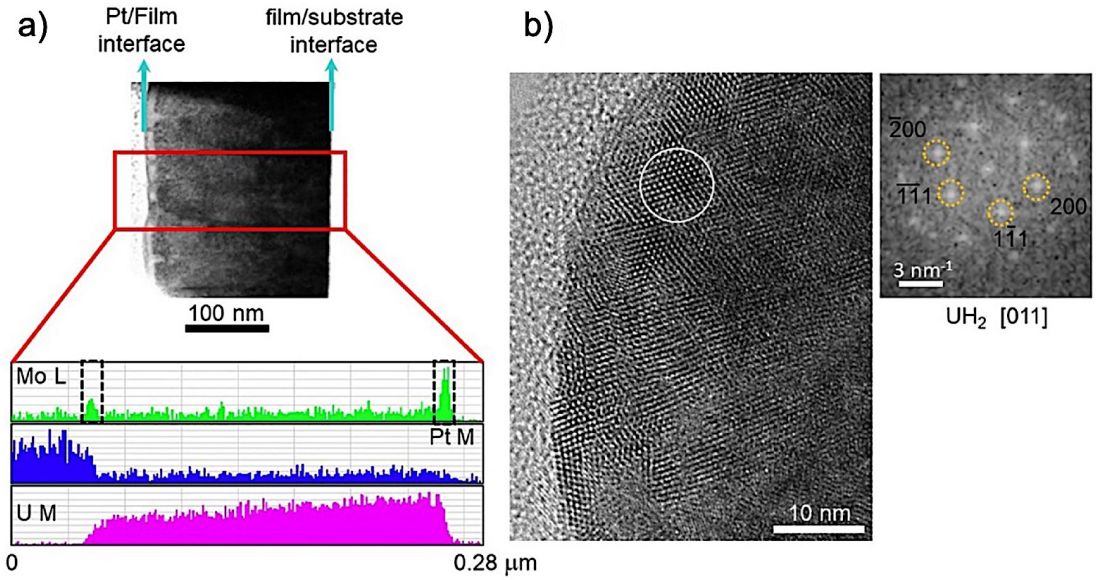


Fig. 3.24 (a) TEM analysis of the $UH_2$ thin film: line profile showing different elements, (b) HRTEM image of the thin film showing the FFT analysis of one grain in the [011] zone axis (Adopted from [142]).

Following FIB preparation, the lamella was transferred to TEM in air, inevitably resulting in oxygen contamination of the surface. Mapping (not displayed here) conducted in scanning TEM mode reveals some concentration of oxygen. However, through EDX (Energy-Dispersive X-Ray) and FFT analyses, we can rule out $UO_2$ as the dominant phase in the lamella. Consequently, we assume the presence of U hydride as the principal phase.

Analyzing various regions using the Fast Fourier Transform (FFT) method suggests the $CaF_2$ structure type of $UH_2$ in sample SO6. Fig. 3.24 (b) illustrates an instance of hydride identification using the FFT pattern. In this case, the pattern generated from the region highlighted by white circles in the image corresponds to the [011] axis. When grains are oriented in this manner, the {200} and {111} family planes align parallel to the *z*-axis, as depicted in the FFT image. The unit cell parameter of the structure, calculated from the *d*-spacing using multiple FFT patterns, is approximately 5.43 Å. This aligns with the unit cell parameter reported for $UH_2$ in the literature (≈ 5.36 Å [5]) and concurs with our XRD study. The determination of grain size indicates 8 nm in average. This compares with the XRD pattern refinement, which yields a grain size of 16 nm for this sample. The grains exhibit a roughly equiaxial shape.

### *3.3.3. Magnetic properties*

Bulk magnetization measurements are particularly useful for phase composition determination or surface oxidation in thin films due to the diverse characteristic types of magnetic behavior of all the phases involved. For ferromagnetic phases, the Curie temperatures $T_C$ were determined as the mean value between the inflection point in the low field $M(T)$ dependence and the intersection point of the tangent (i.e. extrapolation of the highest slope) with the baseline for the two U hydrides. Those are 120 K and 173 K for $UH_2$ and $UH_3$, their respective individual increments of magnetization are distinguishable (for example, in Fig. 3.25 (b)). However, this method does not work for the discrimination of α-$UH_3$ and β-$UH_3$ phases, as previous studies on bulk species [28] revealed that trihydrides have similar Curie temperatures. Nevertheless, there is still a question of whether stabilization of the transient α-$UH_3$ phase in a thin film form will alter the transition temperature.

Fig. 3.25 presents a comparison of zero-field cooling (ZFC) and field-cooling (FC) magnetization curves measured in a 0.05 T magnetic field applied along the sample surface for various samples. The bulk magnetization of the films is inherently influenced by the diamagnetic susceptibility of the massive substrates. At fields as low as 0.05 T, the data directly reflect the magnetization, with a minimal contribution from the diamagnetic substrate. It is evident that all samples exhibit ferromagnetic behavior.

As indicated by XRD, samples SO1 and SO2 (Fig. 3.25 (a) and (b)), deposited using the lowest current of 0.7–1 mA, contain both $UH_2$ and $UH_3$ phases, while an increase in current to 2.2 mA (Fig. 3.25 (c)) promotes the formation of the $UH_3$ phase. The collected magnetization data corroborate the XRD analysis conclusion that, aside from using lower currents, one pathway to the $UH_2$ phase involves allowing for mild heating of the substrate (sample SO7, Fig. 3.25 (e)). An alternative approach is to utilize a Si wafer as the substrate (sample S9, Fig. 3.25 (f)). The small feature in $M(T)$ in the vicinity of the Néel temperature of $UO_2$ ($T_N = 31$ K [147]) is attributed to the contamination of the uncapped samples with oxygen.

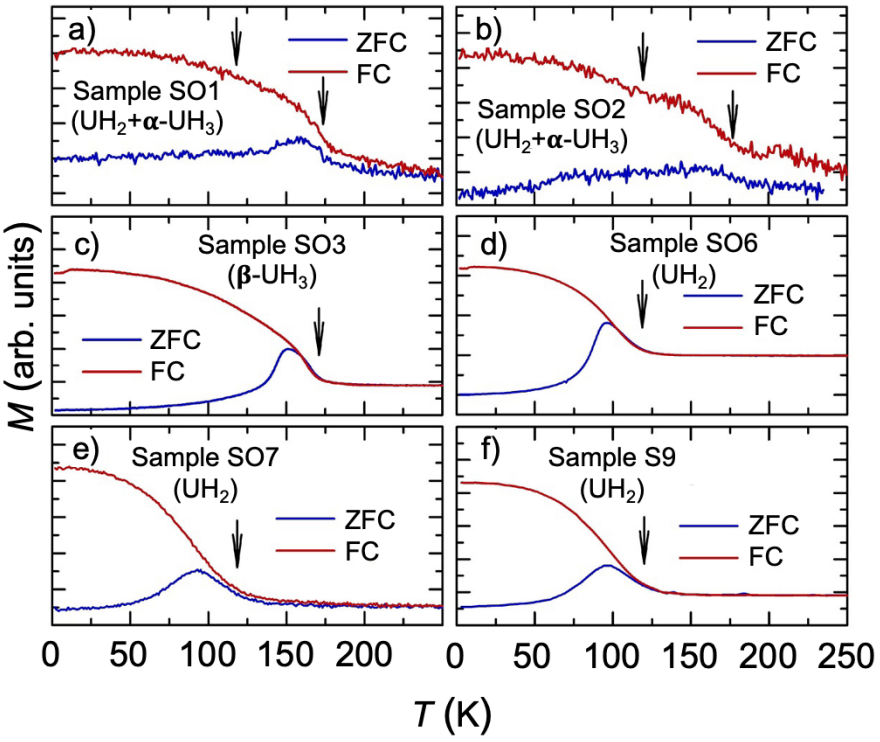


Fig. 3.25 Temperature dependencies of magnetization of the $UH_2$ and $UH_3$ films deposited on various substrates and measured in the field of 0.05 T applied along the sample surface. Arrows indicate ordering temperatures of phases. ZFC and FC refer to the zero-field-cooled and field-cooled measuring modes (Adopted from [142]).

Interestingly, there is no clear distinction in the Curie temperatures of the α-$UH_3$ and β-$UH_3$ phases, where $T_C$ = 170 ± 5 K. The difference in the ZFC and FC data branches reflects magnetic history phenomena, influenced by hysteresis. The behavior of the ZFC branch in Fig. 3.25 indicates that in such low magnetic fields heating almost up to the Curie temperature is required to magnetize the sample. These significant hysteresis values result from a strong magnetic anisotropy, originating in sizable orbital moments inherent to U-based materials. Indeed, all $UH_2$ and $UH_3$ samples exhibit wide magnetic hysteresis loops at low temperatures (refer to Fig. 3.26). The hysteresis width diminishes with an increase in temperature. The bifurcation of the ZFC and FC branches near $T_C$ in samples containing α-$UH_3$ can be linked to its stronger magnetic anisotropy compared to β-$UH_3$, a characteristic also reflected in the slower decrease of coercivity with temperature.

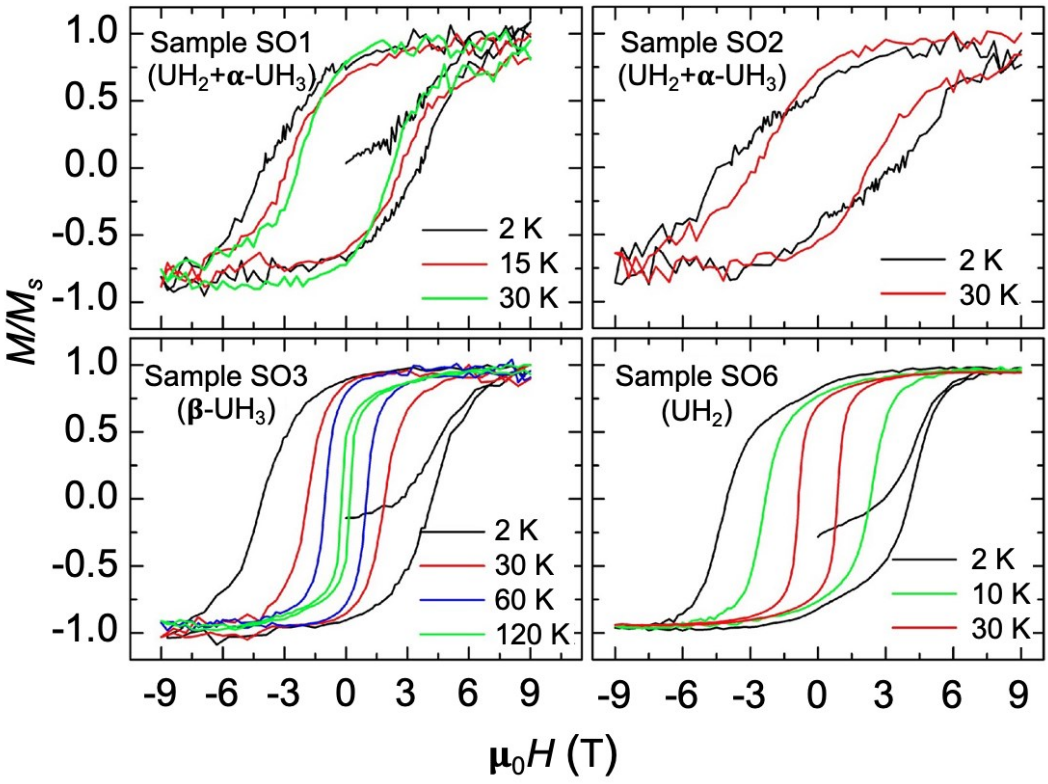


Fig. 3.26 Magnetization curves of $UH_2$ and $UH_3$ samples taken at various temperatures. The noisy loops correspond to the thinnest films (Adopted from [142]).

Without precise knowledge of the U amount in the examined films, determining the size of U moments is challenging; hence magnetization is provided in arbitrary units only. An estimate based on the film area and approximate thickness of $UH_2$ yields an order of magnitude of ≈ 0.5 $\mu_B$/U ($UH_3$ has ≈1 $\mu_B$/U [148]). *Ab initio* calculations

predict a total moment of 0.89 $\mu_B$/U [144]. For the majority of samples, the available 9 T field is insufficient to magnetize the sample up to saturation, and we remain the regime of a minor magnetization loop.

As previously highlighted [149], a disorder or very small grain size generally results in a decrease in the ordering temperatures of U compounds. However, the U hydrides examined in this study appear remarkably insensitive to such effects, likely due to the significance of the local U-H bonds. Additionally, the nearly identical Curie temperatures observed in various samples obtained under different conditions affirm the insensitivity of U-H magnetism to defects and strains.

### *3.3.4. Transport properties*

We explored the influence of atomic and magnetic disorder on the electrical properties of the hydride films. These films (both $UH_2$ and $UH_3$) have $\rho(T)$ reminiscent of the bulk $UH_3$ (Fig. 3.27) with "modified structure", i.e., with a disorder caused by transition metal alloying ($T$ substitutes U atoms) and small grain size [136] which was studied previously.

Bulk pure hydride β-$UH_3$ has the temperature dependence of resistivity quite conventional for a ferromagnet, with a high spin-disorder scattering in the paramagnetic state and thus, high absolute values above 600 μΩcm. Such a value indicate that it is in sort of intermediate state between metal and semi-metal, meaning a low density of electronic states with light effective masses. At a qualitative level, such situation can be associated with the 6*d* and 7*s* states largely removed from the Fermi level by hybridization with the H-1*s* states. $\rho(T)$ fast decreases below $T_C$ [28] and reaches saturation in the low-$T$ region. Bulk Mo (and other T substitutions) alloyed β-$UH_3$ has $\rho(T)$ combining the overall *negative* TCR of U-Mo alloys with the resistivity of β-$UH_3$ [136]. Consequently, its resistivity exhibits a small but sharp cusp at $T_C$ and non-monotonous development below the transition. As the continuing negative slope in the ferromagnetic state is strongly affected by the applied magnetic field, it can be associated with a static magnetic randomness, originating due to a very small grain size of 2-3 nm, bringing the system into the regime of weak localization with prominent quantum effects [136,150]. Just below $T_C$, the correlation length between individual magnetic moments is short, but it increases with decreasing $T$. Proceeding to lower temperatures the magnetic excitations start disappearing and

magnetic anisotropy manifests more, dominating over exchange interactions (compare hysteresis loops taken at different temperatures). Magnetizations in individual neighbor nanocrystals become gradually misoriented. This tendency continues down to the lowest temperatures, which explains the absence of saturation seen for the precursor alloys. Applying a magnetic field suppresses both magnetic excitations in the ferromagnetic state and the misorientation of magnetization in individual nanograins, which results in lower resistivity. The decrease of resistivity should be the most visible in the intermediate temperature range, below $T_C$ but not close to the 0 K limit, as the manipulation with the moments at very low temperatures is weakened by increasing anisotropy.

Comparing hydride films and bulk hydrides with substitution, the overall behavior and the absolute values close to 1000 μΩcm are very similar. The cusp is, however, less sharp. For the $UH_2$ films (Fig. 3.27 (b)), the $T_C$ anomaly is even less pronounced than for $UH_3$.

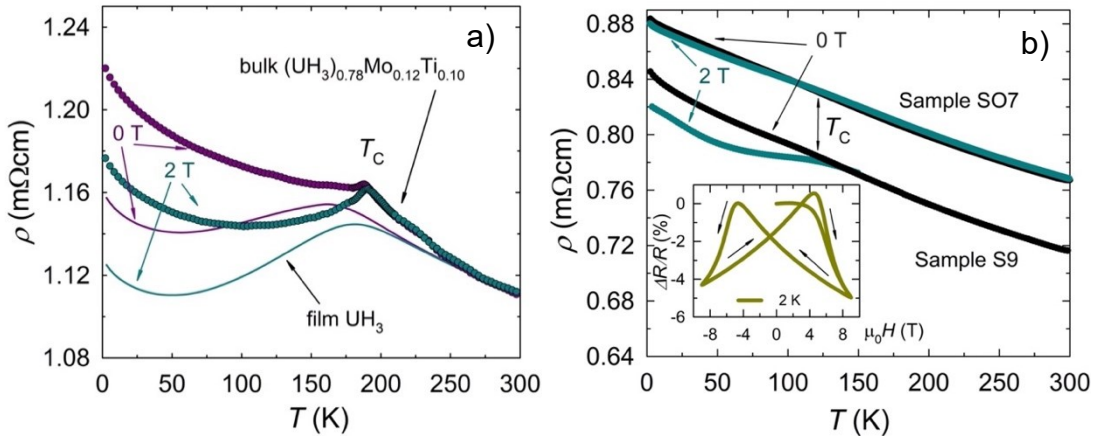


Fig. 3.27 Comparison of the temperature dependence of electrical resistivity, $\rho(T)$, of the $UH_3$ thin film (sample SO3) with bulk $(UH_3)_{0.78}Mo_{0.12}Ti_{0.10}$ (a) and comparison of electrical resistivity $\rho(T)$ curves of the $UH_2$ thin film samples grown on a Si substrate (sample S9) and on $SiO_2$ (self-heated sample SO7) (b). The dark cyan lines are the data in a magnetic field of 2 T. The inset shows the magnetoresistivity at $T = 2$ K for the sample S9. (As the resistance of Si at temperatures below room temperature is considerably higher, it does not qualitatively impact the data and anomalies related to magnetic ordering of $UH_2$. The absolute resistivity values obtained on both insulating and semiconducting substrates are similar in magnitude.). Data for bulk $(UH_3)_{0.78}Mo_{0.12}Ti_{0.10}$ adopted from Ref. [136].

The films without T metal component must have different source of disorder. Besides the small grain size, there may be certain randomness in the occupation of the H sites. Similar to the bulks, the external magnetic field weakens the static magnetic disorder below $T_C$, which makes the onset of ferromagnetism more visible. However, for $UH_2$ films, TCR remains high and negative even below $T_C$, which makes the resistivity increment on cooling from $T = 300$ K reach 17%, i.e., more than double compared to the $UH_3$ film, in which the magnetic order visibly reduces the increment below the transition. The $T_C$ values agree with the magnetization data.

The grain size impacts the shape of the resistivity curve in the studied hydrides. The larger the crystallites, the sharper the anomaly associated with the ordering temperature $T_C$ (see Fig. 3.27 (b), where sample S9 has a grain size of 100 nm, whereas S07 is on the verge of amorphization with 3-4 nm crystallites).

### *3.4. Structure and physical properties of U-T-H thin films*

As mentioned previously, it was revealed during bulk studies that the substitution of uranium with transition metal (up to 15 at.%) in hydride increases the transition temperature. The most spectacular effect was seen in Mo case, which was the first substitution tried in thin films. The second set of samples was prepared with Zr metal in an attempt to stabilize α-$UH_3$ in thin film form. In the previous section, the electronic structure of the mentioned hydrides was tested by means of XPS and UPS. In this section, the influence of substitution is discussed in terms of changes in crystal structure and physical properties.

#### *3.4.1. Structure of hydrides with substitution*

The XRD structure analysis for two samples, with 9 at.% and 15 at.% of molybdenum are presented below. The XRR data for the film $(UH_3)_{0.91}Mo_{0.09}$ on $SiO_2$ substrate cooled to 100 K (not presented here) revealed that the investigated hydride has an approximate thickness of 210 nm and is enveloped by 18 nm-thick buffer and capping Mo layers. The XRD pattern in Fig. 3.28 indicates the β-$UH_3$ structure with a (00*l*) texture type, similar to pure $UH_3$ films from these studies. The inset in Fig. 3.28 displays pole figures confirming the identified texture. The high number of reflections and absence of spurious phases allowed for a full profile refinement using the Rietveld method. The film exhibits a compressive residual stress of -5.1 ± 0.1 GPa. The refined

stress-free lattice parameter, $a = 6.703 \pm 0.004$ Å. The character of the diffraction pattern, featuring broad diffraction peaks and sharp features on the top, can be described as a bimodal structure. It comprises a majority of large grains, with a mean crystallite size of about 200 nm, constituting 60% of the sample volume. Additionally, numerous small grains are present, with a mean size of coherently diffracting domains measuring 3.6 nm.

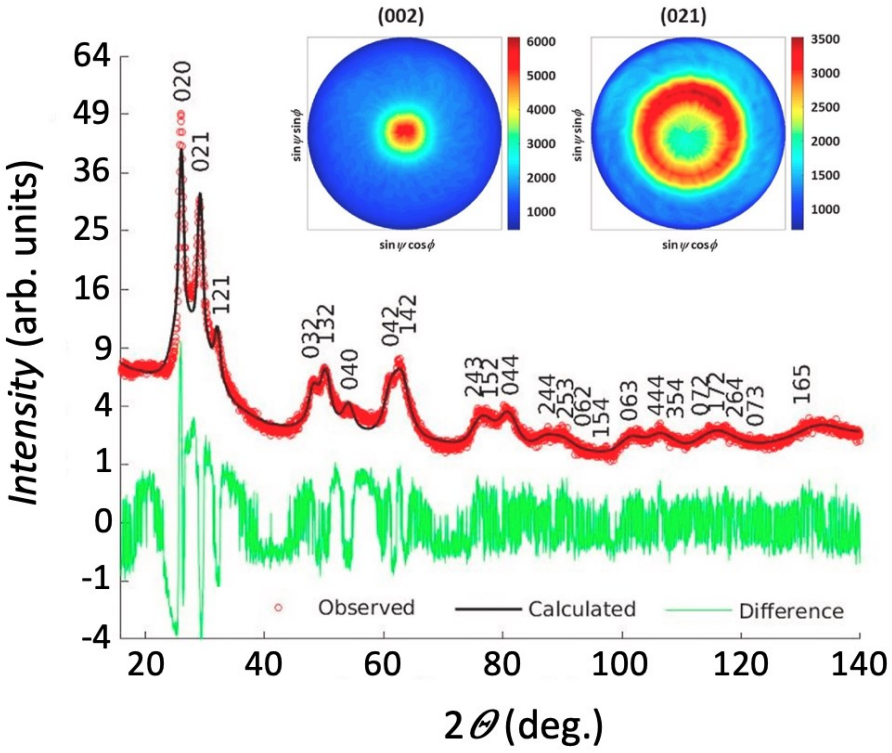


Fig. 3.28 XRD pattern of $(UH_3)_{0.91}Mo_{0.09}$ film measured in the parallel beam geometry at the incidence angle $\alpha_i = 1°$ (red circles) and the fit using program MStruct [29] (black line). The green line is the difference curve. Inset shows pole figures for $(UH_3)_{0.91}Mo_{0.09}$ based on the reflections (002) and (021).

The XRD pattern of the film $(UH_3)_{0.85}Mo_{0.15}$, deposited on a $SiO_2$ substrate cooled to $T = 100$ K (Fig. 3.29), displays significant broadening, suggesting a reduction of grain size to 1.5 nm. Consequently, the material can be considered close to the threshold of amorphization. Nevertheless, the lattice parameter, $a \approx 6.73$ Å, could be determined. The grain size is even smaller than that of the hydride $(UH_3)_{0.85}Mo_{0.15}$ synthesized by the hydrogenation of splat-cooled U–Mo alloy. The lattice parameter of bulk $(UH_3)_{0.85}Mo_{0.15}$ was found to be 6.67 Å [151]. In all the presented cases of thin films, we observe a higher value of the lattice parameter than expected from comparisons with bulk systems. Besides the effects of the sputter

deposition, the reason for this likely lies in the fact that the lattice structure of films is modulated by stress from the substrate.

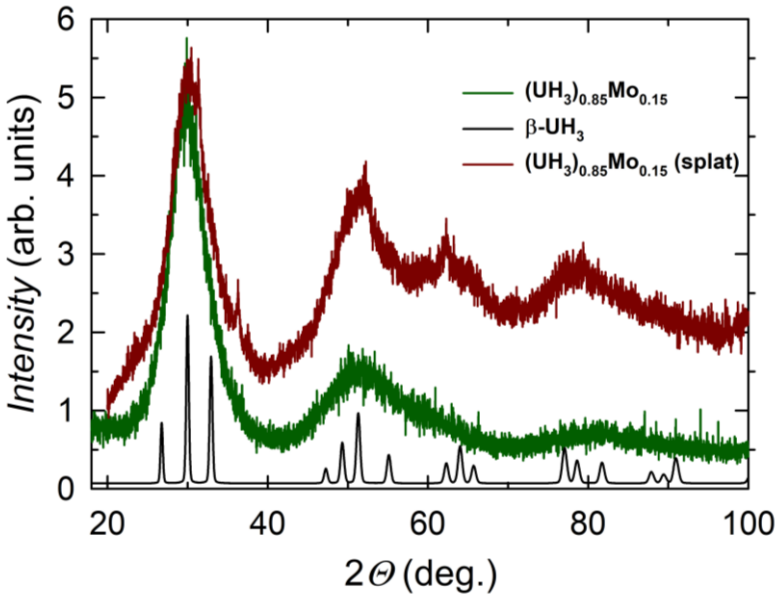


Fig. 3.29 XRD pattern of the $(UH_3)_{0.85}Mo_{0.15}$ film (dark green) and comparison with splat bulk $(UH_3)_{0.85}Mo_{0.15}$ (dark red) and a simulated pattern of β-$UH_3$ (black).

Only the primary analysis of structures for U-Zr-H films was performed. Unfortunately, one of the main reasons for preparation of Zr alloyed hydride films, that is an attempt to stabilize single-phase films of α-$UH_3$, has not been fulfilled. α-$UH_3$ was not observed in any of specimen. However, $UH_2$ structure was stabilized, unlike in Mo-alloying case.

In addition to deposition parameters, which affect phase composition of pure hydride films, there are a few extra for hydride films with substitution. In particular, Zr concentration in prepared films and a complex parameter of total target current (from U and Zr targets), which includes the total amount of deposited material per second, the ratio of U to H in the plasma, and "the temperature" of sputter source. Moreover, the presence of Zr atoms in the hydride structure changes the thermodynamic equilibrium of the system.

We did not cover all the possible combinations of the deposition parameters, but there is sufficient number of samples for suggesting some guideline how to stabilize different phases in thin films (Fig. 3.30).

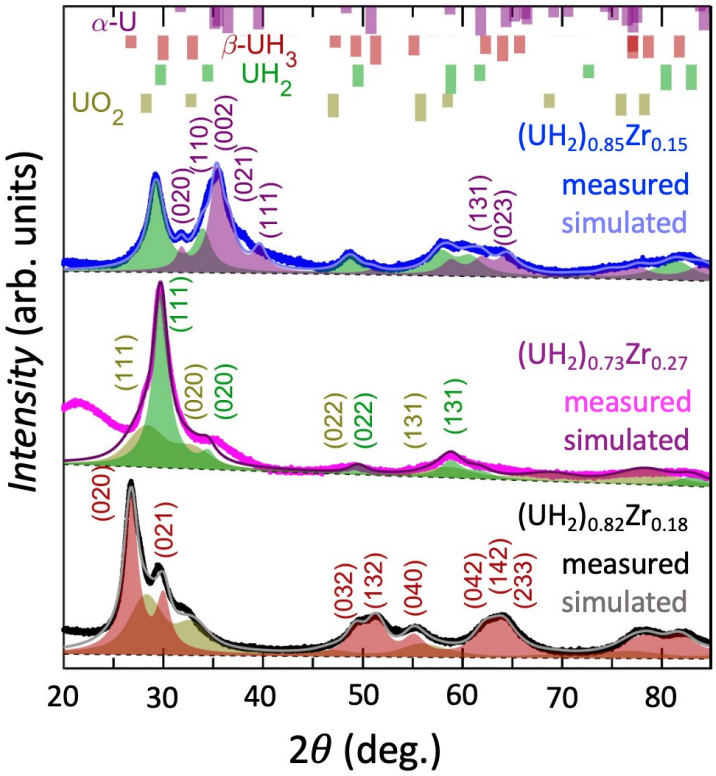


Fig. 3.30 GIXRD patterns of the selected U-Zr-H films. Samples with structure types of $UH_2$ ($(UH_2)_{0.73}Zr_{0.27}$, magenta color, deposited on $SiO_2$ substrate at RT), β-$UH_3$ ($(UH_3)_{0.82}Zr_{0.18}$, black) and mixed phases of $UH_2$ and α-U ($(UH_2)_{0.85}Zr_{0.15}$, blue) are presented. The last two are prepared with LN substrate cooling on Si with buffer/capping layers of Zr. An angle of incidence of a primary beam was $\alpha_i = 1.5°$ for the first pattern and 5° for the rest. The XRD patterns of the phases $UO_2$, β-$UH_3$ and α-U were simulated using bulk lattice parameters. Colored bars at the top of the figure represent the positions of Bragg reflections for each phase.

For the films deposited on $SiO_2$ with similar Zr concentrations, temperature is a decisive parameter. At higher temperature (RT, cooling of substrate by air) $UH_2$ is formed, at lowest $T$ (100 K) β-$UH_3$ can be obtained, contrary to the situation with pure hydrides. Films prepared in the intermediate temperature range between those two points have a mixed phase composition (including $UH_2$, β-$UH_3$ and α-U in different combinations, visible both from XRD data and magnetization loops, see Fig. 3.32). Interestingly, $UH_2$ was stabilized at 100 K only when Zr concentration was high (close to 30 at.% Zr).

The tendencies with temperatures imply also for other substrates (Si, MgO), with exception of $CaF_2$ which facilitates growth of $UH_2$ phase at 100 K instead of β-$UH_3$.

The difference between β-$UH_3$ films deposited on different substrates lies in higher crystallinity (bigger grains) and stronger texture of those deposited on single-crystal substrates (MgO or Si) compared to hydrides obtained on $SiO_2$.

### *3.4.2. Magnetic properties of hydrides with T substitution*

Fig. 3.31 (a) displays variations of Curie temperatures for all the prepared thin films. Those were obtained from temperature dependence of magnetization in low fields, measured in the FC mode, in the same way as described for pure uranium hydride samples. It is known that alloying bulk hydrides with transition metals results in increasing transition temperatures, universally with a maximum approx. at 15 at.% of T concentration (Fig. 3.31 (b)). The most striking effect of alloying was found for Mo substitution with the highest $T_C$ = 203 K [151]. A qualitative model of the indirect influence of the T metal was proposed. The T element included in the structure of the hydride increases the effective H to U molar ratio. The requirement is for T-H bonds to be less polar than the U-H ones [148]. The significance of Mo is in its electronegativity practically coinciding with that of H. Hence if Mo dopants substitute U and H concentration does not decrease, the polar U-H bonding is concentrated onto the remaining U atoms. Zr with electronegativity similar to U behaves opposite. The situation of U should be then similar to U in pure $UH_3$. Indeed, $T_C$ increases in the Zr doped $UH_3$ bulk much less than for Mo. The fact that $T_C$ culminates around 12-15% of substituting metals irrespective of their type can be qualitatively understood as due to destabilization of H if U in the U4 tetrahedra (practically identical in α- and β-$UH_3$) hosting H atoms is replaced by Mo, Zr, or another T element. This destabilization, illustrated by ab-initio calculation for Mo [144], prohibits H atoms residing inside U2Mo2 tetrahedra, but even the U3Mo tetrahedra have H less bonded. Naturally, when not all H sites are occupied for higher T content, the positive influence of polar bonding vanishes rapidly. It seems that the substitution of the level 1/8 (i.e. 12.5 %) is the critical boundary behind which $T_C$ cannot increase any more.

As seen from Fig. 3.31, the substituted hydride films do not follow the initial decreasing trend of $T_C$. In both cases (Zr and Mo), the temperature of the ferromagnetic transition is barely dependent on the concentration of the alloying element (in particular, the initial increase of $T_C$ is absent).

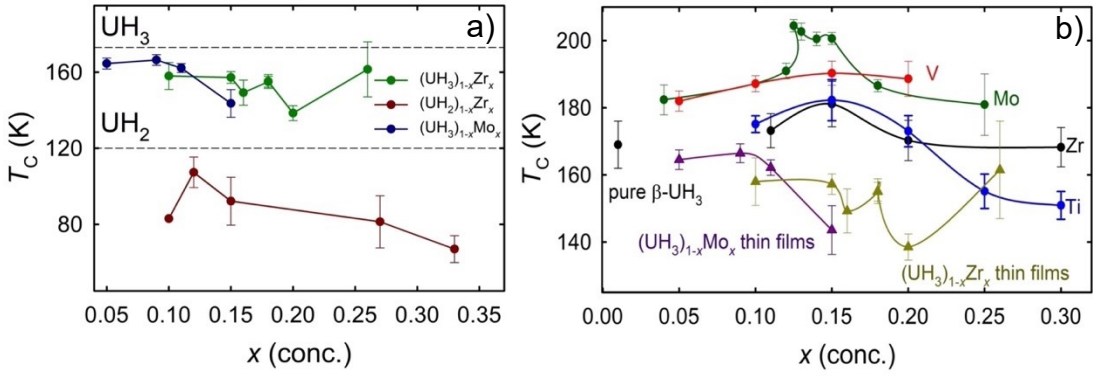


Fig. 3.31 (a) Concentration dependence of the Curie temperature in $(UH_3)_{1-x}Zr_x$, $(UH_2)_{1-x}Zr_x$ and $(UH_3)_{1-x}Mo_x$ thin films and (b) comparison of concentration dependences of thin films and bulk samples with various T-metal substitutions. Data for bulk samples were adopted from [148].

All three sets of films possess lower $T_C$ compared to not only bulk counterparts with the same concentrations of alloying elements but even to pure $UH_2$ or $UH_3$ samples. Considering the insensitivity of $T_C$ to grain size, defects and strains in pure hydride films, the reason for lowered values must be incomplete incorporation of H atoms into the hydride structure. As films are prepared in conditions far from thermodynamical equilibrium, excessive energy (kinetic energy of impinging ions at sputtering is of the order of eV) adds to the instability of H atoms in the structure of deposited samples with substitutions and randomness of H occupied positions, which results in lower $T_C$. The films $(UH_2)_{1-x}Zr_x$ are arguably different. One has to realize that the H concentration can be even more variable within the $CaF_2$ structure type, as shown found in dihydrides of lanthanides and transuranium actinides [152,153].

*Ab initio* calculations performed for U-T hydrides using large super-cells and testing H enthalpies of formation for T occupying various U sites proved indeed that a system embracing Mo substitution has less stable H positions than the Zr alloyed ones. In particular, the enthalpy of formation for the system with 1 Mo atom at *2a* position is -1.03 eV/f.u. (-0.99 eV/f.u. for *6c* position), whereas pure β-$UH_3$ and Zr-substituted structures have the same energy at -1.51 eV/f.u. (-1.32eV/f.u. for Zr *6c* position). These calculations explain the reason why, unlike pure hydride films and $(UH_3)_{1-x}Zr_x$, which can be deposited at room temperature, $(UH_3)_{1-x}Mo_x$ needed cooling for the hydride formation. As expected, an additional Mo alloying atom further destabilizes the structure (-0.64 eV/f.u.). More details will be published elsewhere.

A striking feature of ferromagnetism of uranium hydrides, namely very wide hysteresis loops, is inherent for hydrides with substitution, as well. The reason dwells in small monodomain grains and strong anisotropy increasing the field required for remagnetization. This fact is illustrated by the magnetic hysteresis loops (Fig. 3.32), reaching up to 8 T width at $T = 2$ K. Fig. 3.32 also covers shapes of magnetization curves for samples with different structures and alloying elements.

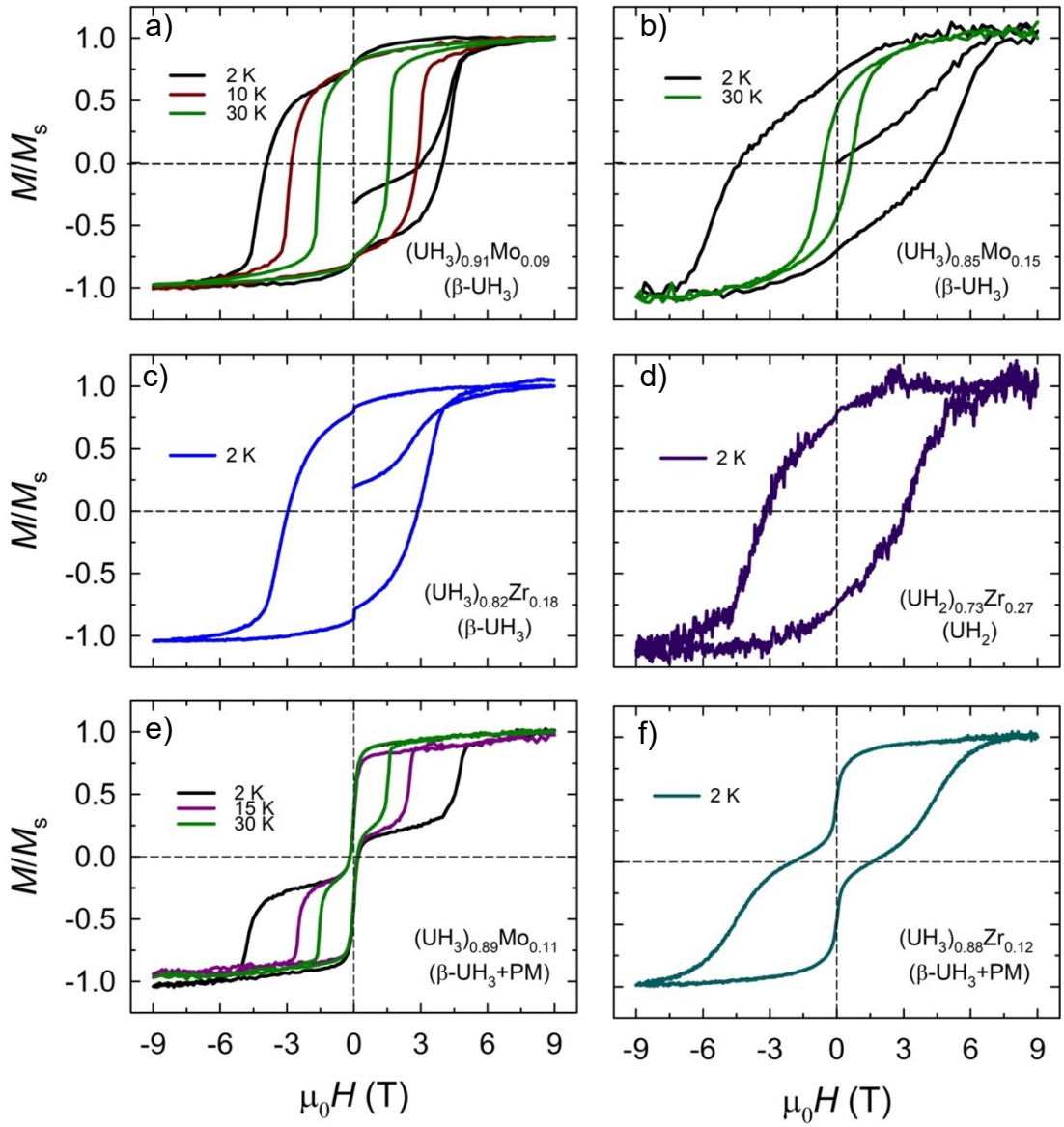


Fig. 3.32 Magnetization curves of selected alloyed hydride films. (a) and (b) depict β-$UH_3$ samples alloyed by Mo with different grain size (200 nm and 1.5 nm, respectively). (c) and (d) correspond to Zr-substituted samples with β-$UH_3$ (c) and $UH_2$ (d) structure. Wasp-waisted loops (e and f) belong to samples with paramagnetic phase (PM) inclusion.

Analogous to bulk hydrides with small grain size [148], thin films possess curves with slow saturation (the remagnetization step is smeared out, though). Comparing loops related to films with the same crystal structure (namely, β-$UH_3$) on Fig. 3.32 (a) and (b), the smaller the grains – the slower saturation. Curves for $UH_3$ (Fig. 3.32 (c)) and $UH_2$ (Fig. 3.32 (d)) with Zr are much alike. The dependence of coercive force on alloying concentration has not been studied. A specific "wasp waisted" shape of the loops with a drop at zero field (Fig. 3.32 (e) and (f)) points to coexistence of a ferromagnetic and paramagnetic (magnetically soft) phase. This gives rise to an exchange spring effect [154]. PM phase is expected to be non-hydrogenated alloy of the same nominal composition as hydride film [148]. The presence of PM phase can be deduced sometimes from XPS U-4*f* core-level lines, when the intensities are higher compared to fully hydrogenated films, or resistivity measurements. A sufficient amount of paramagnetic phase changes the shape of resistivity temperature dependence (it becomes field-independent without any cusp related to metamagnetic transition).

### *3.4.3. Resistivity of U-T Hydrides*

In the present work, electrical properties of the selected thin films are compared with $\rho(T)$ of various bulk and splat-cooled hydrides with the same substitutions studied previously. The temperature dependencies for samples with Mo and Zr prepared by various methods are depicted in Fig. 3.33 and Fig. 3.34, respectively.

Films of hydrides with Mo/Zr substitution are very much analogous to films of pure hydrides. Particularly, the resistivities $\rho(T)$ demonstrate weak dependence on temperature in the paramagnetic state with negative TCR and exceptionally high absolute values of $\rho(T)$ for a metallic system. The Zeeman energy of individual fluctuating moments is negligible compared to the thermal energy $k_B T$. The dynamical fluctuations are thus insensitive to the magnetic fields of several Tesla. Additionally, all the presented $\rho(T)$ dependences for the samples with $UH_3$ structure display a distinct cusp, which indicates the $T_C$.

In addition to the randomness of H-occupied positions (characteristic of pure hydride films), an upturn of $\rho(T)$ in the low-temperature limit can be ascribed to the strong random anisotropy due to Mo/Zr defects, surpassing the ferromagnetic exchange interactions, and randomizing local directions of U. The thin buffer and

capping Mo layer do not play any significant role in the thin films, as otherwise, $\rho(T)$ would exhibit a tendency to decrease at low temperatures.

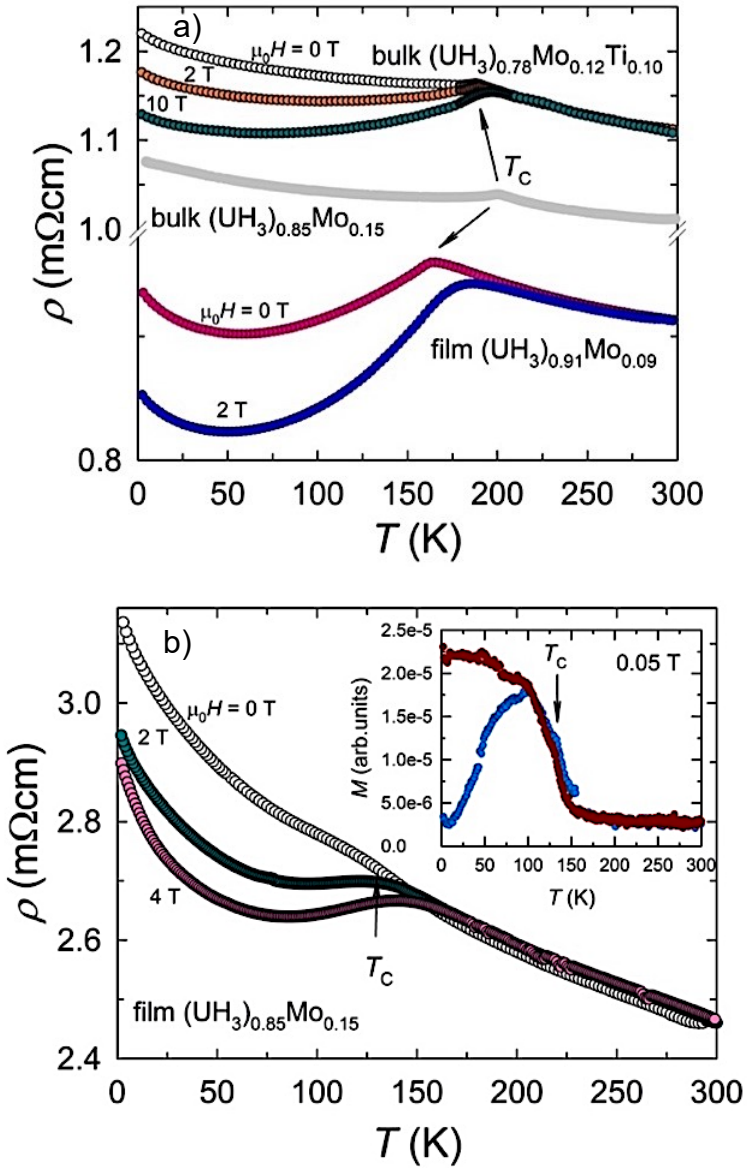


Fig. 3.33 (a) Temperature dependencies of electrical resistivity $\rho(T)$ of the $(UH_3)_{0.91}Mo_{0.09}$ film in magnetic fields 0 and 2 T compared with $\rho(T)$ of various bulk hydrides (adapted from Ref. [150]) and (b) $\rho(T)$ of the $(UH_3)_{0.85}Mo_{0.15}$ film in various fields. The field was applied along the film surface. Inset of figure (b) depicts FC and ZFC magnetization curves for $(UH_3)_{0.85}Mo_{0.15}$ sample. Arrows indicate Curie temperatures.

Fig. 3.33 (b) depicts the resistivity of $(UH_3)_{0.85}Mo_{0.15}$ which is on the verge of an amorphous state with 1.5 nm grain size. Curie temperature $T_C \approx 130$ K is manifested as a broad knee (145 K from magnetization data). Transition becomes more

visible in magnetic fields due to suppression of the magnetic part of the disorder in the ferromagnetic state. $\rho(T)$ has an even more pronounced negative slope in the whole temperature range than the materials discussed previously. It can be understood as a combination of the effect of stronger U–Mo mixing disorder and disturbed crystallinity. In any case, the shape proves that the Mo atoms do not segregate in an extra phase. The fact that Mo occupies the U sites in β-$UH_3$ was demonstrated previously by the Pair Distribution Function (PDF) analysis using high-energy X-rays [155]. Similar to pure hydride films, the magnetic transition is broadened compared to the film with a bigger grain size (sample with 8 at.% Mo, Fig. 3.33 (a)).

The case of Zr substitution is different. The shape of the resistivity temperature dependence of the films does not repeat that of the bulk sample (Fig. 3.34). It was revealed previously, that unlike other bulk hydrides with modified structure, the electrical resistivity of the bulk $(UH_3)_{0.80}Zr_{0.20}$ behaves as in a regular ferromagnet, with decreasing $\rho$ below $T_C$ due to a suppression of the spin disorder and a minor influence of applied magnetic field [28]. Only U hydrides with Zr substitution stabilize in α-$UH_3$ structure with slightly bigger crystallites (10 nm). That might explain the difference between the bulk and film samples, as the thin films have a β-$UH_3$ or $UH_2$ structure with smaller grains. $\rho(T)$ of $(UH_3)_{0.82}Zr_{0.18}$ (Fig. 3.34 (a)) is like other $UH_3$ hydride films studied, however, with smaller negative TCR in a paramagnetic state and clearly visible cusp at $T_C$ (155 K, the same from magnetization). The $(UH_2)_{0.85}Zr_{0.15}$ sample (Fig. 3.34 (b)) shows analogous shape of resistivity as $UH_2$ samples without T metal substitution with negative TCR within the whole temperature range. The cusp is almost indistinguishable, probably due to very fine crystallites. One has also to keep in mind that the dihydrides (of actinides or rare earths), crystallizing in the $CaF_2$ structure type, have in fact a variable $RT_{2+x}$ stoichiometry, with $x$ reaching up to 0.75 [12,156], corresponding to additional type of stochastically occupied H positions. Hence additional type of disorder can be considered functioning in the U dihydrides. Interestingly, MR in the film with $UH_2$ structure is 10 times smaller than in film with $UH_3$ crystal structure.

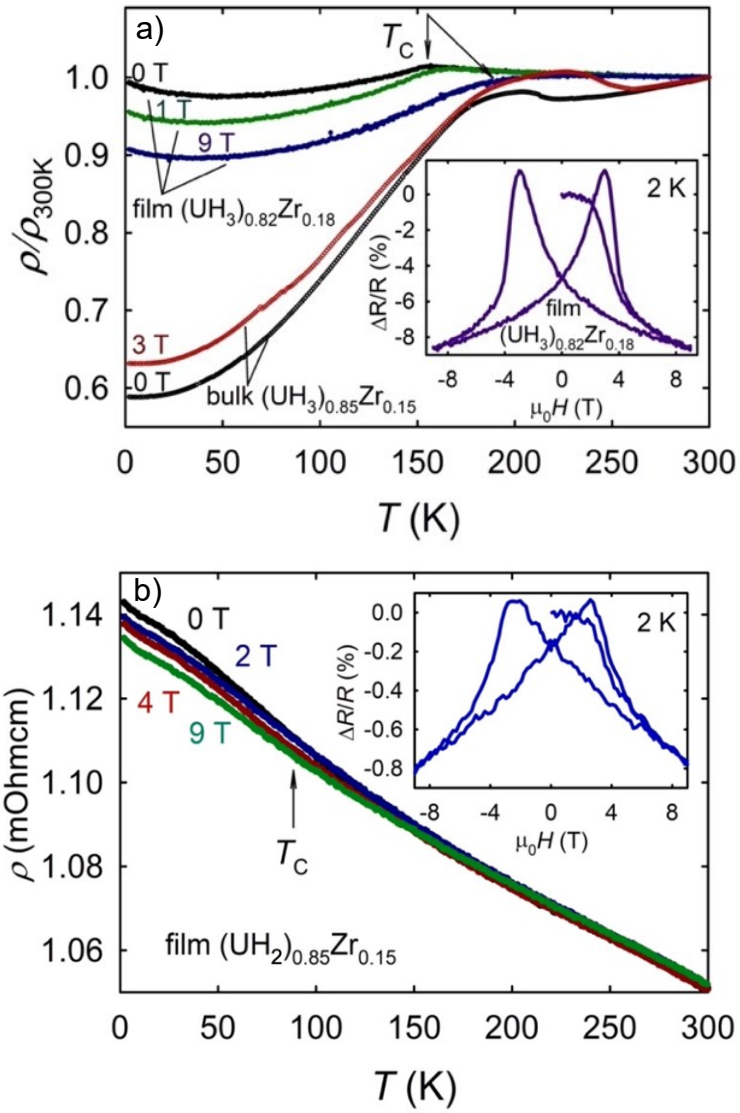


Fig. 3.34 (a) Temperature dependencies of electrical resistivity $\rho(T)$ of the $(UH_3)_{0.82}Zr_{0.18}$ film on $SiO_2$ measured in the fields 0 T, 1 T, and 9 T compared with $\rho(T)$ of bulk $(UH_3)_{0.85}Zr_{0.15}$ (adapted from Ref. [28]) and (b) $\rho$(T) of the $(UH_2)_{0.85}Zr_{0.15}$ film on Si in various fields. The field was applied along the sample surface. Insets depict the magnetoresistance of corresponding hydride films.

It can be concluded that adding transition metal atoms into the system of uranium hydrides does not make significant changes to the transport properties of thin films. In general, all the materials exhibit a negative resistivity slope, which is ascribed to magnetic disorder, leading to intense electron scattering and manifestations of weak localization phenomena [150]. The application of a magnetic field tends to align individual magnetic moments within nanograins, thereby reducing resistivity in the ferromagnetic state. The power of the effect is stronger for Mo alloyed samples.

**Conclusions and future outlook**

1. Thin film preparation is particularly useful tool in actinide research. A few advantages are stabilization of thermodynamically unstable structures (as $UH_2$ phase, not present in bulk); clean surfaces for high quality spectroscopic data (which help to detangle electronic structure when compared to calculations); shape suitable for a variety of physical properties measurements.

2. Structure analysis of U-T (T = Mo, Zr) thin films have shown the relevance of the thresholds of substitution values defined in bulk systems for stabilization of the pure γ-U phase (15 at.% Mo and 30 at.% Zr [28,116]). As all the films were below these limits, they have mixed α- and γ-U phase composition.

3. Even though U-T alloys are superconductors, only one of the films ($U_{0.92}Mo_{0.08}$) from these studies exhibited superconductivity. Transition starts at $T$ = 0.55 K, upper critical field was calculated $\mu_0 H_{c2}$ = 1.0 T. Superconductivity in the $U_{0.92}Mo_{0.08}$ film is probably unrelated to a residual α-U phase. The absence of γ-U bulk superconductivity in our thin films may be attributed to the disordered crystal structure, as a structure disorder on a scale similar to the BCS coherence length significantly impedes superconductivity.

4. In the normal state, resistivities of the films are comparable to those of bulks with the negative TCR and high absolute values exceeding 100 μΩcm. Moreover, negative TCR is present even for the compositions which showed standard metallic behavior in the bulks. This fact can indirectly prove that disorder is responsible for negative values of $d\rho/dT$, as sputter deposition brings additional structural and chemical disorders to the studied systems.

5. A few peculiarities in the physical properties of uranium hydrides (lower $T_C$ = 120 K and magnetic moment 0.8 $\mu_B$ values of $UH_2$ compared to trihydrides, even though it has a larger inter-uranium distance, and almost identical magnetic properties of α - and β-$UH_3$, which have different crystal structure) indicated that Hill physics is not dominant in the system. U-H bonding is the decisive parameter. XPS and UPS studies supplied proofs for this statement. For instance, a band between 4 and 8 eV below the Fermi energy seen on UPS spectra is formed by strong hybridization of U-6*d* and H-1*s* states.

6. The polar bonding primarily affects the outer electrons, specifically the 6*d* and 7*s* states, resulting in a repopulation of the H-1*s* states in the hydrides.

Consequently, the shifts in the shallower levels (U-5*d* and 6*p*) are more significant, 1 eV and 0.6 eV, respectively. Compare to only 0.2 eV shift towards higher binding energy of 4*f* core level lines in hydrides.

7. This slight "chemical" shift can be attributed to the relatively constant 5*f* occupancy in both uranium metal and its hydrides. The 5*f* states of uranium are near the 4*f* core states and any change would have been reflected in 4*f* lines. The asymmetry of the peaks from higher BE side indicates an increased DOS at the Fermi level. Interestingly, $UH_2$ and $UH_3$ exhibit practically identical energy and shape in all controlled spectral lines. The loss of asymmetry and higher intensities of peaks served as a sign of presence non-hydrogenated phase in a film.

8. Even though uranium hydrides show a band magnetism, the presence of the atomic final-state $5f^2$ multiplet structure in the UPS spectrum indicates strong intra-atomic electron-electron correlations. That was proved by LDA+DMFT calculations.

9. Structure analysis of U-H thin films have shown that depending on deposition parameters (namely substrate temperature and type, deposition rate), samples possess either β-$UH_3$ or $UH_2$ structure, or mixture of both phases with various crystallite sizes (from 1.5 nm to 100 nm). α-$UH_3$ was stabilized only as a minor phase in $UH_2$ films. Even Zr substitution did not help to retain α-$UH_3$ phase, however, $(UH_2)_{1-x}Zr_x$ were observed.

10. In the cases when capabilities of XRD methods for structure analysis are limited (for instance, broad peaks due to small crystallite sizes and strains, absence of some peaks due to preferred orientation, overlap of strongest peaks from phases present in the sample), non-obvious techniques can be of a use in phase identification. In particular, temperature dependence of magnetization exhibits transition temperatures characteristic for distinct magnetic phases, or specific shape of hysteresis loops can point on coexistence of magnetic and non-magnetic phases in the sample. Interestingly, the sharpness of the cusp in temperature dependence of resistivity correlates with the grain size (the sharper this feature – the bigger are the grains).

11. The magnetism of U-H system is quite robust, the transition temperature values do not change for samples with different grains size and stains, that emphasizes the importance of U-H bonds. For the hydrides with substitutions, the tendency observed for bulks (maximum of $T_C$ at 15 at.%T [148]) is not followed, and transition

temperatures values are smaller, that can be explained by incomplete incorporation of H atoms into the hydride structure (empty 4U tetrahedra).

12. Further studies of the U-based systems in a thin film form might be divided into two directions. The first one includes the preparation of higher hydrides which were predicted to form under very high pressures [157]. Some of them were calculated to be high temperature supeconductors. Strains in thin layers which work as external pressure might facilitate stabilization of these phases (probably in combination with some post-deposition treatment of thin films as exposure to atomic hydrogen [69] or heating under high $H_2$ pressure). Synthesis and study of the transport properties of these hydrides might help to understand the physics of high-temperature superconductors. The other possible route for further investigation of U-based systems is preparation of heavy-fermion compounds in thin film form [38] as was done for $UPd_2Al_3$ and $UNi_2Al_3$ [158,159]. So far, this area stays largely unexplored. Nevertheless, the advantage of thin film systems (clean surfaces) could be beneficial for the insights into the actinide electronic structure and can bring answers to questions about different ground states of isostructural 5*f* systems.

13. A general conclusion is that it is desirable to study systematically the impact of polar bonding on the uranium 5*f* magnetism, never considered before among principle tuning mechanisms.

**Bibliography**


[1] G. R. Stewart, *Unconventional Superconductivity*, Adv Phys **66**, 75 (2017).

[2] G. R. Stewart, *Non-Fermi-Liquid Behaviour in d- and f- Electron Metals*, Rev Mod Phys **73**, 797 (2001).

[3] G. R. Stewart, *Heavy-Fermion Systems*, Rev Mod Phys **56**, 755 (1984).

[4] K. T. Moore and G. van der Laan, *Nature of the 5f States in Actinide Metals*, Rev Mod Phys **81**, 235 (2009).

[5] L. Havela et al., *Crystal Structure and Magnetic Properties of Uranium Hydride $UH_2$ Stabilized as a Thin Film*, Inorg Chem **57**, 14727 (2018).

[6] S. L. Molodtsov et al., *Dispersion of 5f Electron States: Angle-Resolved Photoemission on Ordered Films of U Metal*, Phys Rev B **57**, 13241 (1998).

[7] W. Nolting and A. Ramakanth, *Quantum Theory of Magnetism* (Springer Berlin Heidelberg, Berlin, 2009).

[8] N. W. Ashcroft and N. D. Mermin, *Solid State Physics* (Saunders College, Philadelphia, 1976).

[9] S. Blundell, *Magnetism in Condensed Matter* (Oxford University Press, Oxford, 2001).

[10] K. T. Moore et al., *Failure of Russell-Saunders Coupling in the 5f States of Plutonium*, Phys Rev Lett **90**, 196404 (2003).

[11] H.H. Hill, W.N. Miner, *Plutonium and Other Actinides*, AIME 1-19 (1970).

[12] L. Havela, D. Legut, and J. Kolorenc, *Hydrogen in Actinides: Electronic and Lattice Properties*, Rep Prog Phys **86**, 056501 (2023).

[13] A. Svane, L. Petit, Z. Szotek, and W. M. Temmerman, *Self-Interaction-Corrected Local Spin Density Theory of 5 f Electron Localization in Actinides*, Phys Rev B **76**, 115116 (2007).

[14] L. Havela et al., *Magnetic Phase Transition in $UNi_2$ Compound*, Physica Status Solidi A **59**, 165 (1980).

[15] A. de Visser, *Magnetic Field–Boosted Superconductivity*, Phys Today **73**, 44 (2020).

[16] M. Tinkham, *Introduction to Superconductivity* (Courier Corporation, New York, 2004).

[17] A. Nie and M. Williams, *Determination of the Critical Field and Critical Temperature for Various Type I and Type II Metals and Alloys* (Harvard University, Cambridge 2016).

[18] N. R. Werthamer, E. Helfand, and P. C. Hohenberg, *Temperature and Purity Dependence of the Superconducting Critical Field, $H_{c2}$. III. Electron Spin and Spin-Orbit Effects*, Physical Review **147**, 295 (1966).

[19] V. V. Schmidt, *The Physics of Superconductors* (Springer Berlin Heidelberg, Berlin, 1997).

[20] H. L. Yakel, *Review of X-Ray Diffraction Studies in Uranium Alloys*, Conf Phys Metal U Alloy, (1973).

[21] J. C. Marmeggi et al., *Phonon Softening in Alpha-Uranium Associated with the CDW Transition*, Physica B Condens Matter **624**, 263 (1999).

[22] R. J. M. Konings, L. R. Morss, and J. Fuger, *The Chemistry of the Actinide and Transactinide Elements*, Vol. 4 (2006).

[23] V. P. Sinha et al., *Phase Transformation of Metastable Cubic γ-Phase in U–Mo Alloys*, J Alloys Compd **506**, 253 (2010).

[24] J. G. Huber and P. H. Ansari, *The Superconductivity of BCC U-Zr Alloys*, Physica B+C **135**, 441 (1985).

[25] D. G. Westlake, *Site Occupancies and Stoichiometries in Hydrides of Intermetallic Compounds: Geometric Considerations*, J Less Common Met **90**, 251 (1983).

[26] D. G. Westlake, *Hydrides of Intermetallic Compounds: A Review of Stabilities, Stoichiometries and Preferred Hydrogen Sites*, J Less Common Met **91**, 1 (1983)

[27] C.D. Taylor, R. Scott Lillard, *Ab-initio calculations of the hydrogen-uranium system: Surface phenomena, absorption, transport and trapping*, Acta Mater **57**, 4707 (2009).

[28] I. Tkach et al., *Electronic Properties of $\alpha-UH_3$ Stabilized by Zr*, Phys Rev B **91**, 115116 (2015).

[29] R. N. R. Mulford, F. H. Ellinger, and W. H. Zachari-Asen, *A New Form of Uranium Hydride*, J Am Chem Soc **76**, 297 (1954).

[30] R. Troc, W. Suski, *The discovery of the ferromagnetism in $U(H,D)_3$ : 40 years later*, J Alloys Compd **219**, 1 (1995).

[31] G. Kresse and J. Furthmüller, *Efficient Iterative Schemes for Ab Initio Total-Energy Calculations Using a Plane-Wave Basis Set*, Phys Rev B **54**, 11169 (1996).

[32] J. C. Lashley et al., *Low-Temperature Specific Heat and Critical Magnetic Field of α-Uranium Single Crystals*, Phys Rev B **63**, 224510 (2001).

[33] L. Havela et al., *XPS, UPS, and BIS Study of Pure and Alloyed β-$UH_3$ Films: Electronic Structure, Bonding, and Magnetism*, J Electron Spectros Relat Phenom **239**, 1 (2020).

[34] H. Kang et al., *Development of Depleted Uranium Bed for Tritium Fuel Cycle and Basic Absorption/Desorption Experiments*, Fusion Eng Des **132**, 86 (2018).

[35] A. Shugard et al., *Uranium for Hydrogen Storage Applications: A Materials Science Perspective*, Tech Rep (2010).

[36] K. Terrani et al., *Irradiation Effects on Thermal Properties of LWR Hydride Fuel*, J Nucl Mater **486**, 381 (2017).

[37] G. Zhang et al., *Improved Resource Utilization by Advanced Burner Reactors with Breed-and-Burn Blankets*, Prog Nucl En **106**, 440 (2017).

[38] R. Springell et al., *A Review of Uranium-Based Thin Films*, Adv Phys **71**, 87 (2022).

[39] W. D. Westwood, *Sputter Deposition Processes*, MRS Bull **13**, 46 (1988).

[40] S. I. Shah, *Effect of Deposition Conditions on Cation Composition During Reactive Magnetron Sputtering of High-T~ Superconductors*, Thin Solid Films **181**, 163 (1989).

[41] T. Gouder, *Thin Layers in Actinide Research*, J Alloys Compd **841**, 271 (1998).

[42] L. Havela et al., *Photoelectron Spectroscopy Study of the 5f Localization in Pu*, Phys Rev B **65**, 235118 (2002).

[43] T. Gouderet al., *$U_2O_5$ Film Preparation via $UO_2$ Deposition by Direct Current Sputtering and Successive Oxidation and Reduction with Atomic Oxygen and Atomic Hydrogen*, J Vis Exp **144**, 59017 (2019).

[44] L. Black et al., *Preparation and Photoelectron Spectroscopy Study of UNx Thin Films*, J Alloys Compd **315**, 36 (2001).

[45] I. Safi, *Recent Aspects Concerning DC Reactive Magnetron Sputtering of Thin Films: A Review*, Surf Coat Technol **127**, 203 (2000).

[46] S. Berg and T. Nyberg, *Fundamental Understanding and Modeling of Reactive Sputtering Processes*, Thin Solid Films **476**, 215 (2005).

[47] W. D. Sproul, D. J. Christie, and D. C. Carter, *Control of Reactive Sputtering Processes*, Thin Solid Films **491**, 1 (2005).

[48] E. de Hoffmann and V. Stroobant, *Mass Spectrometry: Principles and Applications,* (John Wiley&Sons, Chichester, 2007).

[49] C. Cushman et al., *Trends in Advanced XPS Instrumentation,* Vac Tech Coating (2016).

[50] S. Hüfner, *Photoelectron Spectroscopy* (Springer Berlin Heidelberg, Berlin, 2003).

[51] M. P. Seah and W. A. Dench, *Quantitative Electron Spectroscopy of Surfaces: A Standard Data Base for Electron Inelastic Mean Free Paths in Solids*, Surf Interfac Analys **1**, 2 (1979).

[52] D. R. Baer et al., *Use and Limitations of Electron Flood Gun Control of Surface Potential during XPS: Two Non-Homogeneous Sample Types*, Surf Interfac Analys **33**, 781 (2002).

[53] *X-Ray Photoelectron Spectroscopy (XPS)* Reference Pages: *Spin Orbit Splitting*, http://www.xpsfitting.com/2012/08/spin-orbit-splitting.html.

[54] B. D. Ratner and D. G. Castner, *Electron Spectroscopy for Chemical Analysis*, in *Surface Analysis–the Principal Techniques*, Vol. 51 (John Wiley & Sons: Chichester 2009).

[55] D. Briggs, *XPS: Basic Principles, Spectral Features and Qualitative Analysis*, in *Surface Analysis by Auger and X-Ray Photoelectron Spectroscopy* (IM Publications and Surface Spectra Limited, Chichester, 2003), pp. 31–56.

[56] J. F. Moulder, W. F. Stickle, P. E. ' Sobol, K. D. Bomben, and J. Chastain, Handbook of X-Ray Photoelectron Spectroscopy (Perkin-Elmer Corporation, den Prairie, Minnesota, 1992).

[57] F. Celii, *DP Woodruff and TA Delchar, Modern Techniques of Surface Science (Cambridge University Press, Cambridge, 1986)*.

[58] *X-Ray Photoelectron Spectroscopy (XPS)* Reference Pages: *Shake Up Structure*, http://www.xpsfitting.com/2012/08/shake-up-structure.html.

[59] T. Ejima et al., *Line Shapes of the XPS U-4f Spectra in Some Uranium Compounds*, Phys Rev B **53**, 1806 (1996).

[60] G. Zwicknagl and P. Fulde, *The Dual Nature of 5f Electrons and the Origin of Heavy Fermions in U Compounds*, J Phys: Condens Matter **15**, 1911 (2003).

[61] G. Zwicknagl, *The Utility of Band Theory in Strongly Correlated Electron Systems*, Rep Prog Phys **79**, 124501 (2016).

[62] P. S. Bagus et al., *Mechanisms Responsible for Chemical Shifts of Core-Level Binding Energies and Their Relationship to Chemical Bonding*, J Electron Spectros Relat Phenomena **100**, 215 (1999).

[63] P. S. Bagus et al., *Chemical Shifts of the Core-Level Binding Energies for the Alkaline-Earth Oxides*, Chem Phys Lett **196**, 641 (1992).

[64] *SPECS-RSF*, Casa Letters (2012).

[65] C. J. Powell and A. Jablonski, *Evaluation of Calculated and Measured Electron Inelastic Mean Free Paths Near Solid Surfaces*, J Phys Chem Ref Data **28**, 19 (1999).

[66] D. A. Shirley, *High-Resolution X-Ray Photoemission Spectrum of the Valence Bands of Gold*, Phys Rev B **5**, 4709 (1972).

[67] S. Fujimori et al., *Evidence of Mixed Valence States in $UM_2Al_3$ (M = Ni, Pd) Studied by X-Ray Photoemission Spectroscopy*, Solid State Commun **105**, 185 (1998).

[68] S. I. Fujimori et al., *Electronic Structures of Uranium Compounds Studied by Soft X-Ray Photoelectron Spectroscopy*, J Phys Soc Jpn **85**, (2016).

[69] T. Gouder, R. Eloirdi, and R. Caciuffo, *Direct Observation of Pure Pentavalent Uranium in $U_2O_5$ Thin Films by High Resolution Photoemission Spectroscopy*, Sci Rep **8**, 1 (2018).

[70] E. S. Ilton and P. S. Bagus, *XPS Determination of Uranium Oxidation States*, Surface and Interface Analysis **43**, 1549 (2011).

[71] P. S. Bagus et al., *The Complex Core Level Spectra of $CeO_2$: An Analysis in Terms of Atomic and Charge Transfer Effects*, Chem Phys Lett **487**, 237 (2010).

[72] T. Robert, *Correlation between Chemical Bonding and Satellite Lines in X-Ray Photoelectron Spectra of Transition Metal Compounds*, Chem Phys **8**, 123 (1975).

[73] S. I. Fujimori et al., *Electronic Structure of Heavy Fermion Uranium Compounds Studied by Core-Level Photoelectron Spectroscopy*, J Phys Soc Jpn **81**, 014703 (2012)

[74] *Photoelectron Spectroscopy, Ultraviolet Photoelectron Spectroscopy,* Reference Pages*: Thermo Fisher Scientific,* https://www.thermofisher.com/cz/en/home/materials-science/learning-center/surface-analysis/uv-photoelectron-spectroscopy.html.

[75] *UPS*, Reference Pages: https://warwick.ac.uk/fac/sci/physics/current/postgraduate/regs/ mpagswarwick/ex5/techniques/electronic/ups/.

[76] C. P. Opeil et al., *Valence-Band UPS, 6p Core-Level XPS, and LEED of a Uranium (001) Single Crystal*, Phys Rev B Condens Matter Mater Phys **73**, (2006).

[77] T. Gouder et al., *5f-Electron Localization in PuSe and PuSb*, Phys Rev Lett **84**, 3378 (2000).

[78] Y. Baer, *High-Energy Spectroscopic Study of the Occupied and Empty Electronic Levels in Uranium Metal and Compounds*, Physica B+C **102**, 104 (1980).

[79] Y. Baer and J. Schoenes, *Electronic Structure and Coulomb Correlation Energy in $UO_2$ Single Crystal*, Solid State Commun **33**, 885 (1980).

[80] J. G. Tobin et al., *Narrowing the Range of Possible Solutions to the Pu Electronic Structure Problem: Developing a New Bremstrahlung Isochromat Spectroscopy Capability*, IOP Conf Ser Mater Sci Eng **9**, 012054 (2010).

[81] J. G. Tobin et al., *Competition between Delocalization and Spin-Orbit Splitting in the Actinide 5f States*, Phys Rev B Condens Matter Mater Phys **72**, 085109 (2005).

[82] C. P. Opeil et al., *Angle-Resolved Photoemission and First-Principles Electronic Structure of Single-Crystalline α -U(001)*, Phys Rev B Condens Matter Mater Phys **75**, 045120 (2007).

[83] J. G. Tobin et al., *Towards the Quantification of 5f Delocalization*, Appl Sci, **10**, 2918 (2020).

[84] J. G. Tobin, S. W. Yu, and B. W. Chung, *Splittings, Satellites and Fine Structure in the Soft X-Ray Spectroscopy of the Actinides*, Top Catal **56**, 1104 (2013).

[85] *X-Ray Diffraction, XRD Analysis,* Reference Pages: Measurlabs, https://measurlabs.com/methods/x-ray-diffraction-xrd/.

[86] B. D. Cullity, *Elements of X-Ray Diffraction* (Addison-Wesley Publishing Company, 1978).

[87] J. A. Kaduk et al., *Powder Diffraction*, Nat Rev Methods Primers **1**, 1 (2021).

[88] I. Katsuhiko, *X-Ray Thin-Film Measurement Techniques I. Overview*, Rigaku J **24**, 10 (2008).

[89] *GIXRD, Grazing Incidence X-Ray Diffraction,* Reference Pages: Measurlabs, https://measurlabs.com/methods/grazing-incidence-x-ray-diffraction-gixrd/.

[90] *Grazing Incidence X-Ray Diffraction (GIXRD) Analysis of Thin Film Material,* Reference Pages: Rigaku Global Website, https://www.rigaku.com/applications/bytes/xrd/ultima-iv/388427460.

[91] M. Toru, *Out-of-Plane Diffraction Measurements*, Rigaku J **25**, 7 (2009).

[92] K. Inaba and S. Kobayashi, *Various Pole Figure Measurement Techniques with SmartLab, Assisting Thin Film Characterization*, Rigaku J **34**, (2018).

[93] *Texture and Pole Figures,* Reference Pages: Rigaku Global Website, https://www.rigaku.com/applications/texture-and-pole-figures.

[94] *X-Ray Reflectivity, XRR Analysis,* Reference Page: Measurlabs, https://measurlabs.com/methods/x-ray-reflectivity-xrr/.

[95] M. Yasaka, *X-Ray Reflectivity Measurement*, The Rigaku Journal **26**, 1 (2010).

[96] *PBN/PG/PBN Heaters,* Reference Pages: Thermic Edge Europe GmBH, https://thermic-edge.de/en/home/vacuum-products/vacuum-heaters/pg-pbn-heaters/.

[97] *Residual Gas Analyzer*, Reference Pages: https://www.thinksrs.com/products/rga.html.

[98] S. Berg et al., *Modeling of Reactive Sputtering of Compound Materials*, J Vac Sci Tech A: Vac, Surfaces, and Films **5**, 202 (1987).

[99] T. Gouder et al., *Electronic Structure of $UH_3$ Thin Films Prepared by Sputter Deposition*, Phys Rev B Condens Matter Mater Phys **70**, 1 (2004).

[100] N.-T. H. Kim-Ngan et al., *Characterization of U-Based Thin Films: The $UFe_{2+x}$ Case*, J Phys Conf Ser **303**, 012012 (2011).

[101] Z. Matěj et al., *Refining Bimodal Microstructure of Materials with Mstruct*, Powder Diffr **29**, S35 (2014).

[102] N. Keigo and K. Erina, *X-Ray Thin Film Measurement Techniques VII. Pole Figure Measurement*, Rigaku J **27**, 06 (2011).

[103] *How To: TEM Lamella Preparation Using FIB-SEM*, Reference Pages: https://fibfig.com/docs/tem-lamella-preparation/.

[104] L. J. van der PAUW, *A Method of Measuring Specific Resistivity and Hall Effect of Discs of Arbitrary Shape*, Semicond Dev: Pioneering Pap **174**, 1 (1991).

[105] L. J. van der PAUW, *A Method of Measuring the Resistivity and Hall Coefficient on Lamellae of Arbitrary Shape*, Philips Technical Review **20**, 220 (1958).

[106] *PPMS Vertical Puck 2*, Reference Pages: Quantum Design https://qdusa.com/siteDocs/appNotes/1085-156.pdf

[107] S. van den Berghe et al., *From High to Low Enriched Uranium Fuel in Research Reactors*, Adv Sci Tech **73**, 78 (2010).

[108] J. Ward et al., *Some Observations on the Electronic Structure of β-$UD_3$*, J Phys **40**, (1979).

[109] O. Koloskova et al., *5f-Electron Localization in Uranium Binary Hydrides: Photoelectron Spectroscopy*, Phys Rev B **109**, 75165 (2024).

[110] J. Yeh, I. Lindau, *Atomic Subshell Photoionization Cross Sections and Asymmetry Parameters: $1 \leqslant Z \leqslant 103$*, Elsevier **32**, 1 (1985).

[111] L. Havela et al., *$UH_3$-Based Ferromagnets: New Look at an Old Material*, J Magn Magn Mater **400**, 130 (2016).

[112] J. Prchal et al., *Pressure Variations of the 5f Magnetism in $UH_3$*, J Magn Magn Mater **497**, 165993 (2020).

[113] R. Li et al., *Dual 5f Character in Two Allotropes of Uranium Trihydride Studied via a First Principles Calculation*, Chem Phys **538**, 110876 (2020).

[114] M. Magnuson et al., *Electronic Properties and Bonding in $ZrH_x$ Thin Films Investigated by Valence-Band X-Ray Photoelectron Spectroscopy*, Phys Rev B **96**, 195103 (2017).

[115] V. G. Nazin et al., *UPS and EELS Study of Zirconium Oxidation*, J Surfac Inv **1**, 18 (2007).

[116] I. Tkach et al., *Electronic Properties of γ-U and Superconductivity of U-Mo Alloys*, Physica C: Supercond Appl **498**, 14 (2014).

[117] A. M. Adamska, R. Springell, and T. B. Scott, *Characterization of Poly- and Single-Crystal Uranium–Molybdenum Alloy Thin Films*, Thin Solid Films **550**, 319 (2014).

[118] N-T H Kim-Ngan et al., *Superconductivity in the Splat-Cooled UMo Alloys,* Adv Nat Sci: Nanosci Nanotechnol **6**, 015007 (2015).

[119] A. M. Adamska et al., *Growth and Characterization of Uranium–Zirconium Alloy Thin Films for Nuclear Industry Applications*, J Phys D Appl Phys **47**, 315301 (2014).

[120] J. L. O'Brien et al., *Magnetic Susceptibility of the Normal-Superconducting Transition in High-Purity Single-Crystal α-Uranium*, Phys Rev B **66**, 064523 (2002).

[121] D. Graf et al., *Fermi Surface of Uranium at Ambient Pressure*, Phys Rev B **80**, 241101 (2009).

[122] N. T. H. Kim-Ngan and L. Havela, *Superconductivity in U-T Alloys (T = Mo, Pt, Pd, Nb, Zr) Stabilized in the Cubic γ-U Structure by Splat-Cooling Technique*, J Sci: Adv Mat Dev **1**, 1 (2016).

[123] N.-T. H. Kim-Ngan et al., *γ-U Phase in U-Pt System Retained to Low Temperatures by Means of Rapid Cooling*, J Nucl Mat **479**, 287 (2016).

[124] N. T. H. Kim-Ngan et al., *Superconductivity in U–Pt System with Low Pt Concentrations (≤15 at.%)*, Phys C: Supercond Appl **546**, 1 (2018).

[125] E. A. Tereshina-Chitrova et al., *Role of Disorder in Magnetic and Conducting Properties of U–Mo and U–Mo–H Thin Films*, Mater Chem Phys **260**, (2021).

[126] I. Tkach et al., *Characterization of Cubic γ-Phase Uranium Molybdenum Alloys Synthesized by Ultrafast Cooling*, J Alloys Compd **534**, 101 (2012).

[127] S. Dutta et al., *Superconductivity in Amorphous Re Zr (X≈6) Thin Films*, J Alloys Compd **877**, 160258 (2021).

[128] G. Bergmann, *Amorphous Metals and Their Superconductivity*, Phys Rep **27**, 159 (1976).

[129] K. D. Vallejo et al., *Advances in Actinide Thin Films: Synthesis, Properties, and Future Directions*, Rep Prog Phys **85**, 123101 (2022).

[130] J. N. Eckstein et al., *Epitaxial Growth of High-Temperature Superconducting Thin Films*, J Vac Sci Tech B: Microel Proc Phenom **7**, 319 (1989).

[131] X. D. Wu et al., *Epitaxial $CeO_2$ Films as Buffer Layers for High-Temperature Superconducting Thin Films*, Appl Phys Lett **58**, 2165 (1991).

[132] J. H. Mooij, *Electrical Conduction in Concentrated Disordered Transition Metal Alloys*, Physica Status Solidi A **17**, 521 (1973).

[133] B. S. Chandrasekhar and J. K. Hulm, *The Electrical Resistivity and Super-Conductivity of Some Uranium Alloys and Compounds*, J Phys Chem Solids **7**, 259 (1958).

[134] R. D. Barnard, *Some Physical Properties of the and Phases in the U-Zr System*, Proc Phys Soc **78**, 722 (1961).

[135] *Electronegativities of the Elements* Reference Pages*: Wikipedia*, https://en.wikipedia.org/wiki/Electronegativities_of_the_elements_(data_page).

[136] L. Havela et al., *Electrical Resistivity of 5f-Electron Systems Affected by Static and Dynamic Spin Disorder*, Phys Rev B **95**, 235112 (2017).

[137] J. S. Dugdale, *Electron Transport in Metallic Glasses*, Contemp Phys **28**, 547 (1987).

[138] N. Toyota et al., *Electrical Resistance in Superconducting Amorphous Alloy $Zr_{70}Ir_{30}$*, J Physical Soc Jpn **53**, 924 (1984).

[139] A. Ślebarski et al., *Electronic Structure, Magnetic Properties and Electrical Resistivity of the $Fe_2V_{1-x}Ti_xAl$ Heusler Alloys: Experiment and Calculation*, J Phys: Condens Matter **18**, 10319 (2006).

[140] M. Isino, *Concentration and Temperature Dependences of the Electrical Resistivity of Disordered Binary Transition Metal Alloys*, J Phys Soc Jpn **54**, 3848 (1985).

[141] A. Otop et al., *High-Temperature Resistivity of $URh_2Ge_2$*, Physica B Condens Matter **371**, 378 (2006).

[142] E. A. Tereshina-Chitrova et al., *Synthesis and Physical Properties of Uranium Thin-Film Hydrides $UH_2$ and $UH_3$*, Thin Solid Films **775**, 139860 (2023).

[143] R. Troć and W. Suski, *The Discovery of the Ferromagnetism in $U(H, D)_3$: 40 Years Later*, J Alloys Compd **219**, 1 (1995).

[144] L. Kývala, L. Havela, A. P. Kadzielawa, and D. Legut, *Electrons and Phonons in Uranium Hydrides - Effects of Polar Bonding*, J Nucl Mat **567**, 153817 (2022).

[145] R. N. R. Mulford and T. A. Wiewandt, *The Neptunium-Hydrogen System*, J Phys Chem **69**, 1641 (1965).

[146] R. N. R. Mulford and G. E. Sturdy, *The Plutonium-Hydrogen System. I. Plutonium Dihydride and Dideuteride*, J Am Chem Soc **77**, 3449 (1955).

[147] B. T. M. Willis and R. I. Taylor, *Neutron Diffraction Study of Antiferromagnetism in $UO_2$*, Phys Lett **17**, 188 (1965).

[148] O. Koloskova et al., *Hydrogen in U-T Alloys: Crystal Structure and Magnetism of UH3-V*, J Alloys Compd **856**, 157406 (2021).

[149] L. Havela et al., *Structure and Magnetism of Thin UX Layers*, J Alloys Compd **408**, 1320 (2006).

[150] L. Havela et al., *Origin of Negative Resistivity Slope in U-Based Ferromagnets*, Physica B Condens Matter **536**, 527 (2018).

[151] I. Tkach et al., *Ferromagnetism with $T_C$=200 K in the Amorphous 5f Compound $UH_3Mo_{0.18}$*, Phys Rev B **88**, 060407 (2013).

[152] T. Muromura, T. Yahata, K. Ouchi, and M. Iseki, *The Variation of Lattice Parameter with Hydrogen Content of Non-Stoichiometric Plutonium Dihydride*, J Inorg Nucl Chem **34**, 171 (1972).

[153] J. W. Ward, *Electronic Structure and Bonding in Transuranics: Comparison with Lanthanides*, J Less Common Met **93**, 279 (1983).

[154] G. C. Hadjipanayis, *Nanophase Hard Magnets*, J Magn Magn Mater **200**, 373 (1999).

[155] L. Havela et al., *Strong 5f Ferromagnetism in $UH_3$-Based Materials*, *MRS Advances*, **1**, 1 (2016).

[156] B. Staliński, *Structural Features of Rare Earth Hydrides*, Z Physik Chem **145**, 1 (1985).

[157] I. A. Kruglov et al., *Uranium Polyhydrides at Moderate Pressures: Prediction, Synthesis, and Expected Superconductivity*, Sci Adv **4**, 1 (2018).

[158] M. Jourdan, M. Huth, *Superconductivity Mediated by Spin Fluctuations in the Heavy-Fermion Compound $UPd_2Al_3$*, Nat Com **398**, 47(1999).

[159] M. Jourdan et al., *Evidence for Multiband Superconductivity in the Heavy Fermion Compound*, Phys Rev Lett, **93**, 097001 (2004).

[160] J. Kondo, *Resistance Minimum in Dilute Magnetic Alloys*, Progress of Theoretical Physics **32**, 37 (1964).

[161] V. Sechovsky, L. Havela, *Intermetallic Compounds of Actinides*, **4,** 309 (North-Holland, Amsterdam 1988).

[162] E. Chason et al., *Origin of Compressive Residual Stress in Polycrystalline Thin Films*, Phys Rev Lett **88**, 4 (2002).

**List of figures**

**List of abbreviations**

| | |
|---|---|
| **AC** | Alternating Current |
| **ARPES** | Angle-Resolved Photoelectron Spectroscopy |
| **BCS** | Bardeen–Cooper–Schrieffer theory |
| **BE** | Binding Energy |
| **BIS** | Bremsstrahlung Isochromat Spectroscopy |
| **CDW** | Charge Density Wave |
| **DC** | Direct Current |
| **DFT** | Density Functional Theory |
| **DMFT** | Dynamical Mean Field Theory |
| **DOS** | Density of States |
| **EDX** | Energy-Dispersive X-Ray |
| **FC** | Field Cooling |
| **FIB** | Focused Ion Beam |
| **FWHM** | Full Width at Half Maximum |
| **GGA** | Generalized Gradient Approximation |
| **GIXRD** | Grazing Incidence X-ray Diffraction |
| **HREELS** | High-Resolution Electron Energy Loss Spectroscopy |
| **IMFD** | Inelastic Mean Free Path |
| **IPES** | Inverse Photoelectron Spectroscopy |
| **LDA** | Local Density Approximation |
| **LTC** | Linear Transfer Chamber |
| **MBE** | Molecular Beam Epitaxy |
| **MPMS** | Magnetic Property Measurement System |
| **MR** | Magnetoresistance |
| **OIS** | Open Ion Source |
| **PB** | Parallel Beam Geometry |
| **PC** | Preparation Chamber |
| **PDF** | Pair Distribution Function |
| **PES** | Photoelectron Spectroscopy |
| **PF** | Pole Figure |
| **PG-PBN** | Pyrolytic Graphite- Pyrolytic Boron Nitride Heater |
| **PLD** | Pulsed Laser Deposition |

| | |
|---|---|
| **PPMS** | Physical Property Measurement System |
| **PVD** | Physical Vapor Deposition |
| **RF** | Radio Frequency |
| **RGA** | Residual Gas Analyzer |
| **RKKY** | Ruderman-Kittel-Kasuya-Yosida |
| **RSF** | Relative Sensitivity Factors |
| **RSM** | Reciprocal Space Mapping |
| **RT** | Room Temperature |
| **SEM** | Scanning Electron Microscope |
| **SQUID** | Superconducting Quantum Interference Device |
| **T** | 3*d* (4*d*) element |
| **TCR** | Temperature coefficient of resistivity |
| **TEM** | Transmission Electron Microscopy |
| **TPD** | Temperature-Programmed Desorption |
| **UHV** | Ultra-High Vacuum |
| **UDOS** | Unoccupied Density of States |
| **UsC** | Unconventional Superconductor |
| **UPS** | Ultra-violet Photoelectron Spectroscopy |
| **UV** | Ultra-Violet |
| **VSM** | Vibrating Sample Magnetometer |
| **WHH** | Werthamer-Helfand-Hohenberg theory |
| **XPS** | X-ray Photoelectron Spectroscopy |
| **XRD** | X-ray Diffraction |
| **XRR** | X-ray Reflectivity |
| **ZFC** | Zero-Field Cooling |

**List of publications**

***Conference contributions presented by the author***

1. **O. Koloskova**, V. Buturlim, L. Havela, *Structure and magnetic properties of uranium-vanadium alloys*, Journées des Actinides (JdA2018), Praia de Porto Novo, Portugal, March 2018, **best student poster**.
2. **O. Koloskova,** L. Havela, V. Buturlim, M. Paukov, *Resistivity and magnetic properties of uranium alloys with transition metals and their hydrides*, Week of Doctoral Students (WDS2018), Prague, Czech Republic, June 2018.
3. **O. Koloskova**, V. Buturlim, M. Paukov, L. Havela, *Structure, transport and magnetic properties of uranium-vanadium alloys and hydrides*, 12th Prague Colloquium on f-Electron Systems (PCFES2018), Prague, Czech Republic, July 2018.
4. **O. Koloskova**, V. Buturlim, L. Havela, *Structure and magnetic properties of uranium-vanadium hydrides*, Uranium Science, Bristol, United Kingdom, January 2019.
5. **O. Koloskova**, V. Buturlim, P. Minárik, M. Paukov, L. Havela, *Structure and magnetic properties of uranium-vanadium hydrides*, Journées des Actinides (JdA2019), Erice, Italy, April 2019.
6. **O. Koloskova**, V. Buturlim, P. Minárik, L. Havela, *Magnetic Properties of $(UH_3)_{1-x}T_x$: Is Structure Type Important?,* XIV International Conference on Crystal Chemistry of Intermetallic Compounds, Lviv, Ukraine, 2019.
7. **O. Koloskova**, E. Tereshina-Chitrova, M.Paukov, Th. Gouder, J. Kolorenč, L. Havela, *XPS, UPS study of pure and alloyed U-H films*, the AVS 67th International Symposium & Exhibition, online, April 2020.
8. **O. Koloskova**, E. Tereshina-Chitrova, M. Paukov, Th. Gouder, J. Kolorenc, L. Havela, *XPS and UPS study of pure and alloyed U-H films*, Journées des Actinides (JdA2021), online, April 2021.
9. **O. Koloskova**, E. Tereshina-Chitrova, M.Paukov, Th. Gouder, J. Kolorenč, L. Havela, *XPS and UPS study of pure and alloyed U-H films*, Cracow Colloquium on f-electron Systems (CCFES2021), online, April 2021.

10. **O. Koloskova**, S. Mašková-Černá, A. Kolomiets, K. Miliyanchuk, A. V. Andreev, V. Buturlim, L. Havela, *$U_2Ni_2Sn$-$U_2Fe_2Sn$ system – where is QCP?*, Journées des Actinides (JdA2022), April 2022.

11. **O. Koloskova,** E.Tereshina-Chitrova, M. Paukov, T. Gouder, L. Havela, *Uranium hydride thin films: tools of phase composition determination*, Materials Research Society Spring Meeting, May 2022, Honolulu, Hawaii, **best student presentation**.

12. **O. Koloskova**, S. Mašková-Černá, A. Kolomiets, K. Miliyanchuk, A. V. Andreev, V. Buturlim, L. Havela, *$U_2Ni_2Sn$-$U_2Fe_2Sn$ system – where is QCP?,* Solid Compounds of Transition Elements (SCTE2022), Bordeaux, France, June 2022.

13. **O. Koloskova**, E. A. Tereshina-Chitrova, M. Paukov, L. Horak, M. Martinez Celis, M. Cieslar, Th. Gouder, L. Havela, *Uranium hydride thin film: why structure analysis is not sufficient?,* XV International Conference on Crystal Chemistry of Intermetallic Compounds (IMC-XV), online September 2023.

14. **O. Koloskova**, E.Tereshina-Chitrova, M. Paukov, T. Gouder, L. Havela, *Uranium hydride thin films: stabilization of thermodynamically unstable phases*, Prague Colloquium on f-electron systems (PCFES 2023), Prague, Czech Republic, June 2023.

15. **O. Koloskova**, E. Tereshina-Chitrova, M. Paukov, T. Gouder, J. Kolorenc, L. Havela, *Electronic structure of U hydrides probed by XPS and UPS*, Solid Compounds of Transition Elements (SCTE2024), Prague, Czech Republic, June 2024.

***Publications in peer-reviewed international journals***

1. V. Buturlim, J. Valenta, J. Prchal, **O. Koloskova**, P. Dolezal, D. Kaczorowski, M. Martinez Celis, I. Halevy, A. Kolomiets, S. Cerna-Maskova, M. Cieslar, M. Dopita, J. Kastil, P. Kral, I. Turek, F. Honda, D. Aoki, K. Miliyanchuk, E. Svanidze, M. Koenig, M. Divis, Y. Uwatoko, K. Gofryk, J. Kolorenc, D. Legut, U. Wdowik, K. Carva, L. Havela, *Uranium ferromagnetism approaching ambient temperatures: $UCu_2P_2$*, Phys Rev X (2024), submitted.

2. **O. Koloskova**, B. Chatterjee, L. Havela, T. Gouder, J. Kolorenč, *5f-electron localization in uranium binary hydrides: Photoelectron spectroscopy*, Phys Rev B **109**, 75165 (2024).

3. E. A. Tereshina-Chitrova, L. Havela, M. Paukov, **O. Koloskova**, L. Horák, M. Dopita, M. Martinez Celis, M. Cieslar, Z. Šobáň, T. Gouder, F. Huber, *Synthesis and physical properties of uranium thin-film hydrides $UH_2$ and $UH_3$*, Thin Solid Films **775**, 139860 (2023).

4. S. Maskova-Cerna, A. Kolomiets, J. Prchal, I. Halevy, V. Buturlim, M. Nikolaevsky, **O. Koloskova**, P. Kozelj, M. Konig, M. Divis, L. M. Sandratskii, J. Kastil, A. V. Andreev, E. Svanidze, L. Havela, *Insight into the physics of the 5f-band antiferromagnet $U_2Ni_2Sn$ from the pressure dependence of crystal structure and electrical resistivity*, Phys Rev B **103**, 035104 (2021).

5. E. A. Tereshina-Chitrova, L. Havela, M. Paukov, M. Dopita, L. Horák, **O. Koloskova**, Z. Šobáň, T. Gouder, F. Huber, A. Seibert, *Role of disorder in magnetic and conducting properties of U–Mo and U–Mo–H thin films*, Mater Chem Phys **260**, 124069 (2021).

6. **O. Koloskova**, V. Buturlim, M. Paukov, P.Minarik, M.Dopita, K. Miliyanchuk, L.Havela, *Hydrogen in U-T alloys: Crystal structure and magnetism of $UH_3$-V*, J Alloys Compd **856**, 157406 (2020).

6. I. Pazukha, **O. Koloskova**, S. Protsenko, *Peculiarities of magnetoresistive properties of Co/Ag/Py pseudo spin-valves under heat treatment*, J Supercond Nov Magn **33**, 1119 (2020).

7. V. Buturlim, **O. Koloskova**, P. Minárik, L. Havela, *Anomalous superconductivity of the U-Ti alloys*, JPS Conf Proc **30**, 011063 (2020).

8. V. Buturlim, M. Falkowski, M. Paukov, **O. Koloskova**, D. Drozdenko, M. Dopita, P. Minárik, S. Maškova, P. Doležal, L. Havela, *Spin fluctuations in hydrogen-stabilized Laves phase $UTi_2H_5$*, Phil Mag **99**, 1881 (2019).

9. I.M. Pazukha, Y.M. Shabelnyk, I.M. Kozak, T.I. Polek, T.M. Shabelnyk, **O.A. Koloskova**, S.I. Protsenko, *FMR study of the film systems based on magnetic and noble metals*, 2016 Int. Conf. Nanomater. Appl. Prop. IEEE, 01NTF17-1 (2016).

10. V.V. Kulish, A.V. Lysenko, G.A. Oleksiienko, G.V. Bychenko and **O.A. Koloskova**, *Modernized method of averaged characteristics for problem solving of multiharmonic resonant interactions in devices of high-current electronics*, J Nano-Electron Phys **7** 02015 (2015).

## A Attachments

### *A.1 Sputtering parameters used for the thin films production.*

| Sample' s name | Substrate | Substrate temperature (K) | Buffer/Capping | Current (mA) | Deposition time (sec) | $p_{Ar+H2}$ ($\cdot 10^{-3}$ mbar) | $p_{H2}$ ($\cdot 10^{-4}$ mbar) |
|---|---|---|---|---|---|---|---|
| SO1 | $SiO_2$ | RT | -/- | 1 mA | 3600 | 6 | 6 |
| SO2 | $SiO_2$ | RT | -/- | 0.7 mA | 4000 | 6 | 6 |
| SO3 | $SiO_2$ | RT | -/- | 2.2 mA | 3000 | 6 | 6 |
| SO4 | $SiO_2$ | RT | -/- | 1.5 mA | 3000 | 6 | 6 |
| SO5 | $SiO_2$ | RT | Mo/Mo | 1.7mA | 5000 | 8 | 4 |
| SO6 | $SiO_2$ | 170 | Mo/Mo | 2.3 mA | 4000 | 5 | 3.5 |
| SO7 | $SiO_2$ | ≈ 340 | Mo/Mo | 2.2 mA | 1000 | 6 | 6 |
| S8 | Si | RT | -/Mo | 2.3 mA | 4000 | 5 | 3.2 |
| S9 | Si | 170 | Mo/Mo | 2.8 mA | 4000 | 8 | 6 |
| S10 | Si | 150 | -/Mo | 2.3 mA | 4000 | 5 | 3.5 |
| SM11 | MgO | 170 | -/Zr | 2 mA | 3600 | 6 | 4 |
| SM12 | MgO | 170 | -/Zr | 3.1 mA | 3100 | 6 | 4 |
| SM13 | MgO | 170 | -/Zr | 1 mA | 3600 | 6 | 4 |
| SC14 | $CaF_2$ | RT | -/Mo | 2 mA | 1000 | 8 | 6 |
| SC15 | $CaF_2$ | 170 | -/Zr | 2.6 mA | 3600 | 6 | 4 |
| SC16 | $CaF_2$ | 170 | -/Zr | 2.6 mA | 1000 | 6 | 4 |